UNIVERSIDADE ESTADUAL DE CAMPINAS
Instituto de Física Gleb Wataghin

ALISSON CECCATTO DOS SANTOS

Engineering One- and Two-Dimensional Supramolecular Porous Planar Carbon Lattices

Engenharia de Redes Supramoleculares de Carbono Planares e Porosas Uni- e Bi-Dimensionais

CAMPINAS
2024

ALISSON CECCATTO DOS SANTOS

Engineering One- and Two-Dimensional Supramolecular Porous Planar Carbon Lattices

Engenharia de Redes Supramoleculares de Carbono Planares e Porosas Uni- e Bi-Dimensionais

Tese de Doutorado apresentada ao Instituto de Física Gleb Wataghin da Universidade Estadual de Campinas como parte dos requisitos exigidos para a obtenção do título de Doutor em Ciências, na Área de Física Aplicada.

Thesis presented to the Gleb Wataghin Institute of Physics of the University of Campinas in partial fulfillment of the requirements for the degree of Doctor in Science, in the field of Applied Physics.

Supervisor/Orientador: PROF. DR. ABNER DE SIERVO

ESTE EXEMPLAR CORRESPONDE À VERSÃO FINAL DA TESE DE DOUTORADO DEFENDIDA POR ALISSON CECCATTO DOS SANTOS E ORIENTADA PELO PROF. DR. ABNER DE SIERVO.

CAMPINAS
2024

Ficha catalográfica
Universidade Estadual de Campinas (UNICAMP)
Biblioteca do Instituto de Física Gleb Wataghin
Lucimeire de Oliveira Silva da Rocha - CRB 8-9174

Santos, Alisson Ceccatto dos, 1995-
Sa59e Engineering one- and two-dimensional supramolecular porous planar carbon lattices / Alisson Ceccatto dos Santos. – Campinas, SP : [s.n.], 2024.

Orientador(es): Abner de Siervo.
Tese (doutorado) – Universidade Estadual de Campinas (UNICAMP), Instituto de Física Gleb Wataghin.

1. Síntese sobre superfícies. 2. Nanoestrutura. 3. Nanofitas de grafeno. 4. Espectroscopia fotoeletrônica de raio X. 5. Microscopia de tunelamento de elétrons. I. Siervo, Abner de, 1972-. II. Universidade Estadual de Campinas (UNICAMP). Instituto de Física Gleb Wataghin. III. Título.

Informações complementares

Título em outro idioma: Engenharia de redes supramoleculares de carbono planares e porosas uni- e bi-dimensionais
Palavras-chave em inglês:
On-surface synthesis
Nanostructures
Graphene nanoribbons
X-ray photoelectron spectroscopy
Scanning tunneling microscopy
Área de concentração: Física Aplicada
Titulação: Doutor em Ciências
Banca examinadora:
Abner de Siervo [Orientador]
Fernando Loureiro Stavale Junior
Luis Henrique de Lima
Júlio Criginski Cézar
Roberto Magalhães Paniago
Data de defesa: 29-11-2024
Programa de Pós-Graduação: Física

Identificação e informações acadêmicas do(a) aluno(a)
- ORCID do autor: https://orcid.org/0000-0001-7619-3062
- Currículo Lattes do autor: http://lattes.cnpq.br/0743600172828785

INSTITUTO DE FÍSICA
GLEB WATAGHIN

MEMBROS DA COMISSÃO EXAMINADORA DA TESE DE DOUTORADO DO ALUNO ALISSON CECCATTO DOS SANTOS – RA 163518 APRESENTADA E APROVADA AO INSTITUTO DE FÍSICA GLEB WATAGHIN, DA UNIVERSIDADE ESTADUAL DE CAMPINAS, EM 29/11/2024.

COMISSÃO JULGADORA:

- Prof. Dr. Abner de Siervo (IFGW/ UNICAMP) - Presidente e Orientador

- Prof. Dr. Fernando Loureiro Stavale Junior (Centro Brasileiro de Pesquisas Físicas)

- Prof. Dr. Luis Henrique de Lima (Universidade Federal do ABC, Centro de Ciências Naturais e Humanas)

- Prof. Dr. Júlio Criginski Cézar (Centro Nacional de Pesquisa em Energia e Materiais/ Laboratório Nacional de Luz Síncroton)

- Prof. Dr. Roberto Magalhães Paniago (Departamento de Física da Universidade Federal de Minas Gerais)

OBS.: Ata da defesa com as respectivas assinaturas dos membros encontra-se no SIGA/Sistema de Fluxo de Dissertação/Tese e na Secretaria do Programa da Unidade.

CAMPINAS
2024

www.inova.unicamp.br
Rua Dr. Ricardo Benetton Martins, nº 1551
Bosque das Palmeiras, Campinas - SP
CEP: 13086-510

TERMO DE SIGILO E CONFIDENCIALIDADE

Título da Pesquisa: Engineering One- and Two-Dimensional Supramolecular Porous Planar Carbon Lattices
Finalidade: Defesa de Tese de Doutorado
Aluno (a): Alisson Ceccatto dos Santos
Orientador (a): Abner de Siervo
Unidade: IFGW
Data: 29/11/2024

1. São tidas como **"Informações Confidenciais"** todas as informações relacionadas à tese/dissertação mencionada acima, seja presencialmente ou por meio de serviço de videoconferência, expressas por qualquer meio seja oral, escrito ou eletrônico, constantes em documentos, planilhas, sistemas, fotografias, relatórios, disquetes, disco laser, desenhos, modelos, dados, especificações, relatórios, compilações, programas de computador, pedidos de patentes e patentes, produtos e processos e outros, a que venham a ser apresentadas ou de alguma forma disponibilizadas aos examinadores e demais presentes.

2. Os signatários manterão sigilo, em relação às todas e quaisquer **"Informações Confidenciais"** inclusive orais**,** mesmo que estas não contenham nem sejam acompanhadas de qualquer tipo de advertência de sigilo, devendo tal condição ser sempre presumida.

3. Os signatários manifestam absoluta ciência e anuência de que as informações serão protegidas pelos meios legais e desde já asseguram que as **"Informações Confidenciais"** a que tiverem acesso, não serão mecanicamente copiadas ou de qualquer outra forma reproduzidas, bem como não serão divulgadas, publicadas nem serão circuladas, sem a autorização do aluno, do orientador e da Agência de Inovação Inova Unicamp.

4. O descumprimento dos itens ou condições previstas neste Termo sujeitará o signatário que incorrer na infração ao presente à responsabilidade criminal e ou civil e consequente indenização.

5. Os signatários a seguir qualificados e assinados manifestam sua total ciência anuência com as condições estabelecidas neste termo.

Nome Completo	CPF	Assinatura
Rafaela F. Zapparoli dos Santos	423.838.498-98	Rafaela Zapparoli
Marlene C. Ceccatto dos Santos	279.202.218-38	Marlene C. Ceccatto dos Santos
Marceli Ceccatto dos Santos	369.656.638-12	Marceli Ceccatto dos Santos
Micheli Ceccatto dos Santos	323.694.318-14	Micheli Ceccatto dos Santos

Acknowledgements

First, I would like to express my deepest gratitude to my advisor, Professor Abner de Siervo. I am grateful for all his teachings over the years, allowing me to grow academically. Thank you for all the discussions at the café and the drive to strive for excellence at all times. Finally, I am grateful for the encouragement and opportunity to complete my PhD sandwich in Germany.

I would like to thank the members of the Surface Science Group for having welcomed me in the best possible way. In particular, Prof. Richard Landers, for all his teachings, always helped me in the lab. For always being interested in the progress of my PhD and answering my questions. To the labmates I had throughout my PhD: Nataly, Isabela, Vanessa, Eidsa, and Iago.

I am grateful to everyone who helped me during my time in Erlangen. Special thanks to Prof. Steinrück, for hosting me and providing exciting discussions about surface science. To Marie, Natalie, Felix, and Valentin for the amazing environment.

I also thank Prof. Duncan John Mowbray for the fruitful discussions and for providing the DFT calculations that supported most of our experimental findings.

I would also like to thank the entire technical and administrative staff of the Postgraduate Program and the DFA, especially Flávia and Alessandra.

To FAPESP (Fundação de Amparo à Pesquisa do Estado de São Paulo) for my PhD fellowship (2021/04411-1) and to CAPES (Coordenação de Aperfeiçoamento de Pessoal de Nível Superior) for funding my sandwich PhD (PROBRAL: 627947/2021-01) in Erlangen.

I would like to thank my family, my mother Marlene, my father José, and my sisters Micheli and Marceli, for their unconditional love and affection. Without you, I would never have been able to achieve my goals. Thank you for everything. To Heleninha, for her joy and affection. To my home-office partner Frida. Finally, to my dear Rafaela, for always being by my side throughout all these years, unconditionally supporting my decisions, and helping me face all the difficulties to move forward on this journey. Thank you very much.

Abstract

The on-surface synthesis is a promising approach to building low-dimensional nanostructures allowing the investigation of the fundamental physical and chemical phenomena. The process is based on the assembly of atoms and molecules, typically on well-defined metallic surfaces, to construct nanomaterials with unique geometries and consequently properties. This allows the development of new quantum materials with potential applications in nanotechnology. To obtain these nanoarchitectures, several on-surface methods can be employed, such as the Ullmann coupling reaction, Sonogashira reaction, and metal coordination, among others. Typically, such processes are highly dependent on the choice of both the substrate templating and the building block and usually form short-range domains. This motivates the search for potential support substrates and molecular precursors that produce highly-ordered nanostructures in long-range domains independently of the substrate used. Moreover, prominent new nanostructures with emerging electronic properties can be obtained using the atomic and molecular control of the on-surface methods.

In this thesis, we systematically explored the behavior of different organic precursors under ultra-high vacuum (UHV) conditions by combining scanning tunneling microscopy (STM) and X-ray photoelectron spectroscopy (XPS) results with density functional theory (DFT) calculations.

Firstly, we synthesized highly-ordered Cu-coordinated nanostructures with unique geometries using 1,3,5-tris[4-(pyridin)phenyl]benzene (TPyPB) and 1,3,5-tris[4-(pyridin)-[1,1'-biphenyl]benzene (TPyPPB) molecules on Cu(111). The nanoarchitectures obtained extend over hundreds of nanometers with uniform geometry. Depending on the annealing temperature, unique nanostructures can be obtained, named flower-like and diamond-shaped. Moreover, our DFT calculations revealed that all structures are stabilized by N–Cu–N coordination with Cu adatoms on the surface. The adsorption of TPyPPB molecules on Ag(111) reveals a striking difference from Cu(111), where no coordination occurred. This allowed us to explore the behavior of the precursors in the presence of extrinsically adsorbed atoms. We performed the deposition of metal (Co) and nonmetal (Cl) atoms to synthesize unique nanostructures stabilized by Co-coordination and unconventional H$\cdots$Cl hydrogen bonds.

Finally, by using 2,7,11,16-tetrabromotetrabenzo[a,c,h,j] phenazine (TBTBP) molecules we synthesized doped and porous graphene nanoribbons (GNRs) on Ag(110). By combining our results with previous ones from our group, we successfully demonstrated that such ribbons grow regular one-dimensional architecture independently of the substrate orientation.

Resumo

As reações de síntese confinadas à superfície se mostraram promissoras para a construção de estruturas de baixa dimensionalidade. Tais nanoestruturas nos permite investigar fenômenos físicos e químicos fundamentais. Este processo é baseado no agrupamento de átomos e moléculas, normalmente em superfícies metálicas altamente orientadas, para construir nanomateriais com geometrias únicas, permitindo o desenvolvimento de novos materiais quânticos com potenciais aplicações em nanotecnologia. Para obter essas nanoarquiteturas, vários métodos podem ser empregados, como a reação de acoplamento de Ullmann, reação de Sonogashira, coordenação metálica, entre outros. Normalmente, esses processos são dependentes da escolha do substrato e do precursor molecular, e geralmente formam estruturas com domínios curtos. Isto motiva a comunidade científica pela busca de potenciais substratos suporte, assim como precursores moleculares, que produzam nanoestruturas altamente ordenadas formando domínios de longo alcance, que independam do substrato utilizado.

Nesta tese, exploramos sistematicamente o comportamento de diferentes precursores orgânicos sob condições de ultra-alto vácuo (UHV), combinando resultados de microscopia de tunelamento de elétrons (STM) e espectroscopia de fotoelétrons excitados por raios X (XPS) complementadops com cálculos de teoria do funcional da densidade (DFT).

Primeiramente, sintetizamos nanoestruturas altamente ordenadas e coordenadas por Cu com geometrias únicas usando as moléculas de 1,3,5-tris[4-(piridin)fenil]benzeno (TPyPB) e 1,3,5-tris[4-(piridin)-[1,1'-bifenil]benzeno (TPyPPB) sobre Cu(111). As nanoarquiteturas obtidas estendem-se sobre centenas de nanômetros com uma geometria uniforme. Dependendo da temperatura do tratamento térmico, nanoestruturas com morfologias únicas podem ser obtidas, denominadas aqui como "*flower-like*" e "*diamond-shaped*". Além disso, nossos cálculos DFT revelaram que todas as estruturas são estabilizadas pela coordenação, N–Cu–N, com adátomos de Cu na superfície. A adsorção das moléculas TPyPPB sobre Ag (111) mostra uma diferença marcante comparado com Cu (111), onde não observamos coordenação metálica com Ag. Isso nos permitiu explorar o comportamento destes precursores na presença de átomos extrinsecamente adsorvidos. Realizamos a deposição de átomos metálicos (Co) e não metálicos (Cl) para sintetizar nanoestruturas estabilizadas por coordenação metálica e ligações de hidrogênio H$\cdots$Cl não-convencionais. Finalmente, usando moléculas de 2,7,11,16-tetrabromotetrabenzo[a,c,h,j]fenazina (TBTBP) sobre Ag (110) sintetizamos nanofitas de grafeno dopadas e porosas (GNRs). Ao combinar nossos resultados com trabalhos anteriores de nosso grupos, demonstramos com sucesso que tais nanofitas crescem uma estrutura uniforme independentemente do substrato usado.

List of Publications

1. **Alisson Ceccatto**, Eva Marie Freiberger, Natalie J. Waleska Wellnhofer, Simon Jaekel, Duncan John Mowbray, Christian Papp, Hans-Peter Steinrück, and Abner de Siervo. “Engineering Large Nanoporous Networks with Size and Shape Selected by Appropriate Precursors”. **Carbon 2024, 221, 118945.**

2. **Alisson Ceccatto**, Gustavo Ramon Campi, Vanessa Carreño Diaz, Eidsa Brenda da Costa Ferreira, Natalie J. Waleska-Wellnhofer, Eva Marie Freiberger, Simon Jaekel, Christian Papp, Hans-Peter Steinrück, Duncan John Mowbray, and Abner de Siervo. “Engineering Two-Dimensional Supramolecular Self-Assembly: The Role of Cl Atoms”. **Under Review. FlatChem (FLATC-D-24-00446)**

3. **Alisson Ceccatto dos Santos**, Nataly Herrera-Reinoza, Alejandro Pérez Paz, Duncan John Mowbray, and Abner de Siervo. “Reassessing the Adsorption Behavior and On-Surface Reactivity of a Brominated Porphyrin on Cu(111)”. **The Journal of Physical Chemistry C 2021, 125, 31, 17164-17173 (Front cover).**

4. Majid Shaker, Maximilian Muth, Julien Steffen, **Alisson Ceccatto**, Simon Jaekel, Rajan Adhikari, Pascal Gazetas, Christoph Oleszak, Abner de Siervo, Norbert Jux, Andreas Goerling, Ole Lytken, Hans-Peter Steinrück. "Coverage-and temperature-induced self-metalation of tetraphenyltransdibenzoporhyrin on Cu(111)". **J. Phys.: Condens. Matter in press.**

5. Thiago Gonzalez-Llana Brito, Fábio J. R. Costa, **Alisson Ceccatto**, Charles A. N. de Almeida, Abner de Siervo, Odilon D. D. Couto Jr., Ingrid David Barcelos and Luiz Fernando Zagonel. "Investigating the Impact of ITO Substrates on the Optical and Electronic Properties of WSe2 Monolayers". **Nanotechnology 2025, 36, 055704.**

6. Nataly Herrera-Reinoza, Duncan John Mowbray, Alejandro Pérez Paz, **Alisson Ceccatto**, Rodrigo Cezar de Campos Ferreira, and Abner de Siervo. "On-surface synthesis of 1D and 2D porphyrin MOFs on Ag(100) controlled by the substrate temperature". **Submitted. Nanoscale.**

7. Gustavo Campi, **Alisson Ceccatto**, Abner de Siervo, Duncan John Mowbray. "Using FTIR Simulation to Characterize Metal-Organic Frameworks: TPyPB on Cu(111)". **Submitted. Carbon Trends.**

Contents

Chapter 1

Introduction

Since the foundations of atomic and molecular sciences, enormous efforts have been made to fabricate, characterize, and manipulate materials at atomic and molecular levels. The control of atoms and molecules enables us to access matter's novel electronic, magnetic, and chemical properties. To shed light on nature's behavior of atomic and molecular species, several instrumental developments were essential, starting in the 50s with field-ion microscopy (FIM) [1]. In the last decades, imaging capabilities increased their resolution with the advent of scanning probe microscopy (SPM) techniques, e.g., atomic force microscopy (AFM) [2] and scanning tunneling microscopy (STM) [3]. The latter allowed the control of individual atoms on conductive samples, opening the possibility to explore the quantum properties of nanomaterials. Nowadays, one of the main challenges for science is to dominate the synthesis techniques at the angstrom scale. So far, the most successful synthesis routines employed are based on the bottom-up fabrication approach. This strategy consists of using building blocks, such as atoms and molecules, to build supramolecular structures. In this context, surface science is one of the most powerful playgrounds for the synthesis of one- and two-dimensional models to explore the fundamental aspects of materials.

In particular, porous nanoarchitectures are an interesting material due to their confinement properties [4]. The most fundamental porous structure is the so-called quantum corrals, which consist of a well-defined confined region in the Angstrom scale obtained by atomic manipulation on metal surfaces [5]. This structure showed experimentally that the electronic density of states (DOS) of a surface is strikingly affected by spatial confinement. Such confined systems opened the possibility of customizing the electronic properties of the surface by changing their morphology. More complex porous nanoarchitectures are obtained based on supramolecular self-assembly [6].

Among the building blocks used for nanomaterials growth, organic precursors have been successfully employed due to their versatility to be functionalized and their chemical stability. A potential class of supramolecular structure is the two-dimensional metal-organic framework (2D-MOF), which can be designed with a variety of molecules and metal atoms [7]. These materials typically present porous morphology, similar to 3D-MOF, which can be explored as a templating material for quantum confinement [6]. Moreover, the molecular precursors forming the 2D-MOF are bonded via a metal atom/adatom, defined here as metal-coordination. If the metal is magnetic (Fe, Co, Ni), this material can present unique

properties, such as spin filtering. Such material has been successfully synthesized using on-surface methods on metal substrates with a wide range of geometries.

In the last decades, those surface-assisted methods allowed the fabrication of a so far inaccessible material with atomic and molecular level precision: graphene nanoribbons (GNRs) [8]. While graphene consists of a two-dimensional gapless semimetal, the nanoribbons present a bandgap opening, due to the confinement of the charge carriers in this quasi-one-dimensional structure. The electronic properties of GNRs are very sensitive to their width and edge termination. Nowadays, bottom-up fabrication is the most suitable approach to obtain such promising material with atomic and molecular precision. The most successful method for GNR synthesis is the on-surface Ullmann reaction [9]. This process consists of using organic building blocks functionalized with halogenated chemical groups. The reaction is catalyzed on a well-oriented metallic surface, and its first step consists of the C-X (X = F, Cl, Br, I) bond cleavage. As the reaction continues, organometallic and/or polymer species are formed. Despite the well-known mechanism, this method still has some important challenges, such as the synthesis of long-range nanostructures. Typically, the well-oriented substrates used work not only as a catalytic environment but also as a template, defining the nanostructure geometry formed. In the case of GNRs, this dependence on the substrate dramatically affects the properties of the material. The same molecular precursor usually presents distinct behaviors and energy barriers depending on the surface orientation.

In general, molecules with chemical and mechanical stability, as well as stable at high temperatures are promising building blocks for on-surface synthesis. Polycyclic aromatic molecules are a versatile class of precursors due to their planar and non-planar structures, high degree of functionalization, and stability. The morphology of the supramolecular network formed is strongly related to the building block elementary geometry. Even the size of the precursor can completely change the supramolecular ordering. In particular, we explored the molecules 1,3,5- tris[4-(pyridin)phenyl]benzene (TPyPB) and 1,3,5-tris[4-(pyridin)-[1,1'-biphenyl] benzene (TPyPPB) posses the same pyridyl end groups but differing in their size by only one benzene ring. By adsorbing these molecules on coinage metals, especially Cu(111) and Ag(111), we were able to engineer a plethora of two-dimensional porous nanostructures depending on the molecular size. In parallel, we also made use of 2,7,11,16,tetrabromotetrabenzo[a,c,h,j]phenazine (TBTBP) molecular precursors to obtain graphene nanoribbons with a unique morphology, on an anisotropic substrate, Ag(110).

In this context, the main goal of this thesis is to tune and explore the synthesis of porous low-dimensional materials. The use of such 1D and 2D materials helps us to understand their most fundamental aspects, which can be further used to explore new synthesis routes and properties. We systematically investigated the on-surface synthesis of supramolecular porous nanostructures obtained in different pathways. We explored the synthesis of metal-coordinated nanostructures with unique geometries. Moreover, by adding extrins-

ically nonmetals, we investigate the synthesis of nanostructures stabilized by unconventional intermolecular bonds mediated by single adatoms. One of the main challenges in bottom-up synthesis is to obtain a nanomaterial with the same morphology on different templating substrates. This is one of the first steps to make this material scalable. In this context, we successfully synthesized a unique doped and porous graphene nanoribbon which grows a regular and uniform nanomaterial independent of the surface used. In summary, we explored how single adatoms change the material's morphology by employing atomically precise bottom-up synthesis.

To probe and design such structures, it is mandatory to use surface-sensitive techniques. The chemical states of our samples were probed by X-ray photoelectron spectroscopy (XPS) while the morphology was investigated by scanning tunneling microscopy (STM) supported by density functional theory (DFT) calculations. The combination of these three methods allows us to determine the structure formed as well as the reaction products. The theoretical results were obtained by using the Imbabura cluster at Yachay Tech University by our collaborators. The experimental investigation was carried out in the University of Campinas (UNICAMP) at the Surface Science Group (GFS) in the Department of Applied Physics (DFA) of Gleb Wataghin Physics Institute (IFGW).

This thesis is organized as follows: in Chapter 2, a general description of the synthesis routes and properties of nanoporous metal-organic frameworks and graphene nanoribbons. In Chapter 3, the experimental techniques employed and the sample preparation procedures used. In the sequence, we present the results and discussion of the TPyPB and TPyPPB molecules adsorbed on Cu(111) in Chapter 4. In the following, we show the results of TPyPPB molecules on Ag(111) in the presence of Cl and Co adatoms in Chapters 5 and 6, respectively. In Chapter 7 we discussed the synthesis of doped graphene nanoribbons using TBTBP molecules on Ag(110). Finally, the main concluding remarks of this thesis as well as perspectives for future investigations.

Chapter 2

Synthesis of planar carbon lattices

2.1 Two-dimensional metal-organic frameworks

Metal-organic frameworks are porous materials consisting of a neutral or anionic species connected to cations [10]. In the case of MOFs, the latter are essentially metal clusters while their counterparts are molecules, also called ligands. The structure formed can be one-, two-, or three-dimensional, despite the dimensionality of the material, the main common characteristic of this material is its high porosity. Such porous materials present a great potential for application in CO_2 capture [11], H_2 storage [12], and other gases [13]. Moreover, their unique characteristics combining organic and metals can also be explored in optoelectronics [14, 15], sensors [16, 17], magnetism [18, 19], catalysis [20, 21], drug delivery [22, 23], bioimaging [24], etc. The synthesis of 3D-MOFs has its roots in the coordination chemistry [6]. Nowadays, there are hundreds of thousands of different 3D-MOFs that can be possibly obtained by combining different functional organic precursors and metals [4]. In this context, the miniaturization down to two-dimensional MOFs allows us to model their more fundamental phenomena. By reducing the dimensionality, we simplify many processes and permit investigations at atomic and molecular levels. Moreover, the miniaturization of devices pursues low-dimensional materials, and MOFs are an interesting class with potential applications in multiple fields.

In the last decades, the fabrication of supramolecular nanostructures has been extensively studied developing new opportunities in the synthesis of low-dimensional materials. The molecules can assemble in several forms, from weak interactions such as hydrogen bonds [25], van der Waals interaction [26], or dipole-dipole interaction [27] to stronger interactions, as covalent nanostructures [28]. Metal-ligand coordination is a non-covalent interaction with intermediate strength. This gives a higher bond directionality compared to hydrogen bonds and π–π stacking. Moreover, the great availability of organic ligands with several functional groups combined with diverse transition metals is an enormous playground for the scientific community in investigating new materials. On the other hand, the synthesis routines of atomic thin materials typically require an atomically flat platform, as illustrated in Figure 2.1. The surface confinement adds a new player in the synthesis route: the substrate. The platform used affects both the molecule-metal interaction and the geo-

metry of the nanostructure formed. Therefore, the interplay between the nature of the metal, the ligand elementary morphology, and the substrate will define the MOF formed.

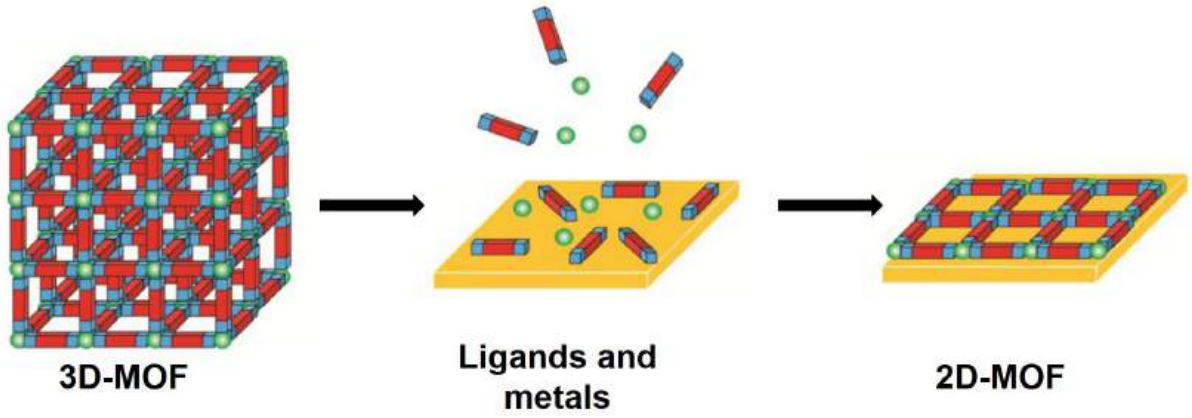

Figure 2.1: Illusration of the three- and two-dimensional MOFs assemble process. Adapted from [10].

Figure 2.2 displays the behavior of 1,3,5-tris(pyridyl)benzene (TPyB) molecules on Au(111) in the presence of Cu and Fe adatoms [29]. The TPyB molecule consists of three pyridyl groups connected to a central benzene ring. Two of the nitrogenated groups are connected in para (ortho) positions, while the third is connected in a para-position, giving this precursor a specific symmetry, with the end groups disposed 120° from each other. Regarding coordination nanostructures, a plethora of functional polyaromatic precursors has been explored with both nitrogenated (-N [30], -CN [31], -NH_2 [32]) and non-nitrogenated (-OH [33], -SH [34]) end groups. In the case of TPyB molecules, the coordination between the ligands and metals is via the pyridyl functional groups. STM images reveal that the codeposition of Cu and TPyB molecules on Au(111) leads to a honeycomb network with a lattice constant of ≈ 2.7 nm, as shown in Figure 2.2a. The molecules are stabilized by two-fold Cu-Py (Py = pyridyl) coordination, i.e., the metal is connected to two ligands, as illustrated in the model of Figure 2.2b. This structure presents remarkable stability, being found up to a temperature of 570 K. Similarly, the codeposition of Fe and TPyB forms also a honeycomb structure, but with a small lattice parameter (≈ 1.4 nm), as shown in Figure 2.2c. This difference in size is due to the different interactions between the ligands and the metals. In this case, the TPyB molecules are three-fold coordinated with the Fe atoms. Despite the same shape of the nanostructure formed, we can manipulate the size of the network by changing the coordination metal.

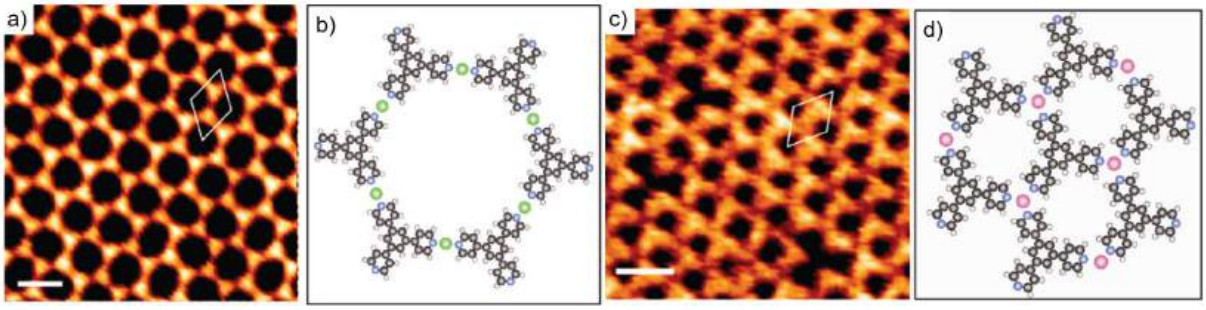

Figure 2.2: a) Honeycomb nanostructures obtained by Cu-coordinated TPyB molecules on Au(111); b) Molecular model showing the two-fold coordination of the Cu adatoms; c) Honeycomb network of TPyB molecules coordinated by Fe adatoms on Au(111) with the d) respective molecular model displaying the three-fold coordination of the molecules. Scale bar: 3 nm. c) Scale bar: 2 nm. C atoms in brown, N in blue, Cu in green, and Fe in pink. Adapted from [29].

Despite the morphological similarity of the nanostructures formed, the change in size dramatically affects the local as well as the macroscopic properties of the material. To demonstrate those changes, Piquero-Zulaica et al. coadsorbed dicarbonitrile molecules with three (Ph3) and six (Ph6) phenyl rings and Co atoms on Au(111), forming two honeycomb Co-coordinated structures with different sizes, as shown in Figure 2.3a and b [35]. In this investigation, the authors focused on exploring how the band structure changes as a function of the lattice constant. On both structures, there is a three-fold Co coordination between the molecules. After the MOF growth, they probed the band structure of the networks by using angle-resolved photoemission spectroscopy (ARPES), as displayed in Figure 2.3c and d. The formation of a porous nanostructure can be seen as a quantum dot array, where the surface states (SS) become confined. This confinement leads to a downshift in the band bottom ($\overline{\Gamma}$ point) as the pore size is reduced. This behavior occurs mainly due to the interaction between the substrate and the 2D-MOF overlayer formed.

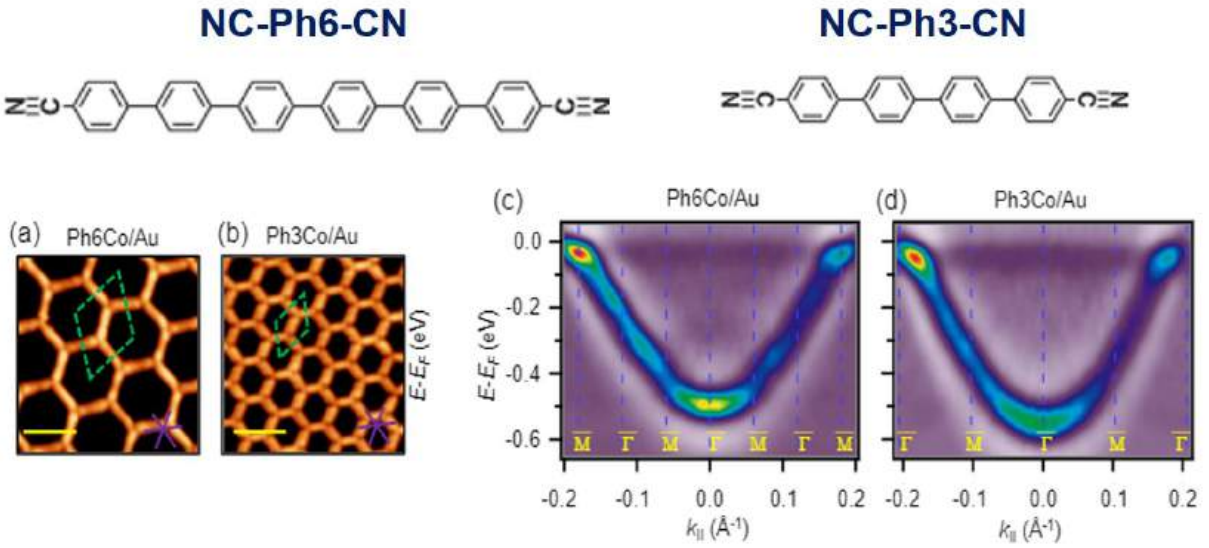

Figure 2.3: Honeycomb nanostructures formed by a) NC-Ph_6-CN and b) NC-Ph_3-CN molecules on Au(111). ARPES measurement obtained at 150 K for both c) Ph_6Co and d) Ph_3Co nanoporous networks. The band structure clearly shows a downward shift and gap opening. Adapted from [35].

Similarly, as in the synthesis of 3D-MOFs, we can explore a variety of functional molecular precursors to synthesize the two-dimensional frameworks. In addition to the honeycomb networks shown before, and depending on the molecules used and the metal coordination center, unique geometries can be obtained [36]. For example, Figure 2.4a displays a 2D-MOF with a square symmetry obtained on (111) surface, demonstrating the versatility of the synthesis [37,38]. In Figure 2.4a, the authors used 5,10,15,20-tetra(4-pyridyl)porphyrin (2HTPyP) molecules coadsorbed with Cu atoms on Au(111) to synthesize Cu-coordinated supramolecular networks [37]. The Cu adatoms (green balls in Figure 2.4a) coordinate with the four pyridyl groups in the molecular periphery. Metal adatoms are also incorporated into the molecular macrocycle through a process known as metalation. Due to the geometry of the 2HTPyP molecules, the network formed has square symmetry, with intermolecular head-on interactions. Figure 2.4b-d displays the formation of Kagome, rectangular, and rhombic networks, respectively, based on dicarbonitrile-sexiphenyl (NC-Ph6-CN) molecules on Ag(111). The formation of different pore shapes and sizes directly affects the electronic confinement. This is evident from the conductance spectra in Figure 2.4e and f measured at the center of the pores. The spectra display peaks with maxima at different energies. The synthesis of nanostructures with different shapes and sizes dramatically changes the electronic properties of the material due to the quantum confinement. For instance, 2D-Kagome and Archimedean can induce the emergence of flat bands due to the confinement of the surface states [39, 40].

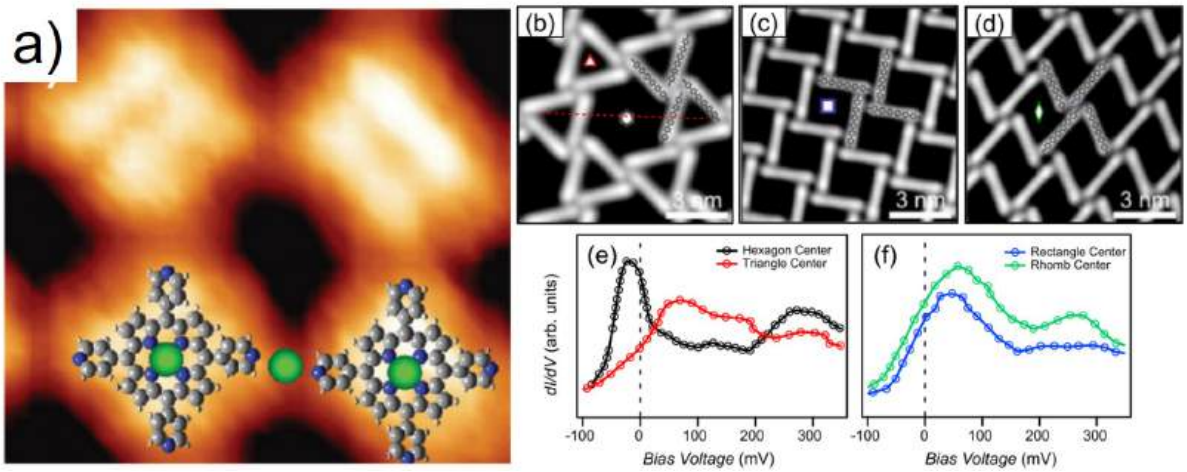

Figure 2.4: a) Square networks of 2HTPyP molecules on Au(111) coordinated by Cu adatoms with superimposed molecular structures. C in gray, N in blue, and Cu in green. Adapted from [37]; b) Kagome, c) rectangular, and d) rhombic nanoporous nanostructures formed on Ag(111), displaying the variety of geometries that can be obtained; e,f) Conductance spectra obtained in the center of the pores, revealing the confinement effects in the electronic density. Adapted from [38, 41].

The use of metals to change the supramolecular arrangement is a successful approach, with prominent examples [42–45]. However, less attention has been paid to the role of nonmetal atoms in the design of organic supramolecular nanostructures. For instance, nonmetal porphyrins were only synthesized recently, by incorporating Si atoms into

the macrocycle of a free-base 5,10,15,20-tetraphenylporphyrin (2H-TPP) [46]. In the case of metals, their interaction with the molecules can influence the semiconductor behavior of the supramolecular structure formed, due to their strong metallicity, changing the electronic states near the Fermi level [47]. By using nonmetals, we can still design new nanoarchitectures, while keeping their electronic properties. As a matter of fact, recent investigations using halogen adatoms combined with polyaromatic organic molecules have demonstrated the capability of nonmetals to induce supramolecular changes [48,49]. One challenge of this approach is to grow large-scale and highly-ordered nanostructures, for potential applications in nanoelectronics. Recently, the construction of a two-dimensional self-assembled network of 2,6-diphenylanthracene (DPA) molecules mediated by Br atoms (**a nonmetal atom**) on Ag(111) was reported [50]. The authors have demonstrated that the density of Br atoms on the surface dramatically changes the network morphology, due to the halogen–molecule interaction, as shown in Figure 2.5. This work opened the possibility to explore 2D halogen-coordinated nanostructures.

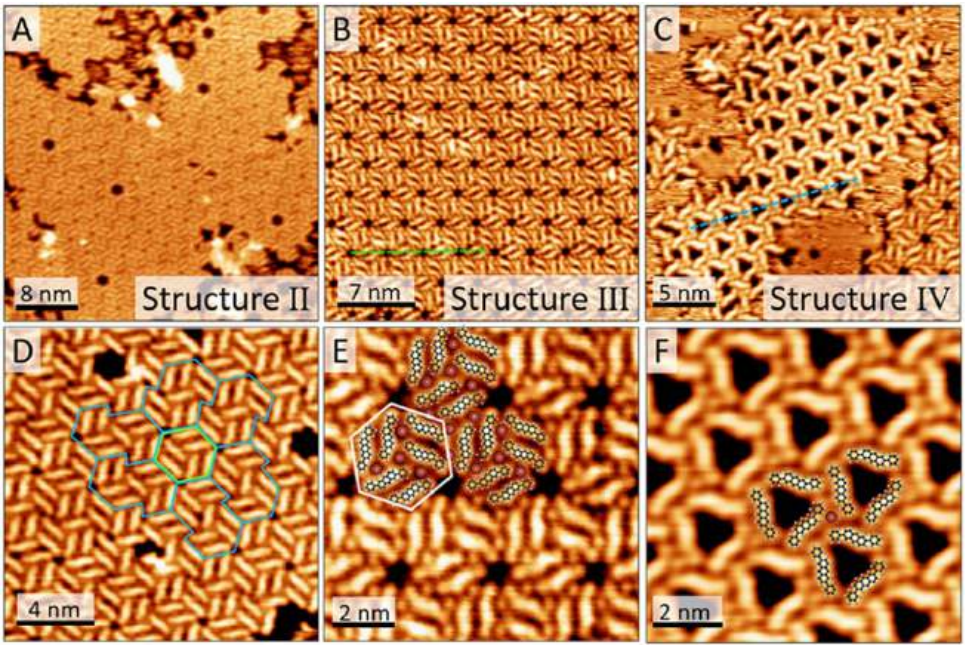

Figure 2.5: a-c) Br adatom-mediated nanostructures based on DPA molecules on Ag(111). The different structures obtained strongly depend on the Br adatom concentration on the surface. d-f) Zoom-in STM images of the nanostructures, showing the molecular arrangement, detailing the Br positions by the red balls. Adapted from [50].

2.2 Graphene nanoribbons

The search for carbon allotropes is constant in the scientific community, especially after the discovery of graphene (Gr) at the beginning of this century [51]. The graphene consists of an atomically flat carbon sheet arranged in a honeycomb fashion, as illustrated in Figure 2.6a. The arrangement can be seen as two interpenetrating triangular lattices of unit vectors represented by $\vec{a_1}$ and $\vec{a_2}$. The δ_1, δ_2, and δ_3 are the nearest neighbor-vectors of the honeycomb

lattice. The reciprocal-lattice is represented by the vectors $\overrightarrow{b_1}$ and $\overrightarrow{b_2}$, in Figure 2.6b, as well as its Brillouin zone. In the case of Gr, the C atoms hybridize in a sp^2 orbital, due to the overlap between the 2s, $2p_x$, and $2p_y$ states. The sp^2 orbitals bond to the C neighboring atoms in the plane. The other p orbital, $2p_z$, also called π orbital, remains unchanged and points orthogonally to this plane. The C atoms are bonded by σ-bonds through their sp^2 orbitals (sp^2–sp^2) while the π orbitals combined form a delocalized orbital above and below the Gr plane. The π electron delocalization gives graphene a high charge carrier mobility across the Gr plane. One of the most remarkable properties of Gr is its peculiar band structure, shown in Figure 2.6c. Complete modeling of the graphene electronic band structure can be obtained using the tight-binding approach [52, 53]. The calculated band structure shows a singularity in the energy dispersion at K and K' points, shown in the zoom-in image in Figure 2.6c, so-called Dirac points. The energy dispersion at both points in the Brillouin zone can be approximated by Equation 2.1.

$$E_{\pm}(\mathbf{q}) \approx \pm\, v_F|\mathbf{q}| + O[(q/K)^2] \tag{2.1}$$

where $\mathbf{q}$ is the momentum measured relatively to the K (or K') points and v_F = 1x10^6 m/s is the Fermi velocity. Here, there is a remarkable difference compared with the usual quadratic dispersion: the Fermi velocity does not depend on the energy or momentum. The Gr band structure linear energy dispersion gives rise to the so-called Dirac cones, where the valence and conduction bands overlap at one point. This defines graphene as a zero-bandgap semi-metal. For this purpose, the graphene sheet is not a good candidate for applications in nanoelectronics. In this context, many approaches have been explored in the last years to open the Gr bandgap such as substitutions doping [54,55], oxidation [56,57], intercalation [58,59], functionalization [60,61], etc.

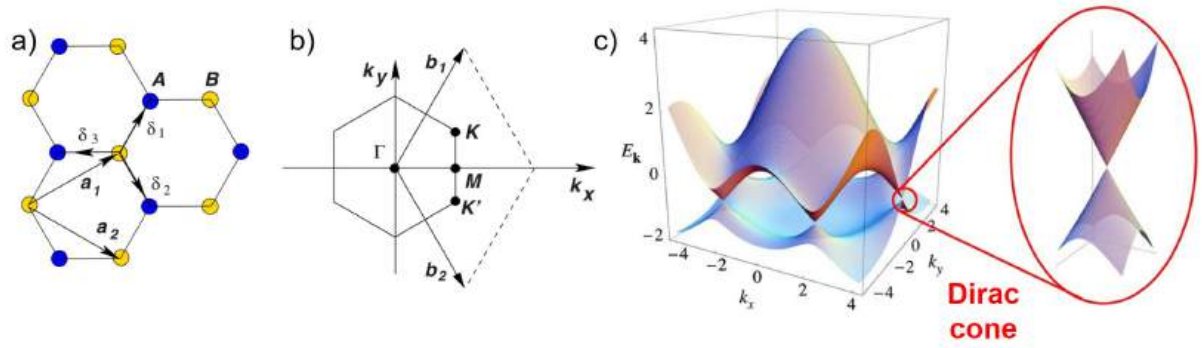

Figure 2.6: a) Gr lattice with primitive vectors $\overrightarrow{a_1}$ and $\overrightarrow{a_2}$ with their first neighbors (blue circles); b) Gr first Brillouin zone with the reciprocal lattice and the high-symmetry points; c) Electronic band structure of Gr obtained by tight-binding model, showing the linear dispersion at the Fermi energy (Dirac cone). Adapted from [53].

Another approach to engineering the band structure is to cut the graphene sheet in strips, forming quasi-one-dimensional nanoarchitectures: the graphene nanoribbons [62].

Their finite widths are the main ones responsible for the bandgap opening through the quantization of electron momenta in the transverse direction of the GNRs. The GNRs are classified following their edge termination and the typical ones are with armchair (AGNR) [63], zigzag (ZGNR) [64], chevron (cGNR) [65], and chiral (chGNR) [66] edges, as illustrated in Figure 2.7a.

In the case of AGNRs, theoretical calculations predicted that all of them are intrinsically semiconductors [67], as shown in Figure 2.7b. Moreover, they also present a bandgap width dependence, requiring further subclassification. The AGNRs can be defined as a function of the number of dimmer lines across the ribbon (N), as illustrated in Figure 2.7a, with an N = 7 AGNR in red.

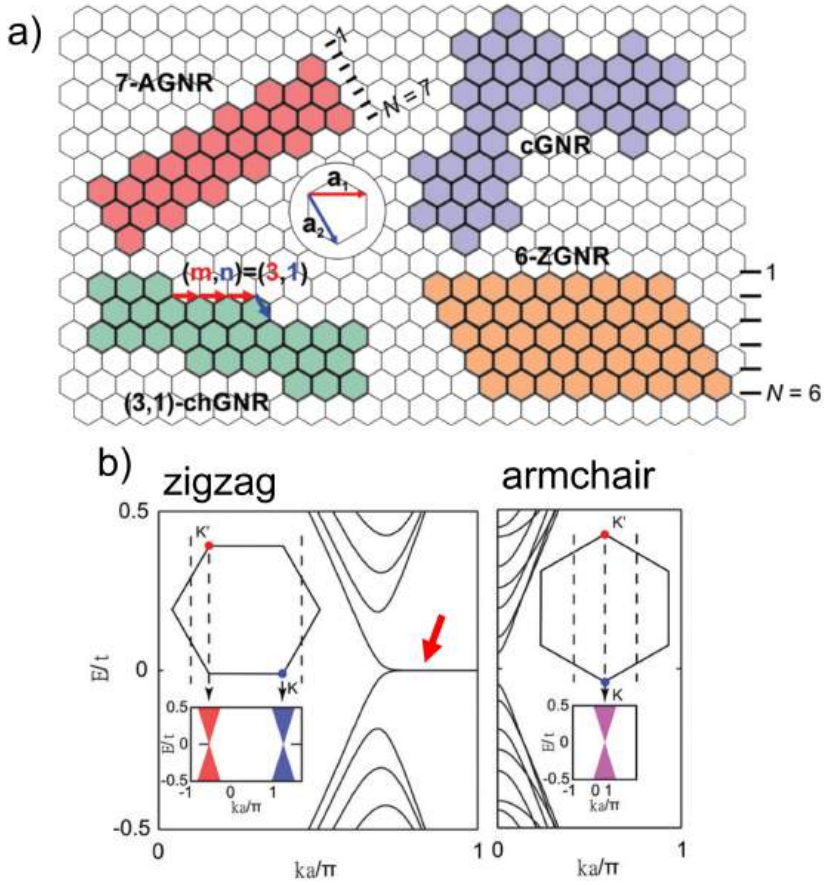

Figure 2.7: a) Graphene nanoribbons morphologies: armchair (AGNR), zigzag (ZGNR), chiral (chGNR), and chevron (cGNR) edge terminations; b) Electronic band structure of ZGNR and AGNR, showing the formation of flat bands (red arrow) for the ZGNR and bandgap opening for the AGNR. Adapted from [8].

The ZGNRs, on the other hand, have the highest valence band state and the lowest conduction band state degenerated at $k_a = \pi$. This originates a flat band at the Fermi level, as highlighted by the red arrow in Figure 2.7b, and becomes flatter as the GNR width is increased [68]. The emergence of those flat bands is explained by looking at the charge density distribution, which shows localized states in the edges that decay into the ribbon [69]. The cGNRs and chGNRs are both less common due to the challenging synthesis but both undergo topological phase transitions by narrowing their width [70, 71]. The most striking

property of the GNRs is their charge transport, where ballistic transport was experimentally demonstrated over several microns for GNRs epitaxially grown on SiC side wall [72, 73].

The electronic band structure of the GNRs can be further tuned by changing their morphology with the insertion of defects [74] and dopants [75]. By using surface-assisted synthesis routines heteroatoms can be easily introduced into the GNR. The doping can occur in two ways: at the edges [76] or the inner part [77] of the ribbon. Considering the heteroatom doping, nitrogen and boron are the two elements with great potential, due to the isoelectronic and isosteric behavior between C=C and B–N units [78]. This allows us to tune the electronic structure of the ribbon keeping the same morphology. Typically, B atoms are incorporated into the graphene ribbon while N and S are commonly attached to the GNR edges. The former leads to in-gap dopant bands, due to the hybridization of the extended π-system of the ribbon with the empty p_z orbitals of boron [79,80]. Figure 2.8a display a GNR unit doped with B atoms in their core obtained by on-surface synthesis [79]. By measuring STM images, the author found that the ribbon formed presents a bias dependence as shown in Figure 2.8b. In the region where the B atoms are located, marked with a purple cross in Figure 2.8a and b, the STM measurements show a distinct contrast, indicating a difference in the local electronic density of states. In the left image of Figure 2.8b the STM tip was biased with -3.0 V, and the region of boron appears as a bright spot while for the STM image with 3.0 V in the right, it appears dark. Since the voltage is applied in the STM tip in this case, the difference in contrast of the B sites depending on the bias voltage indicates that the boron is causing a perturbation in the GNR electronic structure as an electron-accepting unit.

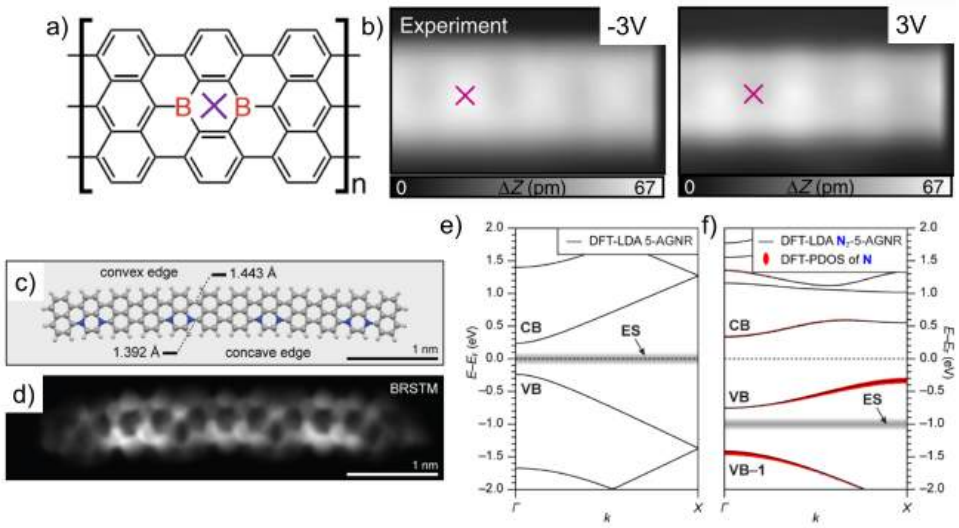

Figure 2.8: a) Molecular unit for AGNRs with B doping in their center; b) STM image of the synthesized B-doped AGNR measured at bias voltages of -3 and 3 V, showing the difference in the local density of states at the B position (purple cross). Adapted from [79]. c) Molecular model for N-doped 5-AGNR and its respective d) bond-resolved STM (BRSTM) image; DFT-LDA-calculated band structure for the e) undoped 5-AGNR and f) N-doped 5-AGNR, highlighting the contribution of molecular orbitals with nitrogen character in red. Adapted from [75].

In the case of N-doping in the core of the GNRs, it can induce changes in the electronic properties that are even more pronounced. Figure 2.8c and d, depict the structure

and the bond-resolved STM image of a 5-AGNR with N doping in its core, respectively [75]. Comparing the calculated band structure of the 5-AGNR with its N-doped counterpart shows that the heteroatom doping in the core changes the band structure from a direct to an indirect gap semiconductor, as shown in Figure 2.8e and f. Such results are also corroborated by scanning tunneling spectroscopy measurements [75]. In this context, heteroatom doping has been successfully employed to engineer the band structure of GNRs.

The GNR properties are strongly sensitive to their morphology at atomic and molecular levels. In this context, their synthesis requires a fine fabrication method with such precision. For instance, many efforts to construct these ribbons have been employed based on both, top-down and bottom-up strategies. Among the top-down methods we can cite the unzipping of graphene nanotubes [81, 82] and electron beam lithography [83, 84]. Both top-down approaches have low sensitivity to tune the GNR structure, except for their width. In this context, tuning the ribbon structure requires a method with atomic and molecular sensitivity and the surface-assisted routes allow us to achieve such precision.

The on-surface synthesis consists of adsorbing molecular precursors on a templating substrate, usually on a single-crystal surface under UHV conditions, confining the molecular reaction on a two-dimensional environment [85]. The crucial aspect of this method is to choose the molecular building blocks and the templating surface carefully. The former typically has functional groups that will be responsible for the molecule-molecule and molecule-substrate interactions. The surface will catalytically activate the reactions and also define the morphology of the nanostructure formed depending on its symmetry. This stepwise approach presents great success in the synthesis of polymeric nanostructures such as doped and functional graphene sheets [86], kagome lattices [87], and porphyrin-based networks [88]. One of the most powerful synthesis routes to obtain such materials is the Ullmann coupling on coinage metal surfaces [89, 90]. This approach consists of the reaction between aryl halides to form aryl-aryl bonds.

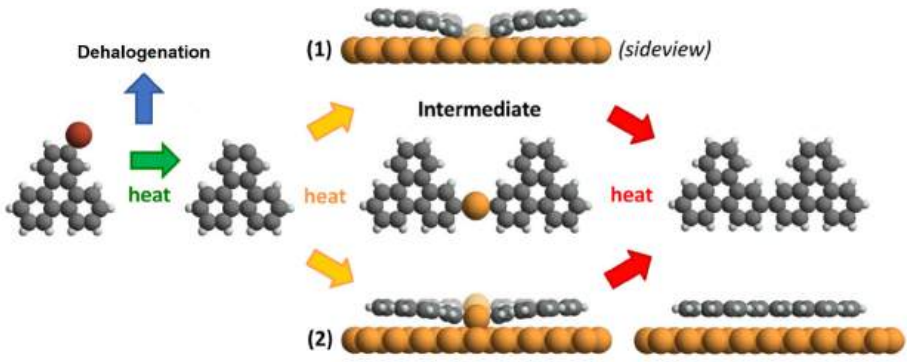

Figure 2.9: Ullmann coupling reaction scheme showing all reaction steps towards the covalent bonding formation. C in gray, Br in red, H in white, and metal in orange. Adapted from [9]

The Ullmann reaction mechanism can be separated into two pathways, as illustrated in a simple picture in Figure 2.9. The reaction is based on halogenated organic pre-

cursors containing C–X (X = F, Cl, Br, I) functional groups (aryl halides), typically at the molecular periphery. In this case, the reaction energy barriers are both molecule and substrate-dependent [91]. The first step consists of the cleavage of the C–X bonds followed by the coupling between the dehalogenated precursors. The C–X bond dissociation occurs upon deposition on the metal surface at a wide range of temperatures depending on the substrate chosen [92, 93]. The precursor's coupling typically forms an intermediate state that consists of (1) a bond with a surface atom through the C radical or (2) the formation of organometallic complexes, C–M–C (M = metal), as displayed in Figure 2.9. Finally, upon heating the molecules can bond through C–C coupling, forming polymeric nanostructures [94, 95].

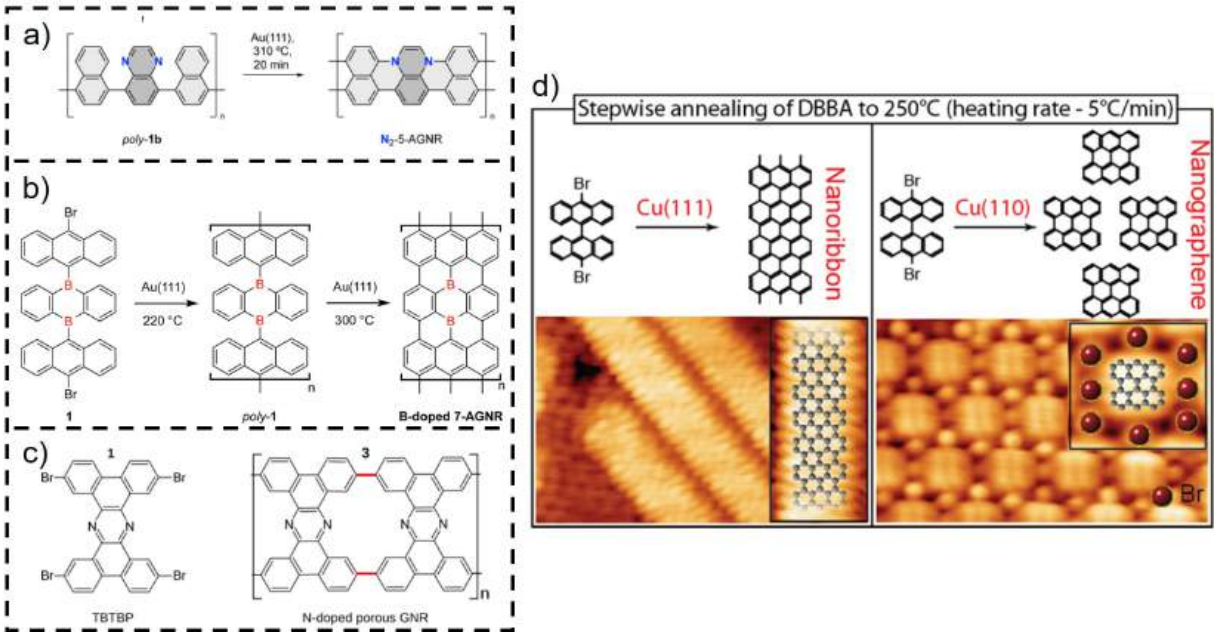

Figure 2.10: a) N-doped 5-AGNR with the heteroatom at the edge position. Adapted from [75]; b) Heteroatom doping at GNR center with B atoms. Adapted from [77]; c) Porous and N-doped AGNR with the molecular precursors connected by sigma bonds, highlighted in red. Adapted from [96]; d) DBBA molecules adsorbed on Cu(111) and Cu(110), leading to the formation of GNRs and nanographene, respectively. Adapted from [97]

The surface-assisted Ullmann reaction allows us to obtain atomically precise GNRs, as depicted in Figure-2.10a-c. The structures show different doping atoms at the core and the edge of the ribbon. In Figure 2.10b, the GNR is formed in two steps: the Ullmann reaction to bond the molecular precursors upon heating at 220 °C followed by cyclodehydrogenation after annealing at 300 °C. This is the typical synthesis route for the growth of GNRs. However, depending on the building block, only the Ullmann reaction is necessary to form the ribbon. In Figure 2.10c, the ribbon is already formed after the C–C coupling. In this specific case, beyond N doping, the GNRs also have pores, forming N-doped porous GNRs.

Figure 2.10d shows the stepwise synthesis of 10,100-dibromo-9,90- bianthracene (DBBA) molecules on two distinct substrates: Cu(111) and Cu(110) [97]. On Cu(111), the DBBA molecules are intact at -120 °C while on Cu(110) they are already partially debrominated at the same temperature. This is clear evidence of how the surface reactivity changes

with the packing. Upon heating at 250 °C on Cu(111), the DBBA precursors follow the Ullmann reaction forming 7-AGNRs. In contrast, the same molecules form nanographene, due to the high anisotropy of the surface, which blocks the molecular units to covalently bond to each other. The surface packing is a key player in the synthesis of GNR using DBBA molecules.

In summary, the electronic properties of the GNRs have a strong dependence on their morphology, especially their width and edge termination. The HOMO-LUMO gap in armchair GNRs is more pronounced for very short ribbons with lengths limited to 3 nm [98]. For longer ribbons, this effect is less pronounced. In addition, heteroatom doping also affects the ribbon band structure, depending on both the type of the dopant as well as its position in the GNR structure. The atomic control over the dopant location in nanomaterials has proven to be a great challenge in materials synthesis [54].

In this context, we will demonstrate the synthesis of doped 7-AGNRs. The heteroatom dopants are located in well-defined positions in the ribbon, demonstrating the atomic precision of our synthesis. Moreover, combined with previous results from our group, we will show that the growth of this unique GNR is independent of the substrate orientation used. Our findings open the possibility of exploring the TBTBP molecular precursor on a variety of substrates to produce uniform doped graphene nanoribbons, even on polycrystalline surfaces.

Chapter 3

Experimental Methods

3.1 Scanning Tunneling Microscopy (STM)

The development of nanotechnology in the last decades was mainly due to the invention of STM in 1981 by Gerd Binnig and Heinrich Rohrer [99]. Afterward, other scanning probe microscopes (SPM) were developed such as atomic force microscopy in 1985 [2], and recently with the qPlus sensor invention, it is possible to measure both STM and AFM in parallel [100]. These techniques allowed real-space imaging at the Angstrom scale with atomic and molecular bond resolution. The SPM can be used in a wide range of environments, such as high pressures [101], ultra-high vacuum [102], liquids [103], insulators [104], etc. This invention opened several possibilities in the nano-sized area from imaging to manipulation.

3.1.1 Tunneling: elementary model

The tunneling effect can be modeled in a simple picture considering a free particle in a one-dimensional potential barrier $U(z)$. In classical mechanics, if the particle's energy E is lower than the potential barrier ($E < U(z)$), the particle is confined since the region inside the barrier is classically forbidden. However, in quantum mechanics if the barrier is finite ($|U(z)| < \infty$), the particle has a non-zero probability to be found inside the potential barrier. To describe this behavior, let's consider a particle of mass m traveling in a finite potential barrier of height $U(z) = U_0$ and width d, as illustrated in Figure 3.1. By solving the time-independent Schrödinger equation,

$$-\frac{\hbar^2}{2m}\frac{d^2\psi(z)}{dz^2} + U(z)\psi(z) = E\psi(z) \tag{3.1}$$

we find the wavefunctions ψ which describe the particle's behavior. Considering the case where the particle is initially in the region I with $E < U_0$, the solutions are given by:

$$\psi^I \propto e^{ikz} + e^{-ikz} \tag{3.2}$$

$$\psi^{II} \propto e^{\beta z} + e^{-\beta z} \tag{3.3}$$

$$\psi^{III} \propto e^{ikz} \tag{3.4}$$

where $k = \frac{\sqrt{2mE}}{\hbar^2}$ and $\beta = \frac{\sqrt{2m(U-E)}}{\hbar^2}$.

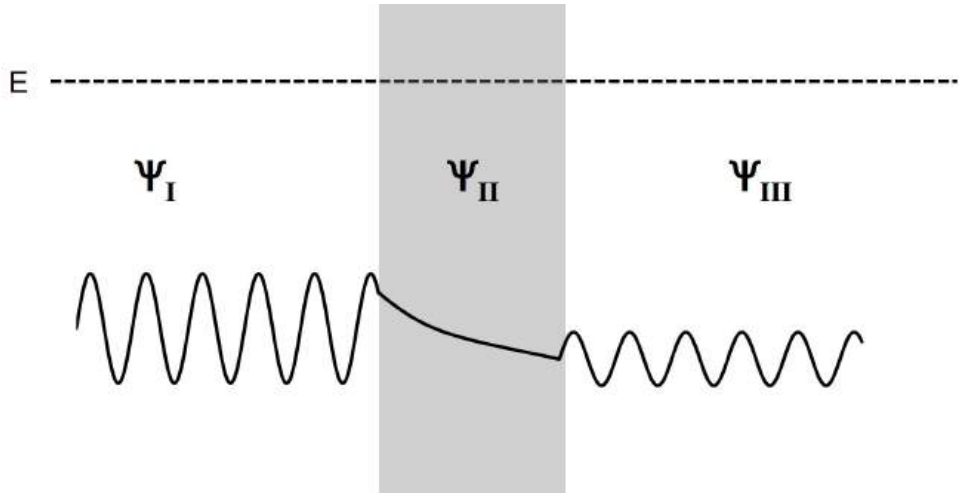

Figure 3.1: Tunneling effect one-dimensional model for a finite potential barrier.

The solutions of Schrödinger equation tell us that in the classically forbidden region (II), $|\psi^{II}|^2 \neq 0$, i.e., the particle can be found inside the barrier. If the width d is sufficiently small, the particle can be transmitted from region I to III through the potential barrier. The transmission coefficient T can be defined as the probability ratio between the incident and transmitted wavefunctions as follows:

$$T = \frac{|\psi^{III}(d)|^2}{|\psi^{I}(0)|^2} \propto e^{-2\beta d} \tag{3.5}$$

If the particle is an electron we can infer that the tunneling current depends exponentially with the distance between the regions I and III. This is the simplest picture of the STM tunnel junction, if we identify region I as the sample and III as the STM tip. Moreover, for metals their work function $(U-E) \equiv \phi_T \equiv \phi_S \approx 5$ eV implying that $\beta \approx 1$ Å^{-1} which means that the tunneling current decays one order of magnitude per angstrom.

3.1.2 STM: fundamental aspects

The STM working principle is based on the approach of an atomically sharp tip to a substrate, both metallic. The tip is attached to piezoelectric ceramics which control the XYZ movement of the tip with respect to the sample, as illustrated in Figure 3.2a. Such a piezo controller can keep the tip and sample separated by sub-angstrom distances, in which the wavefunctions of both electrodes overlap. Suppose a bias voltage (V) is applied between them. In that case, the Fermi levels of the tip and sample are now shifted by eV, and electrons can flow from the sample to the tip and vice-versa, depending on the bias polarity, as displayed in Figure 3.2b. Hence, the STM is a powerful technique that can probe both occupied and unoccupied states of a sample.

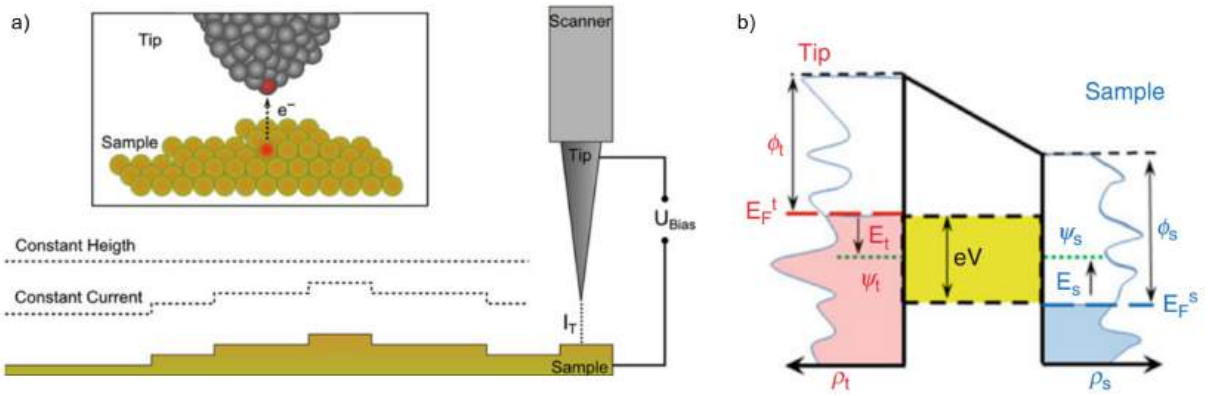

Figure 3.2: a) STM tunnel junction with the illustration of the two typical scanning modes: constant current and constant height. Adapted from [3]; b) Tunneling process between tip and sample. For positive bias applied in the sample, unoccupied electronic states of the sample are probed. For negative bias voltages, occupied sample electronic states are probed. Adapted from [105].

The STM measures the tunneling current (I_t) between two electrodes. The equation 3.5 tells us that the transmission coefficient of a tunnel junction depends on the width of the barrier, which in the case of STM is tip-sample distance. A more formal way to express the tunneling current was performed by Bardeen [106]. The Bardeen tunneling theory treats the electron tunneling phenomena as a one-particle process, neglecting the mutual interaction between the electrons, and considering the elastic tunneling case. Assuming a step function for the Fermi distribution function, the tunneling current can be written as follows:

$$I = \frac{4\pi e}{\hbar} \int_0^{eV} \rho^T(E_F^T - eV - \epsilon)\rho^S(E_F^S - \epsilon)|M^{TS}|^2 d\epsilon \tag{3.6}$$

where ρ^T, E_F^T, ρ^S, and E_F^S are the density of states and Fermi energy for the tip and sample, respectively. The tunneling matrix M^{TS}, is a surface integral that describes the projection of an initial state of the sample, perturbed by the potential $U(z)$ onto a final state of the tip and vice-versa. In other words, this matrix considers the coupling between the states of the sample and the tip perturbed by the potential of the barrier. Tersoff and Hamann [107, 108] further optimized the Bardeen theory by modeling the tip states by a radially symmetric wavefunction, $\psi(\mathbf{r}) \approx Ae^{-k\mathbf{r}}/\mathbf{r}$. The main prediction of the Tersoff-Hamann theory is that the tunneling current depends on the local density of states (LDOS) at the center of the tip. The tip states can be further approximated with more complex calculations by modeling the tip as p- or d-like orbitals [109].

The two typical modes of STM operation are the constant-height and constant-current modes, as illustrated in Figure 3.2a. In the former, the tip scans the sample surface at a fixed distance z, mapping the DOS of the sample. In the constant-current mode, the STM adjusts the tip-sample distance z to keep the tunneling current at a fixed setpoint value. In this mode, the image is a topographic view of the sample which depends also on the DOS of the sample, since the tunneling current consists of the integral of the DOS.

Moreover, by taking the derivative of the tunneling current with respect to the

bias voltage in equation 3.6:

$$\frac{dI}{dV} \propto \rho^S(eV) \tag{3.7}$$

we can obtain the local density of states of the sample by measuring the variation of the tunneling current as a function of the applied bias voltage.

3.2 X-ray Photoelectron Spectroscopy (XPS)

Photoemission spectroscopy (PES) is one of the most powerful techniques in surface science to probe the chemical and electronic states of atoms, molecules, solids, and liquids. The photoemission phenomenon was observed in 1887 by Hertz and explained later in 1905 by Einstein. From the 50s to the 70s, Kai Siegbahn developed the instrumentation to perform spectroscopy measurements for chemical investigations, also known as electron spectroscopy for chemical analysis (ESCA) or more commonly nowadays as X-ray photoelectron spectroscopy (XPS). The technique is based on the photoelectric effect where incident X-ray light ejects photoelectrons from the sample, which are counted as a function of the kinetic (or binding) energies. This gives a chemical fingerprint of the chemical species present in the sample.

3.2.1 Photoemission phenomena

The photoemission is described by the photoelectric effect, where light with energy $\hbar\omega$ shines the material, promoting electrons from an occupied state with binding energy ϵ_B to states above the vacuum level (see Figure 3.3a). For electrons in a material of work function ϕ, their kinetic energy ϵ_K is given by [110]:

$$\epsilon_K = \hbar\omega - \epsilon_B - \phi \tag{3.8}$$

The energy distribution of equation 3.8 suggests that the photoemission spectrum is a one-to-one mapping of the occupied states in the sample. However, several phenomena can affect the energy distribution, making this simple mapping more complicated [111]. Figure 3.3b, illustrates a typical photoemission spectrum, with some of the main features observed in photoemission spectroscopy. The elastic lines are related to the characteristic peaks of the sample (core levels and valence band) and result from elastic scattering. In the X-ray energy range (100 - 1500 eV), the photons penetrate several hundreds of nanometers in the material. Since the electrons possess a very short inelastic mean free path, we expect that the electrons excited in regions deeper in the solid will reach the surface after one or several inelastic losses. This random process produces the inelastic background in Figure 3.3b. Finally, the electrons that suffered multiple inelastic scattering and are emitted with low kinetic energies (high binding energies) produce the secondary electrons peak. If the kinetic energy losses are quantized, another contribution to the PE spectrum can appear known as satellites [112].

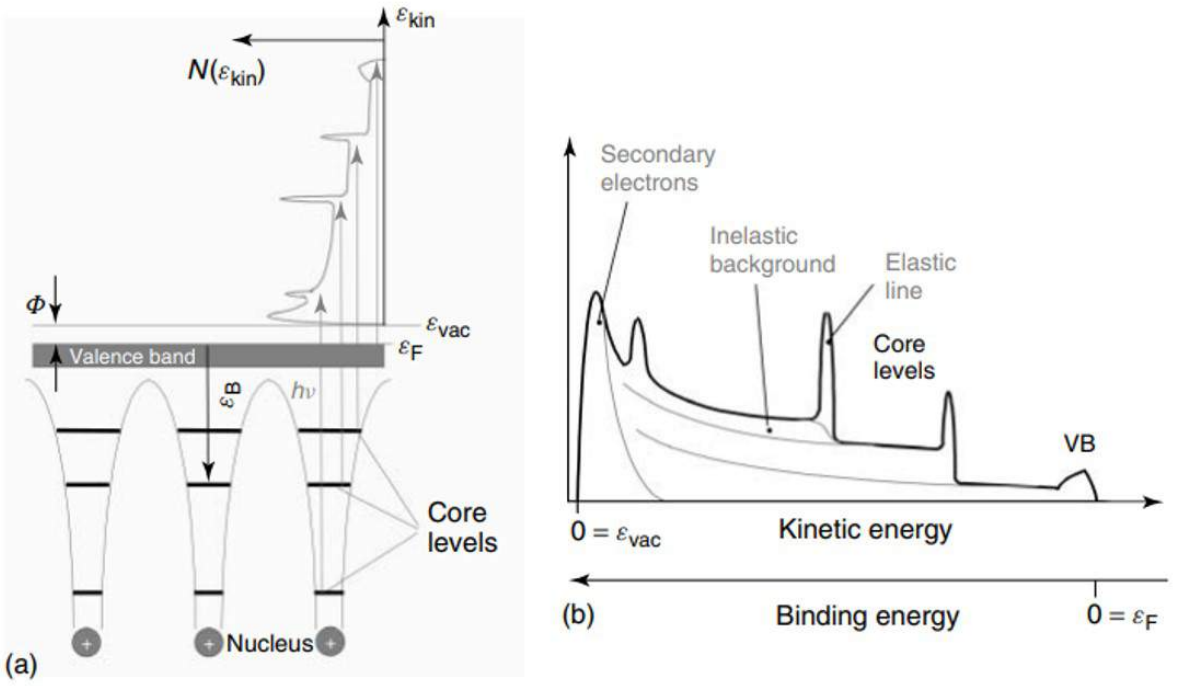

Figure 3.3: a) Photoemission diagram showing the relation between the occupied states of a material by absorbing a photon with energy $h\nu$; b) Illustration displaying the main features that compose the XPS spectrum. Adapted from [111].

In addition to the inelastic scattering, another important effect typically present in the PE spectrum is the Auger electrons. This effect occurs due to a relaxation process of the excited state created after photoemission. After photoelectron emission, a vacancy is created which is filled by an electron from a less bounded state, releasing the excess of energy. This released energy only depends on the two states involved. This excess of energy would cause two main processes depending on the order of magnitude of the energy involved. For low energy process (1 keV), the Auger effect is predominant while for high energies (10 keV) the emission of X-rays emission prevails [113]. For XPS, the main contribution is the Auger lines, where the energy excess is released by emitting an electron. Since the energy involved depends only on the energy difference between the levels, the Auger peaks in the XPS spectrum are independent of the excitation energy.

The core level peaks have a characteristic binding energy, which is related to their chemical environment. The core level binding energies give not only the elemental composition of the sample but also the so-called chemical shifts, which is often the most valuable information. When a chemical bond is formed, electrons from the valence band change their spatial distribution which induces a shift in the atomic core levels. This gives a fingerprint of the formation of ionic and covalent bonds as well as the oxidation state of the elements forming the sample. Figure 3.4 illustrates the chemical shift at the N 1s core level after the metalation of 2H-tetraphenylporphyrin (2HTPP) molecules [114]. The intact molecule (Figure 3.4b) presents two peaks at the N 1s core level (green arrows) assigned to the –N= and –NH– species in a 1:1 ratio. After the molecule undergoes a metalation reaction, i.e., a metal

atom is incorporated into the molecular core, only one peak is observed in the N 1s. This is evident in Figure 3.4c, where a Cu atom is bonded to the four N atoms in the porphyrin core, changing the N 1s core level peak to one chemical species only (blue arrow).

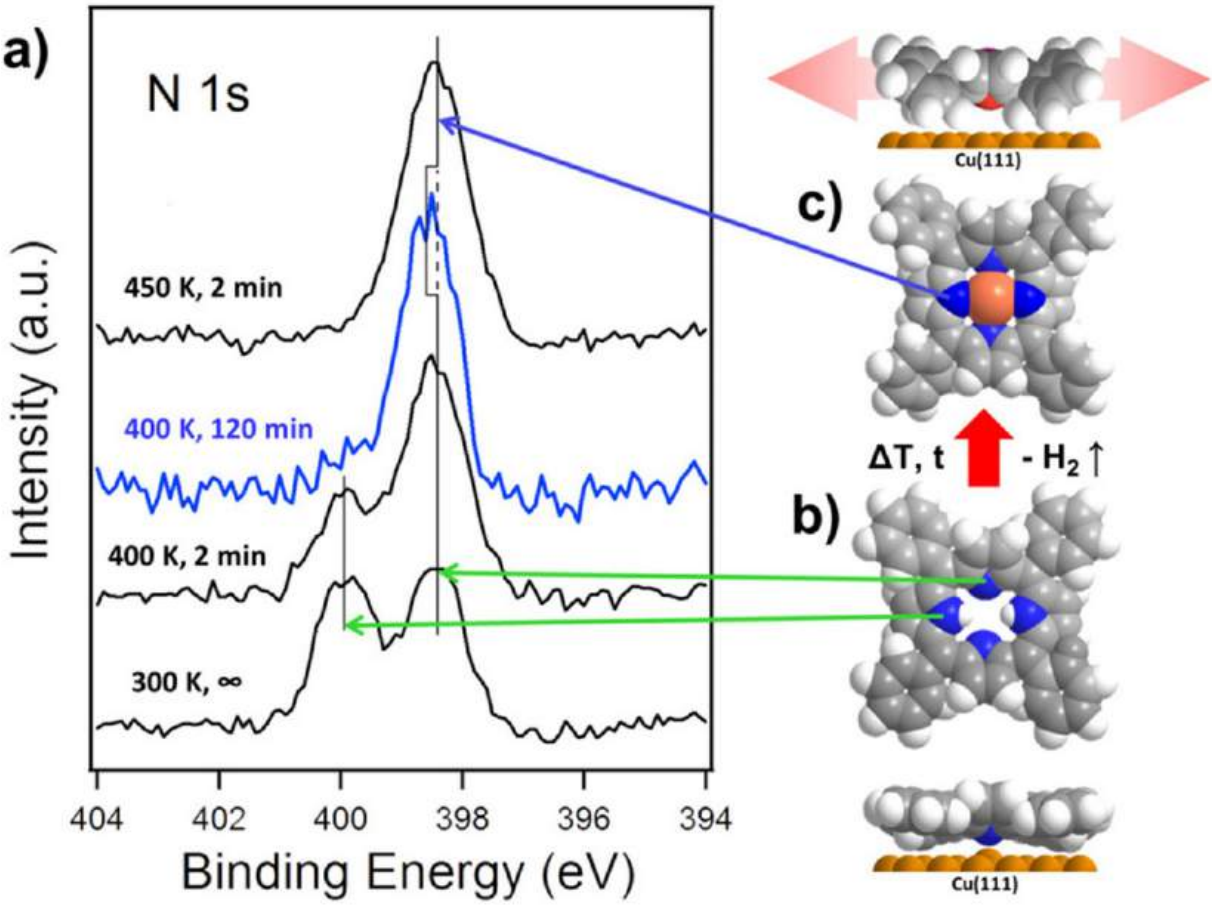

Figure 3.4: a) XPS spectra of the N 1s core-level of 2HTPP molecules showing the contributions of the iminic (-N=) and pyrrolic (-NH-) nitrogen for free-base molecules (300 K) and Cu-metaled molecules (400 K); b) Free-base 2HTPP and c) Cu-metaleted 2HTPP molecules. Adapted from [114].

3.2.2 Surface sensitivity

The XPS is a powerful technique for surface science analysis. The XPS probe depth is restricted to a few surface layers of the material (typically 2 - 10 atomic layers). Figure 3.5 displays the inelastic mean free path (IMFP) of the electrons (dots) which can be described by a universal curve (solid line). For typical X-ray energies (100 - 1500 eV), the electrons IMFP is around 5 nm. Therefore, the inelastic photoelectrons are emitted from the few atomic layers of the sample.

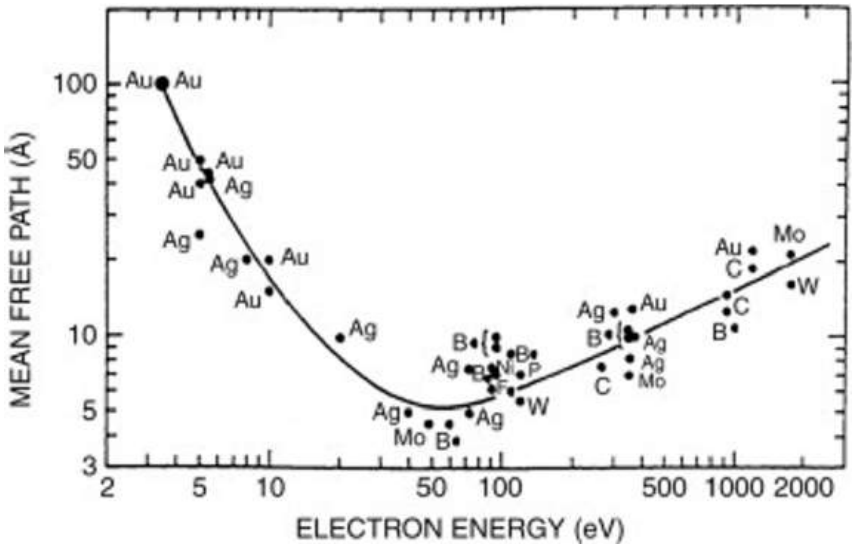

Figure 3.5: Universal curve of the inelastic mean free path (IMFP) of electrons in solids. Adapted from [115].

The surface sensitivity can be further tuned by varying the angle between the sample and the electron analyzer, θ. Such behavior is described by the Beer-Lambert law (see equation 3.9) which relates the flux of inelastic electrons I which travels through a thickness d with an IMFP λ. The parameter I_0 is a reference intensity measured at a given angle, usually $\theta = 0°$. For an exciting energy of Al Kα source, the IMFP ranges from 1 to 3.5 nm, which gives a sample depth in the order of 3 to 10 nm. In order to have a better surface sensitivity, we can vary θ to grazing angles, making the depth analyzed shallow. The Beer-Lambert law is also a useful tool for the determination of the thickness d of thin films through angle-resolved XPS (ARXPS). In summary, the XPS is a powerful surface analysis tool to determine the chemical composition of the 2D material formed on a templating surface, complementing the STM measurements.

$$I = I_0 e^{\frac{-d}{\lambda cos\theta}} \tag{3.9}$$

3.3 Experimental Setup

Figure 3.6 displays the surface science experimental setup used in all experiments performed during this thesis. The equipment is located in the Department of Applied Physics of the Gleb Wataghin Institute of Physics at the University of Campinas (UNICAMP). This UHV facility belongs to the Surface Science Group (GFS) and consists of two interconnected chambers: XPS/Preparation and STM. The former operates at a base pressure in the low 10^{-10} mbar while the latter at low 10^{-11} mbar. The XPS/preparation chamber is equipped with a conventional X-ray source (Al and Mg Kα), a SPECS Phoibos 150 hemispherical electron analyzer, an ion gun for sputtering, low energy electron diffraction (LEED) optics for crystallographic characterization, Knudsen cell and e-beam evaporators for molecular and metal deposition, respectively. The chamber also has a manipulator with a filament and high-voltage supply for electron bombardment for sample cleaning and reconstruction.

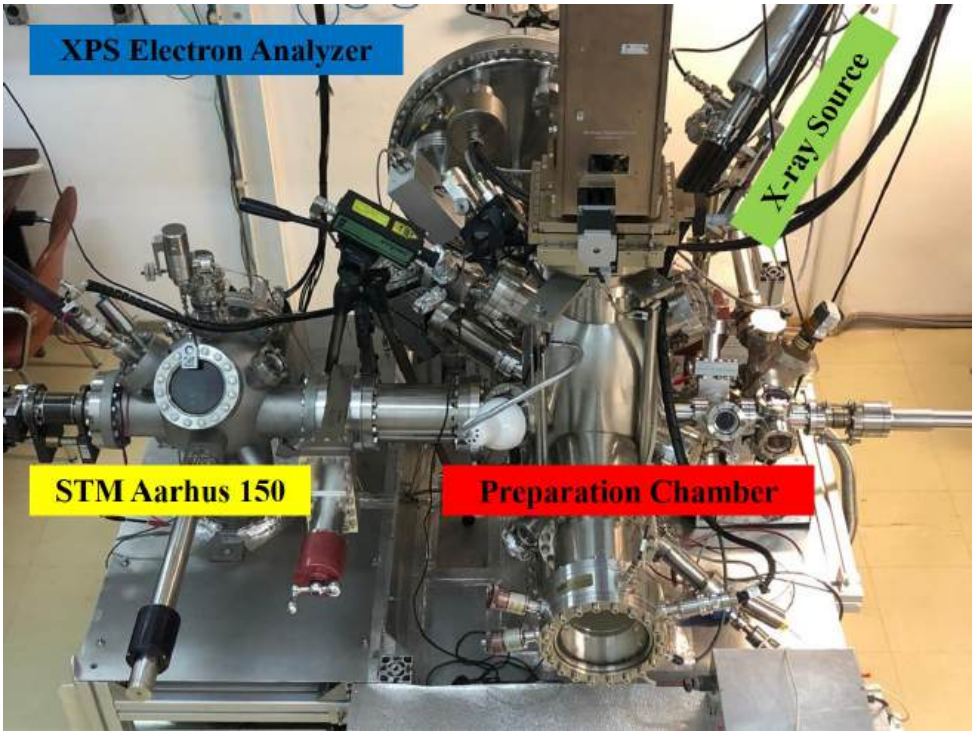

Figure 3.6: Experimental setup used in the experiments performed during this thesis in the Surface Science Group (GFS) at Unicamp.

STM

The SPM chamber is equipped with a variable temperature (VT) STM SPECS Aarhus 150 (see Figure 3.7a), with a SPECS SPC 260 controller. The microscope can operate in temperatures ranging from 100 K to 400 K. The cooling system is through a flux of liquid nitrogen and the heating is performed by a Zener diode, mounted in a massive block, a so-called cradle. The damping system consists of Viton rubber bands attached to the cradle to reduce undesired vibrations.

Figure 3.7b shows a zoom image of the STM stage, with the STM tip highlighted by the red arrow. The tip is mounted over a platform that consists of piezoelectric ceramics for controlling the approaching (z-direction) and scanning (xy-directions). All experiments of this thesis were performed in the constant current mode using a W tip. Moreover, the STM chamber is also equipped with an ion gun for tip preparation.

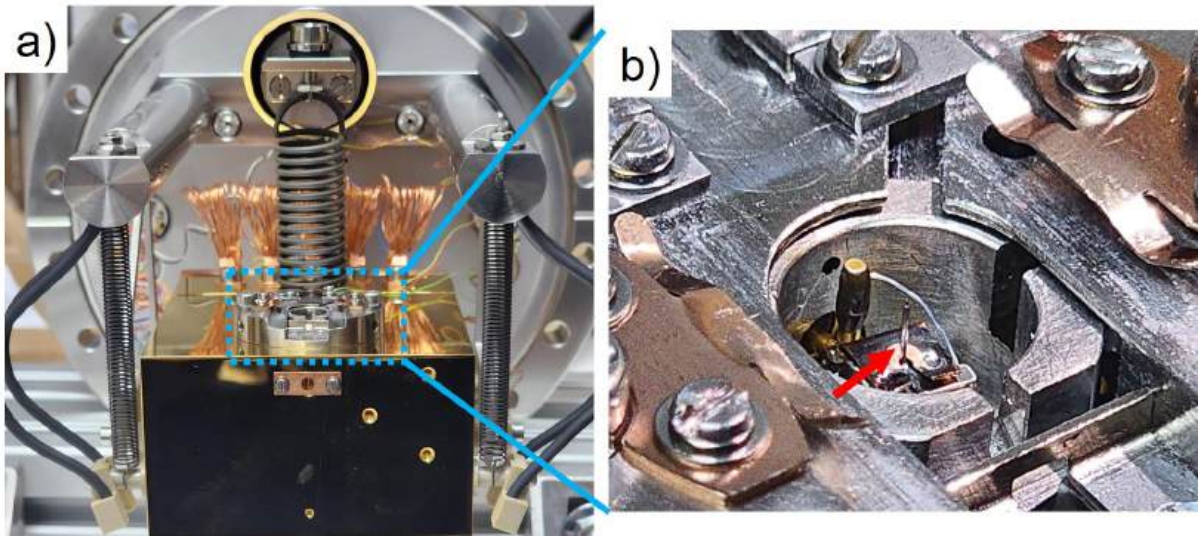

Figure 3.7: a) STM SPECS Aarhus 150 stage and b) zoom image of the STM tip (red arrow).

XPS

The XPS measurements were performed using a hemispherical electron analyzer (HSA) similar to the one shown in Figure 3.8a. After being emitted from the sample, the photoelectron passes through a system of electrostatic lenses and is focused in the entrance slit (see Figure 3.8b). This defines the analysis area as well as the acceptance angle. After focusing on the entrance slit, the photoelectrons enter the hemispherical region, which consists of the inner and outer hemispheres.

All XPS measurements of this thesis were performed operating the HSA in the Fixed-Analyzed Transmission (FAT) mode. In this mode, the voltage difference applied to the outer and inner hemispheres ($V_{out} - V_{in}$) is constant, or E_{pass} = constant (see Figure 3.8b). The electron collection is very dependent on the electrostatic lenses placed before the entrance slit. The electrostatic lenses both focus the electrons at the entrance slit and reduce their velocity. Consequently, the electron kinetic energy is reduced to match the pass energy of the hemispherical analyzer.

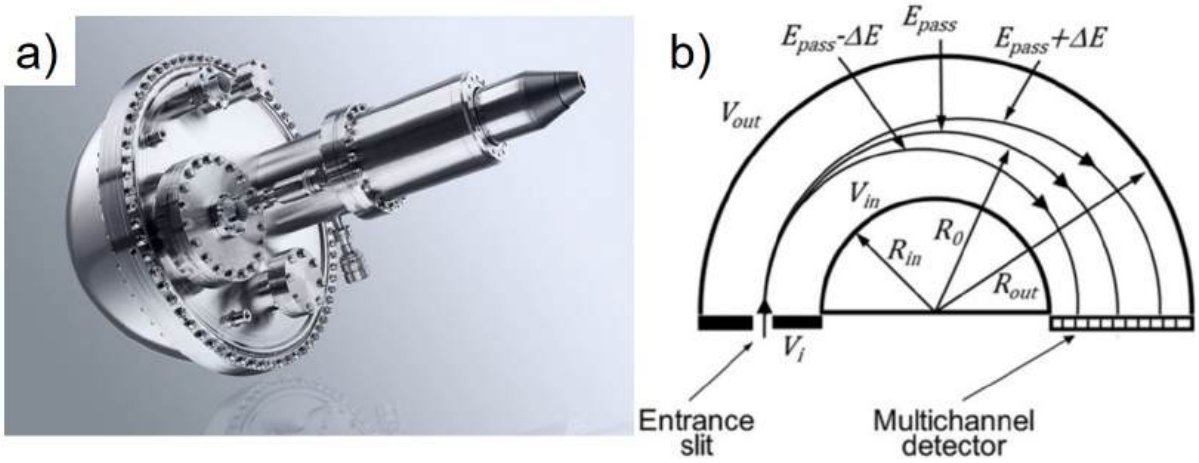

Figure 3.8: a) SPECS Phoibos 150 hemispherical electron analyzer; b) Schematics of the electron trajectories in the hemispherical electron analyzer.

The electrons traveling along the equipotential plane of the HSA, $R = (R_{in}+R_{out})/2$, have an energy given by E_{pass}. This energy is defined by the electrostatic lens. Only the photoelectrons in a range of energy $[E_{pass}-\Delta E; E_{pass}+\Delta E]$ hit the multichannel detector located at the exit of the HSA. The energy resolution for an entrance slit of width W and an acceptance angle α is given by the equation 3.10. The photoelectron energy is thus scanned by varying V_{out} and V_{in} and generating an intensity vs. energy spectrum.

$$\Delta E = E_{pass}\left(\frac{W}{2R} - \frac{\alpha^2}{2}\right) \tag{3.10}$$

3.4 Sample preparation

Surface preparation

All samples presented in this thesis were prepared *in situ* in a UHV environment. Such preparation guarantees that the surface analyzed has a low degree of contamination. The metal substrates were prepared by applying a standard surface science procedure consisting of cycles of sputtering followed by annealing of the metal monocrystal. The sputtering was performed using Ar^+ to physically remove most of the undesired contamination (O_2, H_2O, CO, CO_2, etc) of the surface. The next step consists of a heat treatment to remove further contaminations of the substrate but, most importantly, reconstruct the surface. The annealing temperature is often set as 50-60% of the melting point of the substrate material. This last procedure allows the formation of an atomically flat surface with large terraces, which is mandatory for the STM measurements and for the growth of the low-dimensional materials synthesized in this thesis. In our experimental setup, the annealing process is performed by homemade software that controls the heating and cooling ramps as well as the annealing temperature. To obtain long terraces ($\geq$ 1000 Å in our case) a slow heating ramp and most importantly a very slow cooling rate are mandatory. For all substrates used, the heating and cooling rates were 0.8 K/s and 0.3 K/s, respectively. The surface cleanliness and ordering were then verified by LEED and STM measurements.

Figure 3.9a-c displays the STM measurements of the three clean substrates used in this thesis: Cu(111), Ag(111), and Ag(110). The inset images show the atomic resolution of each substrate. Such high-resolution images are used to calibrate the STM images measured afterward and to determine the high-symmetry directions of the surface. The atomic resolution measurements of well-known surfaces and materials are mandatory in our case to calibrate the STM piezo distortions. All STM images presented in this thesis were post-calibrated using the Gwyddion software [116] based on different atomic resolution images of different metal substrates. The bottom image in Figure 3.9a display the atomic-resolved STM measurement of the Cu(111) surface. The blue arrows in the inset images show the lattice vectors of the (111) surface. The lattice constant found is (2.54 $\pm$ 0.05) Å. Similarly, the bottom image in Figure 3.9b and c shows the atomic resolution STM measurement for the Ag(111) and Ag(110) surfaces, respectively. The lattice constant for the hexagonal surface of Ag is (2.86 $\pm$ 0.05) Å. For the rectangular Ag(110) surface, we found lattice constants of (2.85 $\pm$ 0.06) Å and (4.12 $\pm$ 0.06) Å.

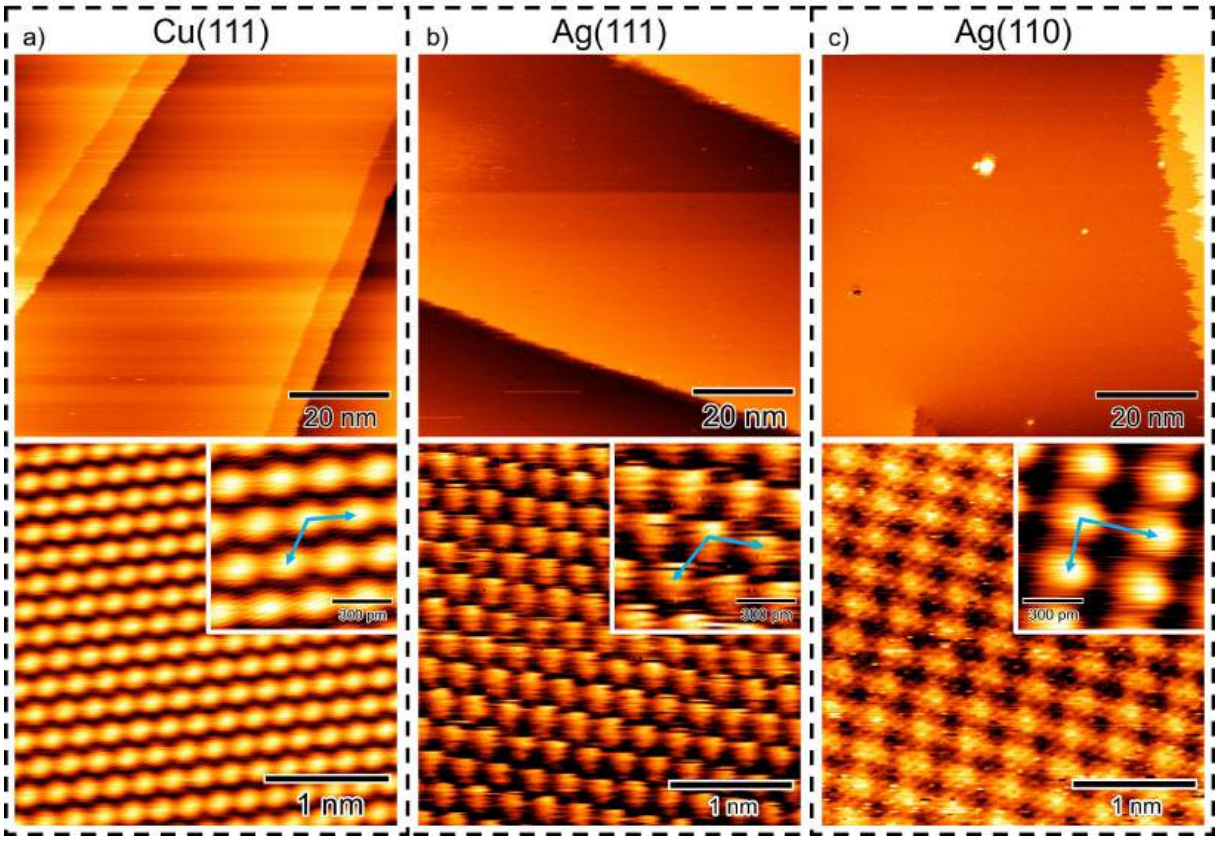

Figure 3.9: STM overview image of a) Cu(111), b) Ag(111), and c) Ag(110) substrates with respective high-resolution STM images showing the atomically resolved surface in the bottom images. The blue arrows represent the lattice vectors of the surface.

The Cu(111) substrate shown in Figure 3.9a was prepared using typical parameters of Ar^+ sputtering (800 eV; 10.0 μA cm^{-2}) for 30 minutes. The preparation chamber was backfilled with Ar at a partial pressure of 4x10^{-6} mbar. The annealing step was performed at 790 K for 15-20 minutes. The temperature was measured using a commercial infrared pyrometer. For the Ag(111) and Ag(110) surfaces, the sputtering was performed at similar Ar partial pressures as in the case of Cu(111) but with an ion energy of 600 eV (8.0 μA cm^{-2}) for 30 minutes. The annealing procedure was performed at 770 K for 10-15 minutes.

Metal and molecular deposition

The Co metal deposition used in this thesis was performed using a commercial e-beam evaporator Focus model EFM3. The metal consists of a Co rod (99.999%) 2-3 cm long. Inside the evaporator, the rod is placed near a tungsten filament and we applied a high-voltage at the metal. In such a configuration, the rod is bombarded with electrons and melts the apex of the material, releasing the metal atoms. The deposition is controlled by monitoring the flux of ionized atoms, the emission current, and the exposure time. Typically, for Co with a 1000 V applied an emission current of 6 mA is necessary to maintain a 3 nA flux By using these parameters for an exposure time of 30 seconds, we obtain coverages in the adatom regime

(≤ 0.05 ML). For our purposes, it is important to achieve such low coverage to investigate the role of the Co adatoms in the MOF formation.

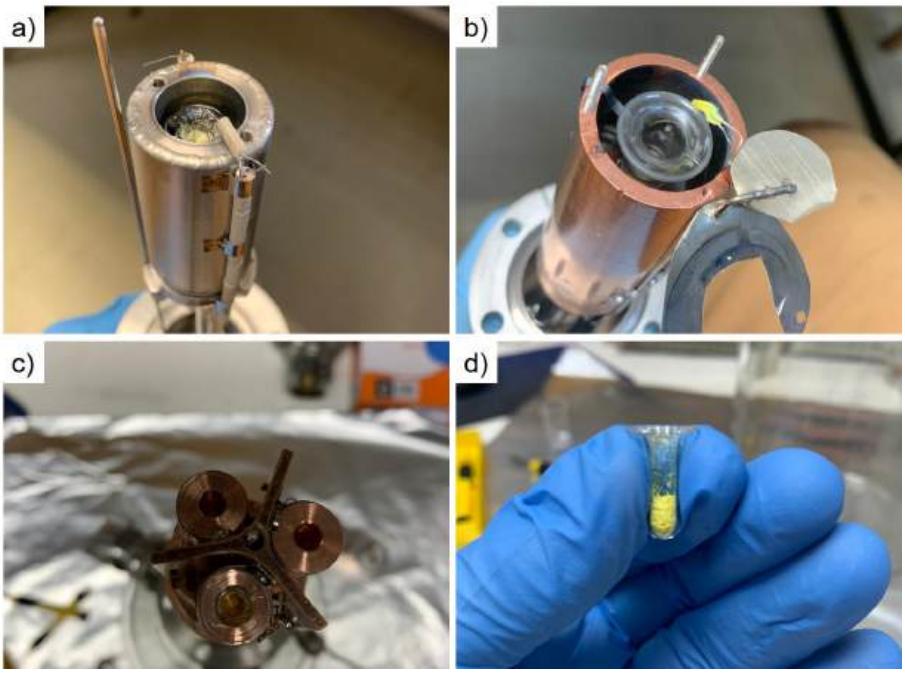

Figure 3.10: a-c) Knudsen cell evaporators for molecular deposition; d) Quartz crucible with molecular precursor inside (yellow powder).

All molecular precursors used in this thesis were sublimated using Knudsen cell evaporators, as shown in Figure 3.10a-c. We performed the depositions using three different evaporators with a single cell (see Figure 3.10a and b) and a three-fold cell (see Figure 3.10c). The molecular precursors used are all in solid state at RT (yellow powder in Figure 3.10d). They were placed in a quartz crucible which is then inserted in the Knudsen cell. The crucible is heated by a filament, sublimating the molecules. The crucial parameters for molecular evaporation are the filament current, the evaporation temperature, and the exposure time. The coverage calibration was performed by STM measurements, limiting to ≤ 1 ML for all experiments.

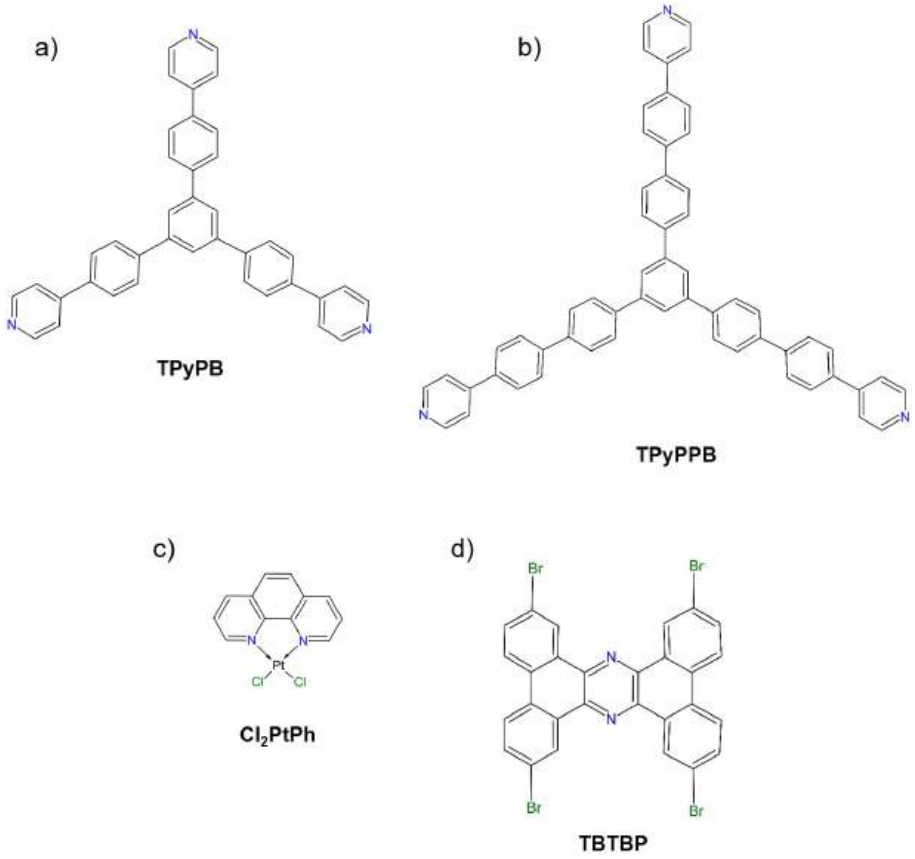

Figure 3.11: a) TPyPB, b) TPyPPB, c) Cl_2PhPt, and d) TBTBP molecular structures.

All molecules used in this thesis are shown in Figure 3.11a-d. The 1,3,5-tris[4-(pyridin)phenyl]benzene (TPyPB) and 1,3,5-tris[4-(pyridin)-[1,1'-biphenyl]benzene (TPyPPB) precursors shown in Figure-3.11a and b respectively, were purchased from ET Chem Extension. Both precursors present similar morphologies with pyridyl end groups, only differing in the arm length. Figure 3.11c display the dichloro-(1,10-phenanthrolin)-platin(II) (Cl_2PhPt) precursor, purchased from Sigma-Aldrich. The 2,7,11,16-tetrabromotetrabenzo [a,c,h,j] phenazine (TBTBP) molecule is shown in Figure 3.11d, and it is a non-commercial molecule. The precursor was synthesized by the group of Prof. Ronaldo Pilli from the Chemistry Institute (IQ) at UNICAMP following the reported procedure [117]. All evaporators were degassed for long periods ($\geq$ 3 hours) before deposition, guaranteeing no contamination on the surface. For all precursors, the deposition coverage was determined by STM measurements, maintaining the submonolayer coverages. This is an important step in synthesizing the nanostructures since the on-surface molecular diffusion is crucial for the quality of the material formed. The deposition temperatures for each precursor are summarized in Table 3.1. Depending on the evaporator used, these values may change due to the position of the thermocouple in the evaporator.

Table 3.1: Crucible temperatures during molecular deposition

Molecule	Temperature
TPyPB	570 K
TPyPPB	650 K
Cl_2PhPt	510 K
TBTBP	620 K

Chapter 4

Engineering Large Nanoporous Networks with Size and Shape Selected by Appropriate Precursors

---

Publication: **Alisson Ceccatto**, Eva Marie Freiberger, Natalie J. Waleska-Wellnhofer, Simon Jaekel, Duncan John Mowbray, Christian Papp, Hans-Peter Steinrück, Abner de Siervo. **"Engineering large nanoporous networks with size and shape selected by appropriate precursors"**. *Carbon* 221, 118945 (2024)

All DFT calculations presented in this chapter were performed using the Imbabura cluster at Yachay Tech University by Prof. Duncan John Mowbray.

Large domains of two-dimensional supramolecular porous nanostructures are interesting for various applications from electronics to biology. Here, we investigate the formation of Cu-coordinated networks on Cu(111) using scanning tunneling microscopy and density functional theory (DFT). We consider two molecules with three pyridyl end groups connected to a central benzene ring by either one or two phenyl groups, namely 1,3,5- tris[4-(pyridin)phenyl] benzene (TPyPB) and 1,3,5-tris[4-(pyridin)-[1,1'-biphenyl] benzene (TPyPPB), respectively. Upon deposition of TPyPB at room temperature, a honeycomb nanostructure forms, which is stabilized by Cu adatoms, as previously seen. Upon deposition at 400 K, the growth dynamics change, and molecules become trapped in the hexagonal pores. In contrast, deposition of TPyPPB at room temperature leads to vitreous structures, which rearrange at 400 K forming a low-defect and extended ordered honeycomb phase, which is also stabilized only in the presence of Cu adatoms. The DFT calculations for both honeycomb phases show an impressive agreement with the experimental results, considering the size of such structures. After annealing at 420 K, a complex flower-like structure composed of a mix of two- and three-fold coordinated Cu centers emerges. Further annealing to above 420 K leads to another new phase composed of a high molecular density motif, the so-called diamond phase.

Introduction

On-surface synthesis has emerged in areas ranging from electronics [118] to biology [119] as a tool to build two-dimensional (2D) materials by confining building blocks, e.g., on a metal surface. This acts as a template to construct functional nanostructures [120]. The on-surface reaction method enables unique architectures inaccessible via other preparation routes [85, 121]. For example, the synthesis of atomically precise graphene nanoribbons (GNRs) is only possible by bottom-up fabrication methods [62, 64]. This synthesis approach to form 2D nanostructures on metal surfaces has been widely explored due to their potential applications in gas storage, heterogeneous catalysis, and nanoelectronics [122–127]. A bottom-up strategy permits the exploration of different building blocks with programmable substituents, which can give rise to a tailored functionalization of the final structure [96, 128]. Furthermore, the functional end-groups (nitrogenated, carboxylated, halogenated, etc.) and their positions play a key role in on-surface reactions, controlling the molecule-molecule bonds and the geometry of the final products. Prominent examples of on-surface synthesis are coupling reactions employing halogenated precursor molecules such as the Ullmann [91] or Sonogashira reaction [129]. Such reactions enable the coupling of basic and also rather complex building blocks. In the Ullmann reaction, the halogen group dissociates, yielding free carbon radicals at the molecule's linkage sites, resulting in either organometallic or organic C–C bonded nanostructures [89, 102]. Similarly, the Sonogashira cross-coupling reaction also uses halogen functional groups. However, in this case, they are bonded to alkyne-

functionalized molecules [129,130]. For non-halogenated precursors, the network formation is typically stabilized by hydrogen bonds [131] or metal coordination [132]. This study uses the latter route to prepare 2D metal-organic frameworks (2D-MOFs).

In particular, on-surface coordination chemistry has proven remarkably efficient at forming nanostructures with extended domains by using cyano, pyridyl, or carboxyl end groups [31,43,133]. Due to the flexibility of their d-orbitals, metal adatoms can coordinate in different symmetries and bond lengths, directly affecting the MOF's structure and thereby its electronic properties [33, 134, 135]. Moreover, molecular pores can act as barriers that confine surface state electrons [136] or as a host for atoms/molecules working as nanoreactors in the so-called "host-guest" chemistry [126, 127, 137, 138]. Interestingly, the coordinating metal atoms can work as transmission channels for electrons between adjacent pores due to the weak potential barrier for the surface electrons, thereby forming coupled electronic states [139]. Moreover, the metal centers in MOFs are good platforms that can be explored as single-atom catalysts (SAC) by using different *d* metals as coordination centers, such as Cu, Ni, Pd, and Pt [140]. The surface analogous for MOFs, the so-called surface metal-organic networks (SMONs or 2D-MOFs), are model systems for a better understanding of physical and chemical mechanisms involved in the host-guest chemistry that are accessible by local-probe techniques such as STM.

The adsorption of 1,3,5-tris[4-(pyridin)phenyl]benzene (TPyPB, also denoted as ext-TPyB in literature [141]), a molecule with three pyridyl end groups connected to a central benzene ring by a phenyl group (see Figure 4.1b) on Cu(111), has been previously studied, and coverage-dependent molecular arrangements have been reported [141]. At low densities, semi-regular networks are formed via the coordination of the pyridyl (Py) end groups to Cu adatoms, leading to two- and three-fold Cu-coordinated metal-organic frameworks (MOFs). The resulting semi-regular tilings are a set of Euclidean tessellations made from two or more polygon faces [142]. By increasing the molecular density, the self-assembly results in different motifs such as honeycomb, square, and non-Archimedean lattices. Furthermore, the lattices can be tailored by choosing different metal atoms [29]. Notably, 1,3,5-tris(pyridyl)benzene (TPyB), that is the smaller analog of TPyPB with no phenyl spacer (see Figure 4.1a), assembles in different honeycomb patches coordinated either by Fe or Cu on Au(111), when both metals are coadsorbed on the surface [29, 143]. In the resulting structures, Cu is two-fold coordinated, whereas Fe is three-fold coordinated. Simultaneous deposition of both metals reveals that Cu coordination is more stable at room temperature (RT). Upon annealing at higher temperatures (400–500 K), the arrangement becomes coordinated by Fe centers, indicating kinetic and thermodynamic selection of the final products. Overall, the coordination chemistry of 2D-MOFs is a powerful strategy to control the morphology, electronic, and magnetic properties of such 2D nanoporous materials. However, similar studies of TPyPB's larger analog, 1,3,5-tris[4-(pyridin)-[1,1'-biphenyl]benzene (TPyPPB), with two phenyl groups connecting the three pyridyl end groups to the central benzene ring

(see Figure 4.1c), are missing in literature. A systematic investigation involving this large molecule is interesting, since the arm size defines the distance between the coordination centers and their oxidation state due to the different number of coordinations. Moreover, the molecular size also leads to a different concentration of metal centers, possibly affecting the catalytic behavior of the organic overlayer.

Herein, we combine scanning tunneling microscopy (STM) and density functional theory (DFT) to investigate the self-assembly of two different three-legged organic molecules, TPyPB and TPyPPB, on Cu(111). They are both functionalized with pyridyl end groups but exhibit different arm lengths, that is, one or two phenyl spacers between the central benzene ring and the end group, as shown in Figure 4.1b and 4.1c, respectively. Table 4.1 in the Supplementary results shows the different arm lengths for TPyB, TPyPB, and TPyPPB precursors. Such differences allow for the control of the pore size and the distance between Cu adatoms. After deposition at RT, TPyPB coordinates with Cu adatoms in large domains ($\geq$ 100 nm) of a honeycomb nanostructure. On the other hand, the adsorption of TPyPPB at RT forms vitreous-like arrangements of Cu-coordinated molecules. Annealing up to 350–500 K leads to many different final structures depending on temperature and duration. After heating to 400 K, we find a coexistence of honeycomb networks and flower-like nanostructures. The honeycomb domains are characterized by two-fold Cu coordination, whereas the flower-like patches are more complex with two- and three-fold coordination centers in the unit cell. Based on our DFT calculations, we also shed light on the process of Cu–Py coordination and the chemical stability of the porous nanostructures.

Results and discussion

TPyPB on Cu(111)

As a first step, we revisit the adsorption behavior of the three-legged molecules with one phenyl spacer, TPyPB, shown in Figure 4.1b and previously studied by Lin et al. [141,144,145]. These results serve as a basis for our study of the larger molecules with two phenyl spacers, TPyPPB, shown in Figure 4.1c. In addition, our DFT calculations provide new information on the nature of the metal-coordination bonds.

Depositing submonolayer coverages of TPyPB at RT leads to three main arrangements, as shown in the STM measurements in Figure 4.2a-c, in agreement with Ref. [141]. All arrangements form ordered patches with distinct symmetries, as shown by the FFT images in Figure 4.9 in the Supplementary results. The honeycomb structure in Figure 4.2a and the semi-regular nanostructure in Figure 4.2b are stabilized via intermolecular Py-Cu-Py bonds. This is due to both the repulsive interaction between the N end groups and copper's propensity for forming Cu–N bonds. The semi-regular nanostructure exhibits a hexagonal unit cell as highlighted in green in Figure 4.2b. For the honeycomb structures, the metal

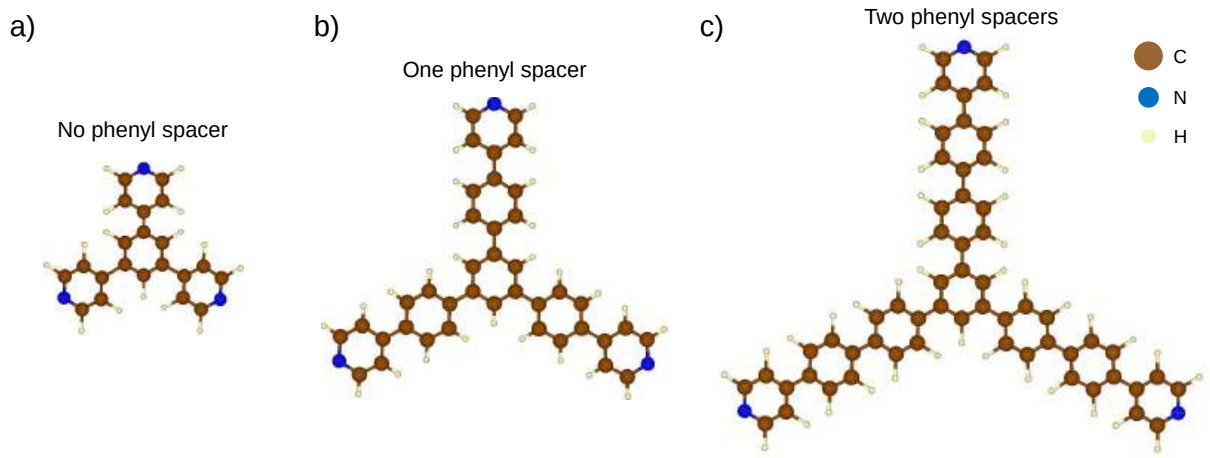

Figure 4.1: Molecular precursor structures for a) TPyB, with no phenyl spacer, b) TPyPB, with one phenyl spacer, and c) TPyPPB, with two phenyl spacers. C, N, and H atoms are depicted in brown, blue, and light yellow, respectively.

center is two-fold coordinated, and for the semi-regular phase, the Cu centers are both two- and three-fold coordinated, as reported by Yan et al. [141]. The third structure in Figure 4.2c has a square-like motif, with more complex interactions between the molecules. It is characterized by an outer octagon and an inner square, as highlighted in green and blue in Figure 4.2c. The inner squares are formed by two-fold Cu coordination and the outer octagons exhibit two types of interaction: six sides interact via two-fold Py-Cu-Py coordination (green sides) while the other two are stabilized by hydrogen bonds (blue sides), N···H, between the N end groups and the H in the molecular arms (see the blue oval in Figure 4.2c). This arrangement is similar to the one reported by Yan et al. [141] for TPyPB on Cu(111) with a molecular density of 0.195 mol nm^{-2}.

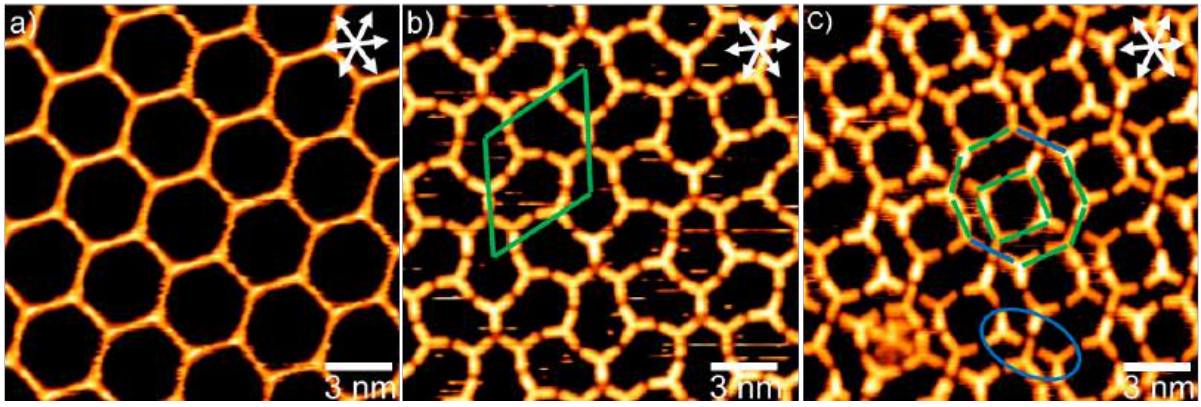

Figure 4.2: STM images of TPyPB deposited on Cu(111) at RT yelding either a) a honeycomb ($I_t = -650$ pA; $V_t = -1.4$ V), b) a semi-regular ($I_t = -610$ pA; $V_t = -1.4$ V), and c) a square motif ($I_t = -700$ pA; $V_t = -1.4$ V). The white arrows indicate the main crystallographic directions of the Cu(111) surface.

The predominant phase among these three phases with distinct symmetries is the honeycomb structure, which forms extended domains. The molecules are coordinated via collinear head-on Py-Cu-Py interactions of the linker groups of the neighboring mo-

lecules, as seen from the high-resolution STM image in Figure 4.3a and the DFT simulation in Figure 4.3b.

To better understand the nature of these interactions we have performed DFT calculations for a honeycomb network of TPyPB on Cu(111) without and with Cu adatoms, aligning the molecules along either the long-bridge $\langle 1\bar{2}0\rangle$ direction or rotated by 19° in the $\langle 210\rangle$ direction, as is the case experimentally (see Figure 4.3a). Without Cu adatoms, we find the TPyPB honeycomb lattice aligned in the $\langle 210\rangle$ direction (see Figure 4.3c) is almost isoenergetic with isolated TPyPB molecules adsorbed on Cu(111), i.e., $E_{form} \approx 0$ eV/mol. However, in this case, it is possible to form the network without Cu atoms given that the adsorbate in-plane compression is sufficiently high [141]. In contrast, when aligned along the $\langle \bar{1}20\rangle$ direction, we find the TPyPB honeycomb lattice becomes unstable ($E_{form} \approx -0.27$ eV/mol). This indicates the TPyPB overlayer prefers a molecular alignment in the $\langle 210\rangle$ direction, as we see experimentally. When Cu adatoms are introduced at the TPyPB junctions, we find organometallic Py-Cu-Py bonds are formed and for each molecular alignment the honeycomb structure becomes quite stable ($E_{form} > 1.5$ eV/mol) and is reasonably close to the Cu(111) surface, with an adsorption height of $d \approx 2.8$ Å. In particular, placing the Cu adatoms on bridge sites and aligning the TPyPBs in the $\langle 210\rangle$ direction yield the most stable structure ($E_{form} = 1.77$ eV/mol) by more than 0.2 eV, in agreement with our experiments (see Figure 4.3). It is worth noting that the inclusion of Cu adatoms within the overlayer is justified by both their known availability and mobility at RT.

For TPyPB on Cu(111) the insertion of Cu adatoms leads to a head-to-head configuration as shown in Figure 4.3b, which agrees with the experimental results shown in Figure 4.3a. For the scenario without the Cu adatoms, the STM simulations show that the molecules are not coordinated via head-on interactions, as highlighted in green in Figure 4.10 in the Supplementary results. By comparing the STM image and the simulation for the coordination via Cu adatoms in Figure 4.3, it is observed that in both cases the Cu adatoms are quite difficult to resolve. This is in line with previous studies on coordinated nanostructures with nitrogen functional groups due to the weak electronic density of the metal centers after the coordination [141, 146, 147].

From the STM images we determine the lattice vectors of the porous honeycomb network to be $|\vec{\mathbf{a}_1}| = |\vec{\mathbf{a}_2}| = (3.9 \pm 0.1)$ nm, with an angle of 60±2°, resulting in a pore size of ~13 nm^2 and a molecular density of 0.15 TPyPB/nm^2. For our DFT calculations of the honeycomb network we employed a unit cell with a lattice parameter of ≈ 4.05 nm rotated by 19.1° from the $\langle \bar{1}10\rangle$ direction. This angle is in excellent agreement with our experimental observations from STM, which yield an angle of 20±2°. This is evident from Figure 4.11 in the Supplementary results, in which two rotational domains, highlighted by dark-blue and green areas, are displayed. The two domains are rotated by 20° with respect to the $\langle \bar{1}10\rangle$ directions (see white arrows in the upper right corner) and by 40° with respect to each other. The main crystallographic substrate directions were determined using an STM image of the Cu(111)

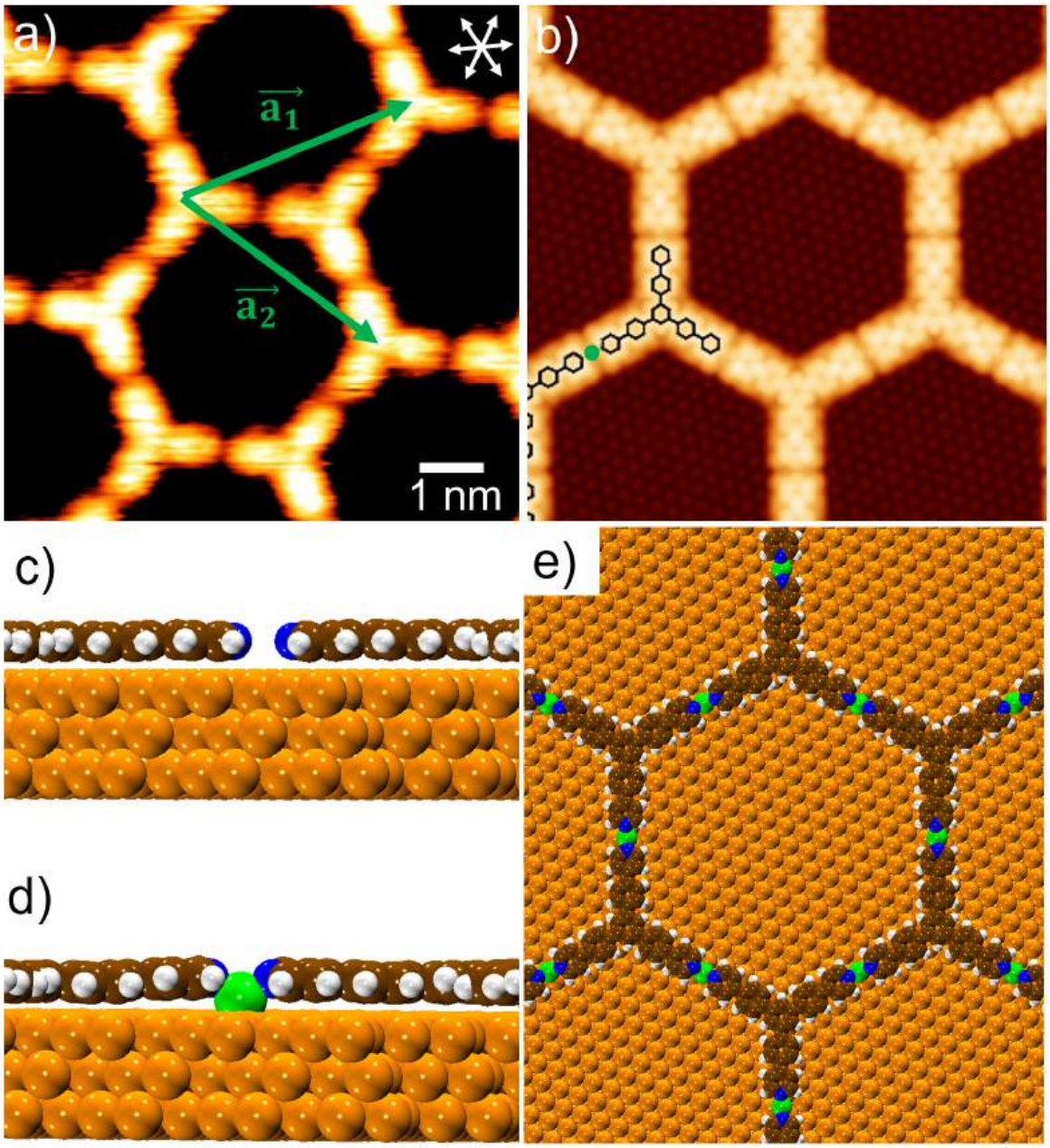

Figure 4.3: a) High-resolution STM image of the honeycomb arrangement of TPyPB with the lattice vectors $\vec{\mathbf{a}}_1$ and $\vec{\mathbf{a}}_2$ ($I_t = -710$ pA; $V_t = -1.4$ V). b) STM simulation of the honeycomb nanostructure stabilized by Cu adatoms, highlighted by the green dot. DFT relaxed structures for c) Py–Py and d,e) Py–Cu–Py linkages. The Cu adatoms are highlighted in green.

surface with atomic resolution.

Deposition of the TPyPB molecules at high temperatures changes the growth dynamics of the metal-organic layer. Adsorption at 400 K leads to large honeycomb domains without the existence of semi-regular or square-like arrangements, as evident from Figure 4.4a and b. Since the honeycomb nanostructure grows large domains at higher temperatures as compared to RT [141], the formation of the hexagonal pores occurs immediately upon deposition of the molecules on the surface. Some molecules adsorb on the metal-

organic layer as the deposition continues and populates the pores. This behavior is not reported for deposition at RT and subsequent annealing, suggesting that the pore population is related to the growth sequence of the sample [141, 144]. However, these figures show that there are dark and bright cavities, suggesting a population of the pores. We can attribute this irregular appearance of the pores to two scenarios: a) mobile TPyPB molecules and/or b) new molecular species formed from the TPyPB precursor. The green arrows in Figure 4.4b highlight pores with an irregular appearance. Such behavior can be attributed to mobile species in the pores during the time scale of the STM scan. Two-dimensional nanoporous networks have a great potential to act as nanoreactors, by confining the chemical reactions in regions of a few nanometers [126, 127]. In such confined regions, the surface state electrons are scattered due to the confinement, giving new catalytic properties in the pores compared to the clean substrate. It is possible that the change in the electronic density of states in the pores combined with the substrate temperature during deposition (400 K), catalyzed the intramolecular reaction, e.g. cleaving off molecular arms and rearranging into new molecular species. However, further experiments are needed to address such behavior, which is beyond the scope of this work.

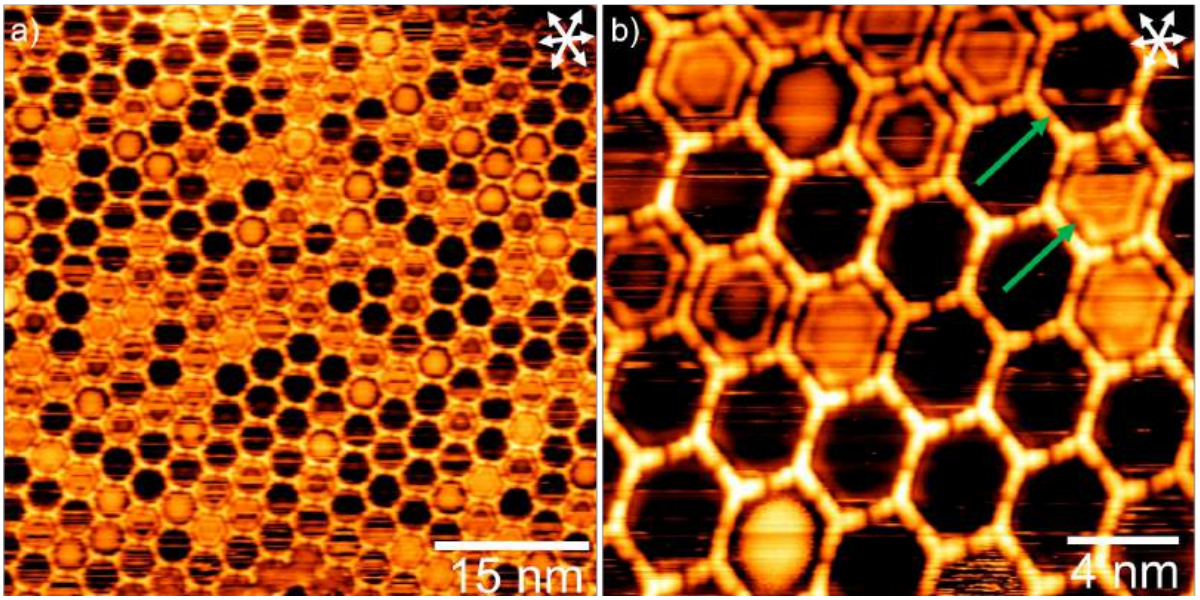

Figure 4.4: a) Overview image after molecular deposition of TPyPB with the substrate held at 400 K during the sublimation (I_t = -580 pA; V_t = -1.4 V); b) Zoom image of hexagonal networks with distinct apparent heights related to trapped molecules in the pores (I_t = -520 pA; V_t = -1.4 V).

For high molecular coverages of TPyPB, the growth behavior is quite different, with the molecules forming a densely packed assembly with a molecular density of ≈ 0.30 mol/nm^2, as shown by Figure 4.12a in the Supplementary results. Two bonding motifs are observed: two of the arms are Cu-coordinated with other molecules while the third arm is stabilized by the N···H bonds between the pyridyl end group and the phenyl group of an adjacent molecule, as highlighted by the blue oval in Figure 4.12b in the Supplementary results. This contrasts with the situation on Ag(111), where TPyPB grows a close-packed nanostruc-

ture stabilized by N···H bonds between the terminal pyridyl groups and the central benzene of the adjacent molecule [30]. The main difference regarding the molecular self-assembly on Cu(111) and Ag(111) is that Ag adatoms do not coordinate with the pyridyl end groups [30]. The non-coordination chemistry with Ag adatoms for precursors functionalized with pyridyl and cyano-groups has been extensively reported in the literature [36, 148–150].

TPyPPB on Cu(111)

As a next step, we investigated an unexplored molecule with two phenyl spacers, TPyPPB, shown in Figure 4.1c. The additional phenyl unit incorporated in the molecular arms leads to substantial changes in the molecular arrangements. We investigated several coverages, from the submonolayer range up to the fully saturated layer. In each case, the denoted coverage was obtained from the surface area covered by the metal-organic layer networks as estimated from several STM images. Table 4.2 in the Supplementary results summarizes the resulting coverages and sublimation parameters.

Deposition of TPyPPB on Cu(111) held at RT with a coverage of ≈ 50%, leads to a vitreous-like phase shown in Figure 4.5a, with different coordination motifs. This is in contrast to the adsorption of TPyPB under the same conditions, which reveals more ordered arrangements with three main motifs: honeycomb, semi-regular, and square. The difference in the length of the molecular arms for TPyPPB and TPyPB (see Table 4.1 in the Supplementary results) leads to such distinct behavior. Since the Cu adatoms tend to adsorb in specific sites on the surface, the Py-Cu-Py intermolecular interactions are limited by the length of the molecular arms and the adatom position. The vitreous-like nanostructure is similar to the atomic arrangement of silica and hence denoted as vitreous [151]. To increase the molecular diffusion on the surface, the sample was heated to 350 and 380 K for 5 minutes each. After annealing at 350 K, the molecules start to form honeycomb-like motifs that grow into larger domains at 380 K as shown in Figure 4.5b. These honeycomb patches do not fully cover the surface (surface coverage of only ≈50%) but grow in isolated domains of around 50-70 nm in diameter. At 380 K, the molecules start to form a flower-like nanostructure that displays a unique geometry as shown in Figure 4.5c.

This configuration is a complex nanostructure composed of a central hexagon surrounded by six smaller elongated hexagons, as shown by the high-resolution STM image in Figure 4.5d. The structure resembles an Archimedean lattice called bounce [152]. As known from theoretical calculations, such Archimedean lattices exhibit remarkable electronic properties, e.g., topological band gaps and flat bands [40]. This configuration has already been predicted by Monte Carlo calculations and also reported experimentally for the small analog with no phenyl spacer, TPyB, coordinated by Cu adatoms on Au(111) [153, 154]. The calculations reveal similar energies for two- and three-fold coordination, which results in different coexisting geometries for the metal-organic layer [153]. Interestingly, while a

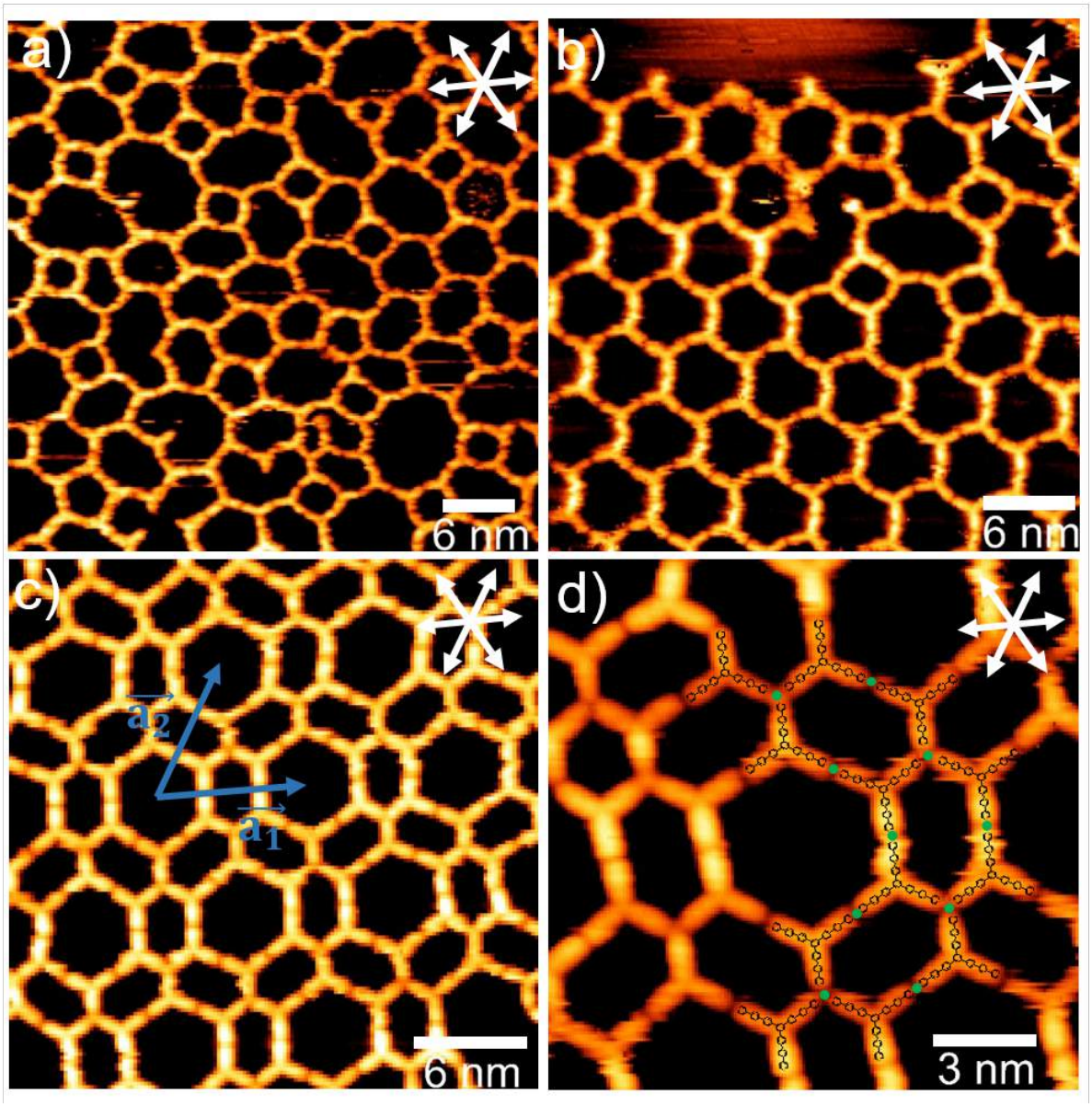

Figure 4.5: a) Vitreous-like arrangement after RT deposition (I_t = -270 pA; V_t = -1.6 V). b) Honeycomb nanostructure after annealing at 350 K for 5 minutes (I_t = -300 pA; V_t = -1.8 V). c) Metal-organic lattice of flowers defined by $\vec{\mathbf{a}_1}$ and $\vec{\mathbf{a}_2}$ (I_t = -320 pA; V_t = -1.6 V). d) High-resolution STM image of the flower-like nanostructure with the superimposed molecular structures coordinated by Cu adatoms in green (I_t = -320 pA; V_t = -1.6 V).

similar coordination with the pyridyl group is predicted by theory on Ag(111), it is not observed experimentally [30].

For Cu coordination, the metal-organic layer is thus characterized by the coexistence of two- and three-fold coordination, depending on molecular coverage and temperature. Indeed, the flowers have two types of coordination centers: the inner hexagon sides are formed by two-fold coordinated Cu adatoms, as shown in the high-resolution STM image of Figure 4.5d, while the elongated hexagonal pores are interconnected to each other via three-fold coordination centers. We attribute the appearance of such complex structures to the similar interaction energies of two- and three-fold Cu adatoms as found by Monte Carlo

calculations [153]. Figure 4.5c shows an ordered motif of the flower-like arrangement with the lattice parameters $\vec{\mathbf{a}_1}$ and $\vec{\mathbf{a}_2}$ being highlighted. The lattice angle is 60±2° with the lattice vector $\vec{\mathbf{a}_1}$ aligned with the $< \bar{1}10 >$ surface direction. The superstructure is commensurate (33×33) with lattice constants $|\vec{\mathbf{a}_1}| = |\vec{\mathbf{a}_2}| = (8.4 \pm 0.1)$ nm, suggesting a Cu–N bond length of (2.5 ± 0.5) Å. This value agrees with the typical values for Cu–N bonds [155, 156].

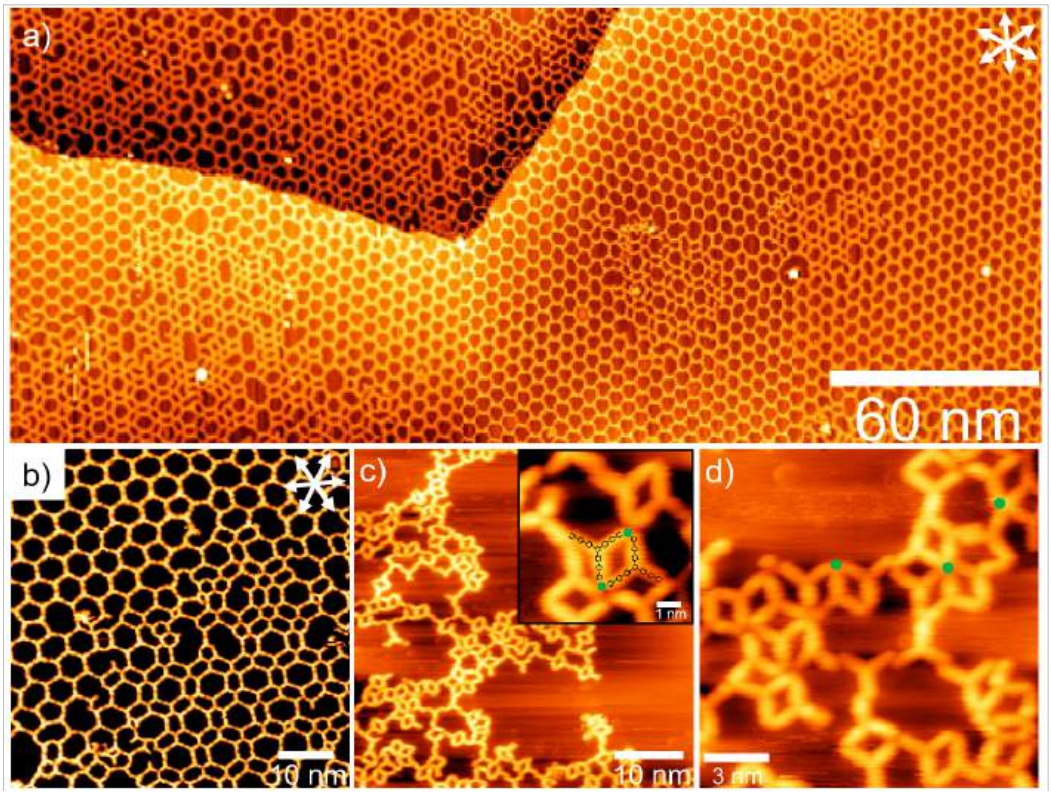

Figure 4.6: a) Overview of the saturated layer of TPyPPB molecules forming two main distinct motifs after annealing at 400 K for 5 minutes. STM images after further annealing at b) 420 K and c) 500 K for 5 minutes. The zoom image in the inset shows the diamond domain coordinated by Cu adatoms in green. d) STM image showing the different coordination centers (three-, four-, and five-fold) highlighted by the green dots. a) (I_t = -330 pA; V_t = -1.8 V). b) (I_t = -330 pA; V_t = -1.6 V). c) (I_t = -290 pA; V_t = -1.8 V). d) (I_t = -230 pA; V_t = -1.1 V).

Figure 4.6a provides a large area STM image of a surface fully covered with a TPyPPB layer (see evaporation parameters in Table 4.2 in the Supplementary results), obtained after annealing at 400 K for 5 minutes. This coverage leads to domains of two main phases: the flower-like and honeycomb structures. Notably, the boundaries between the phases are characterized by a transition region, where the molecules form pores with different geometries. Further annealing at 420, 450, and 500 K was performed for 5 minutes in each step. The corresponding representative STM images for 420 and 500 K are shown in Figure 4.6b and 4.6c, respectively. The STM image in Figure 4.6b, after heating to 420 K shows no distinct changes regarding the coverage and structural arrangement of the molecules. Substantial changes only begin when the sample is heated to 450 K with a new phase emerging, the so-called diamond phase, that covers the surface at 500 K, as shown in Figure 4.6c. Its molecular structure is shown in the inset in Figure 4.6c. After annealing at 500 K, the STM

images in Figure 4.6c and 4.6d show that the majority of molecules are arranged in diamond-shaped motifs. In this configuration, molecules form dimers with the metal center in various coordination symmetries, that is, three-, four-, and five-fold coordinated, highlighted by green dots in Figure 4.6d.

The histogram in Figure 4.7a shows the statistical analysis of several STM images as a function of the annealing temperature. We display the fractions of four different structural motifs on the surface, the honeycomb, flower-, diamond-, and vitreous-like structures. Besides the formation of the diamond phase upon annealing at 450 and 500 K, we observe the emergence of uncovered regions in the STM images, labeled as the free area in the histograms. While the honeycomb and flower-like phases have similar densities (0.08 TPyPPB/nm^2 and 0.10 TPyPPB/nm^2, respectively), the diamond phase is a more densely packed structure (0.14 TPyPPB/nm^2), which is by ≈43% and ≈29% denser than the honeycomb and the flower-like patches, respectively. The molecular density of the diamond phase was estimated using the smaller structure formed, shown in the zoomed inset of Figure 4.6c (see Figure 4.7e also). For this reason, we attribute the emergence of uncovered regions to the rearrangement of less densely packed honeycomb or flower-like phases to the more densely packed diamond phase and not to molecular desorption.

To investigate the behavior of the metal-organic layer as a function of annealing time, we heated the sample at 400 K for 5, 15, and 120 minutes. The histogram in Figure 4.7b shows the statistical distribution of the different phases as a function of time. Overall, the fraction of the vitreous phases decreases with time, while simultaneously the fractions of the ordered honeycomb phase (model in Figure 4.7c) and flower-like phase (model in Figure 4.7d) increase. The fraction of the honeycomb phase is by about a factor of 2 to 2.5 times larger than that of the flower-like phase, which suggests that this is the most stable structure. The conversion into the honeycomb structure is limited by molecular diffusion and free space to form the nanostructure. At 400 K, the honeycomb domains grow larger for the coverage of 90% than for the fully covered sample (see Table 4.2 in the Supplementary results) and are almost defect-free as displayed in Figure 4.13 in the Supplementary results. After comparing the behavior for different coverages (see Table 4.2 in the Supplementary results), the coverage of 90% turned out to be the optimum condition to obtain a homogeneously covered surface. After annealing at 400 K for 3 hours, the molecules grow in large domains (> 125 nm), as shown in Figure 4.8a and Figure 4.14 in the Supplementary results. This clearly shows that it is necessary to keep a small area of the surface uncovered to allow for molecular diffusion and rearrangement. Remarkably, for TPyPPB with two phenyl spacers, the semi-regular and square-like motifs found for TPyPB with only one phenyl spacer in Figure 4.2b and 4.2c were not observed in any experiment.

Figures 4.8b and 4.8c display two honeycomb domains each rotated by 7±1° from the $<\bar{1}10>$ direction of the Cu(111) surface, yielding an angle of 14±2° between the domains. The length of the lattice vectors of the two domains agrees with the experimental uncer-

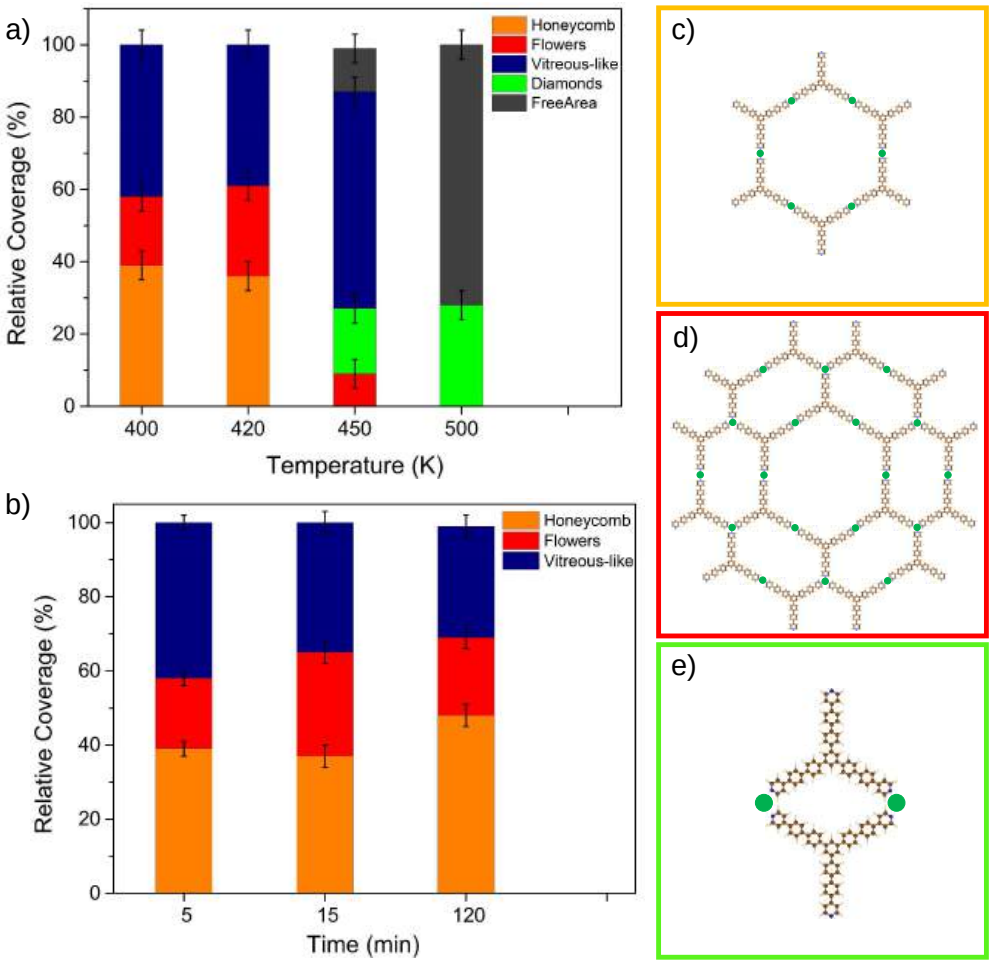

Figure 4.7: Histograms of the molecular arrangements for the sample with saturated layer as a function of annealing a) temperature in K, and b) duration in minutes at 400 K. Structural models for the c) honeycomb, d) flower-like, and e) diamond-shaped motifs (C in brown, N in blue, H in light yellow, and Cu in green).

tainties. For the first domain, shown in Figure 4.8b, the lattice constants are $|\vec{\mathbf{a}_1}| = |\vec{\mathbf{a}_2}| = (5.2 \pm 0.2)$ nm with a lattice angle of $60 \pm 1°$. For the second domain, shown in Figure 4.8c, the lattice constants equal $|\vec{\mathbf{a}_1}| = |\vec{\mathbf{a}_2}| = (5.3 \pm 0.2)$ nm with a lattice angle of $59 \pm 1°$. The honeycomb structure formed from TPyPPB has a large pore size with a hexagon side length of 3.0 ± 0.1 nm and a pore area of ≈ 24 nm^2 (see Table 4.1 in the Supplementary results). Despite the distortion, this structure is very similar in shape to the honeycomb structure of the smaller TPyPB molecule coordinated with Cu atoms on a Cu(111) with a smaller pore area of 13 nm^2 [141]. The hexagons forming the TPyPPB honeycomb lattice are composed of a 1:1 ratio of molecules and Cu adatoms, as is evident from the high-resolution STM image in Figure 4.8d.

To see how the Py-Cu-Py interaction for TPyPPB compares with that of TPyPB, we have also performed DFT calculations for a TPyPPB honeycomb network on Cu(111) without and with Cu adatoms and aligning the molecules along either the long-bridge $\langle\bar{1}20\rangle$ direction or rotating them by about $\pm 7°$, as found in our STM measurements. For both alignments, the TPyPPB honeycomb network without Cu adatoms is very unstable ($E_{form} > 0.55$ eV/mol)

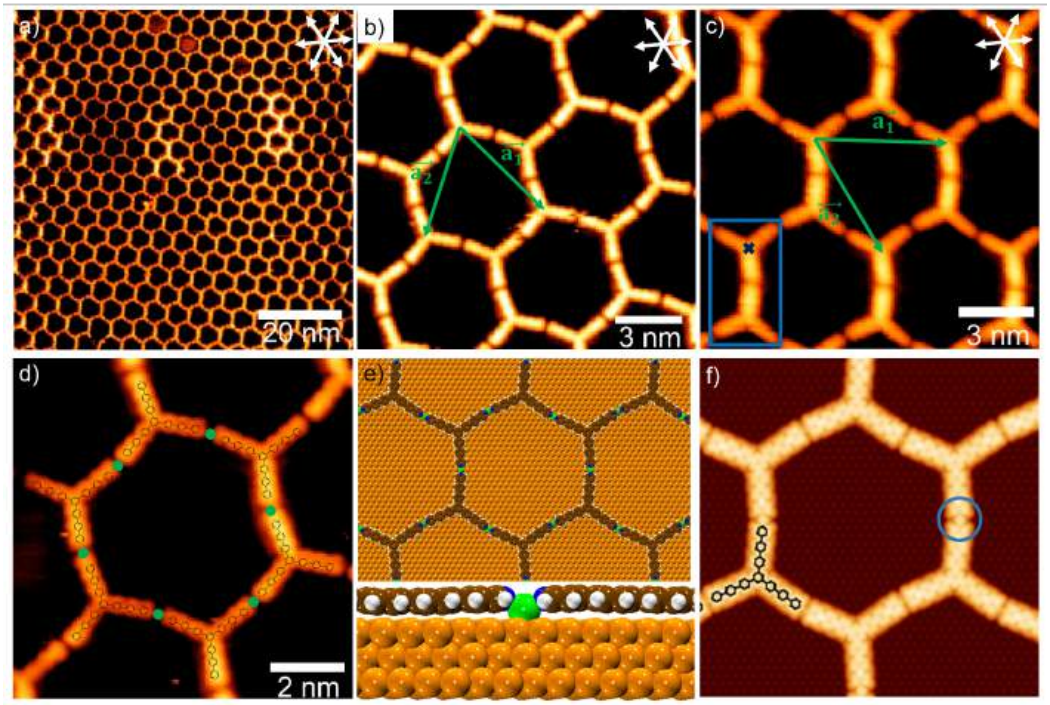

Figure 4.8: a) Extended domain of the honeycomb nanostructure formed after annealing the sample with a surface coverage of 90% at 400 K for three hours. b,c) Rotational domains of the honeycomb nanostructure highlighting the lattice vectors $\vec{\mathbf{a}_1}$ and $\vec{\mathbf{a}_2}$. The hexagons of the domains show distortions as highlighted by the blue rectangle in c). d) High-resolution STM of the hexagonal pores with superimposed TPyPPB molecular structure coordinated by Cu adatoms in green. e) Top- and side-view for the honeycomb nanostructure formed after Cu-coordination obtained from DFT (Cu adatoms in green). f) STM simulation for the honeycomb nanostructure stabilized by coordination with Cu adatoms, highlighting the adatoms at atop positions with a blue circle. a) (I_t = -280 pA; V_t = -0.8 V). b) (I_t = -240 pA; V_t = -0.5 V). c) (I_t = -260 pA; V_t = -1.9 V). d) (I_t = -240 pA; V_t = -0.5 V).

and should not be experimentally observable. However, when Cu adatoms are introduced at the TPyPPB junctions, Py-Cu-Py organometallic bonds are formed yielding quite stable structures (E_{form} ~ 1.50 eV/mol) as was the case for TPyPB. This suggests that Cu adatoms are indispensable when forming a TPyPPB network. Note that, in contrast to the experimental results, the ±7° rotation of the TPyPPB molecules (see Figure 4.8e) slightly destabilizes the overlayer by about 0.1 eV/mol. This discrepancy is most probably attributable to the higher inherent entropy of this rotated structure, which should lead to stabilization at higher temperatures but is neglected in our DFT-calculated formation energies. Perhaps more importantly, the resulting STM simulation based on this structure (see Figure 4.8f) is in striking agreement with the high-resolution STM measurement of the hexagonal pores (see Figure 4.8d).

Notably, the molecules stabilize in a honeycomb lattice composed of distorted hexagons highlighted by a blue rectangle in Figure 4.8c, where the molecules are rotated around the central benzene ring of TPyPPB, which is indicated as dark blue cross. Our calculations also considered this behavior, as shown in Figures 4.8e and f. In both theory and experiment the molecules are rotated by ≈7° around the central benzene ring, and the Cu adatoms are located either at the bridge or atop adsorption sites. Interestingly, the STM sim-

ulation shows that it is possible to visualize the Cu adatoms in the atop positions, as highlighted in blue in Figure 4.8f. The observed behavior suggests that the molecules optimize their positions to achieve the best coordination with the Cu adatoms on the surface since the most stable configuration is the honeycomb nanostructure. Interestingly, an even more pronounced distortion of some pores can occur, as highlighted by the green oval in the STM image of Figure 4.15a in the Supplementary results. Here, pores are distorted in two manners: one is elongated along $\vec{\mathbf{a}}_2$ direction and consequently, the adjacent one is compressed in the same direction, as illustrated in Figure 4.15b in the Supplementary results.

It is worth mentioning that for three- and four-fold Cu-coordination, which can occur rarely and for non-perfect structures, it is possible to resolve a bright circular protrusion at the molecular junctions as highlighted by the green arrows in Figure 4.16a and b in the Supplementary results. This contrasts the situation for two-fold coordination, where no such protrusion due to the Cu adatoms is resolved, as indicated by the blue arrow in Figure 4.16b in the Supplementary results. We might attribute this behavior to electronic effects induced by a Cu adatom in a different oxidation state (or coordination state) due to interaction with more than two molecules. An alternative explanation is that the metal in three- or four-fold coordination has a larger distance to the surface than in the two-fold coordination, causing brighter spots in the STM images. The latter explanation is in line with the STM simulations of Figure 4.8f since we can visualize the Cu adatoms located in atop positions.

Conclusion

In summary, we present a detailed study of the synthesis and characterization of highly ordered metal-organic layers for two similar three-legged molecules on Cu(111) using STM and DFT. The two molecules have three functional pyridyl linkers separated from a central benzene ring by either one or two phenyl spacers. For the precursor molecule with one phenyl spacer (TPyPB), we obtain a honeycomb nanostructure in line with previous investigations. Our DFT calculations demonstrate that this structure is stable only in the presence of two-fold coordinated Cu adatoms. Moreover, increasing the substrate temperature to 400 K during the molecular deposition affects the growth dynamics resulting in a honeycomb layer with trapped TPyPB molecules in the cavities. Depositing the molecules at RT leads to two further nanostructures with square-like and semi-regular motifs in line with previous investigations.

For TPyPPB, an unexplored precursor with two phenyl spacers, quite different behavior is observed. This is characterized by various phases depending on the annealing temperature. At 400 K, the molecules grow in large domains (>100 nm in diameter) of Cu-coordinated honeycomb motifs. This structure with large pores of ~24 nm^2 can act as a host material for molecules and atoms, for instance, working as nanoreactors for catalysis. After annealing at 420 K, a more complex structure, so-called flower-like, grows. These nano-

structures present different lattice parameters and molecular densities (see Table 4.3 in the Supplementary results). For higher temperatures (> 450 K) the molecules start to form a high-density structure composed of so-called diamonds.

Our DFT calculations and STM simulations for the experimentally observed honeycomb structures show an impressive agreement with the experiment and demonstrate the important role played by Cu adatoms in the stabilization of these structures. Our work demonstrates the design of highly ordered 2D MOFs with distinct symmetries and sizes. The respective pores with sizes of about ~13 nm^2 and ~24 nm^2 can be used as scaffold reactors. The highly ordered nanoporous network can also act as a host-guest material with potential applications in molecular switches in nanocircuits, catalysis, and gas sensing. The quantum confinement of surface electrons can be controlled at the atomic/molecular level by tailoring the molecular sizes and the MOF geometries. The quantum properties of such nanostructures present great potential for applications in nanoelectronics and photonics. The results reported for the TPyPB and TPyPPB molecules demonstrate that the molecular size plays a key role in the nanoporous arrangement. These molecules have the potential to be explored on non-metallic substrates and 2D materials (e.g. graphene and h-BN) with the use of co-deposited metallic atoms as coordination centers. The different molecular sizes can change the magnetic and catalytic properties of the metals, due to the formation of nanostructures with distinct geometries.

Methods

Sample preparation and STM details

The experiments were performed at UNICAMP in Campinas (Brazil) using an UHV surface science apparatus, consisting of two interconnected chambers. One chamber is equipped with X-ray photoelectron spectroscopy, LEED optics, a Knudsen cell for molecular sublimation, e-beam evaporators for metal deposition, and facilities for sample cleaning. The base pressure of the chamber was in the low 10^{-10} mbar. The other chamber is equipped with an STM SPECS Aarhus 150 with a SPECS SPC 260 controller, operating in a base pressure of low 10^{-11} mbar. The STM chamber is also equipped with Ar^+ sputtering for tip cleaning. The Cu(111) single crystal was cleaned by cycles of Ar^+ sputtering at 600 V at 7 μA cm^{-2} for 30 min, followed by annealing at 790 K for 15 min. The precursors TPyPB and TPyPPB were purchased from ET Chem Extension and sublimated using a homemade Knudsen cell at temperatures of 550 and 573 K, respectively. The deposition parameters (temperature, deposition time, and coverage) of the TPyPPB precursor are summarized in Table 4.1 in the Supplementary results. Cu was evaporated from a molybdenum crucible using a commercially available e-beam evaporator. All evaporators were degassed before sublimation. The STM measurements were performed at RT with a W tip in the constant current mode and

tunneling voltage (V_t) applied to the sample. The images were analyzed using Gwyddion and WSxM softwares [116, 157].

DFT Calculations

The DFT calculations were performed using the Imbabura cluster at Yachay Tech University by Prof. Duncan John Mowbray. All DFT calculations used the PBE exchange-correlation functional [158], with van der Waals (vdW) corrections included via the Grimme's D3 semiempirical method [159]. We performed our calculations using the projector-augmented wave method (PAW) [160] as implemented in the GPAW code [161, 162]. A linear combination of atomic orbitals (LCAO) [163] was used to represent the Kohn-Sham wave functions, with double-ζ-polarized (dzp) basis sets employed for the adatoms and atoms of the overlayer, and a single-ζ-polarized (szp) basis set employed for the atoms of the Cu(111) substrate. A grid spacing of $h \approx 0.2$ Å was used with an electronic temperature of $k_B T = 0.1$ eV and all total energies extrapolated to $T \rightarrow 0$. The adatoms and atoms of the overlayer were relaxed until a maximum force of less than 0.03 eV/Å was obtained, keeping the three layers of the Cu(111) substrate frozen at its experimental coordinates ($a \approx 3.61$ Å). The large dimensions of the supercells employed throughout ($L > 40$ Å) meant Γ-point calculations were sufficient to describe the wavefunctions.

The TPyPB honeycomb overlayer was modeled using two TPyPB molecules adsorbed on either a $16\mathbf{a_1} \times \mathbf{16a_2} \times \mathbf{19.2\hat{k}}$ or a $(12\mathbf{a_1} + \mathbf{6a_2}) \times (-\mathbf{6a_1} + \mathbf{18a_2}) \times \mathbf{25\hat{k}}$ supercell consisting of a three-layer Cu(111) substrate. The TPyPPB honeycomb overlayer was modeled using two TPyPPB molecules adsorbed on a $22\mathbf{a_1} \times \mathbf{22a_2} \times \mathbf{19.2\hat{k}}$ supercell consisting of a three-layer Cu(111) substrate. Formation energies E_{form} for each overlayer were calculated using

$$E_{form} = N_{ads}(E[Ads@Cu(111)] - E[Cu(111)]) + N_{ad}(E[Cu_{ad}@Cu(111)] - E[Cu(111)]) - (E[N_{ads}Ads + N_{ad}Cu_{ad}@Cu(111)] - E[Cu(111)])$$

where N_{ads} is the number of adsorbate molecules and N_{ad} is the number of adatoms that form the overlayer, $E[Ads@Cu(111)]$ is the total energy of an isolated adsorbate on the Cu(111) surface, $E[Cu(111)]$ is the total energy of the clean Cu(111) surface, $E[Cu_{ad}@Cu(111)]$ is the total energy of an isolated Cu adatom adsorbed on the most stable hollow site of the Cu(111) surface, and $E[N_{ads}Ads + N_{ad}Cu_{ad}@Cu(111)]$ is the total energy of the overlayer consisting of N_{ads} adsorbates and N_{ad} Cu adatoms.

The Tersoff-Hamann [164] approximation was employed for all STM simulations in constant-current mode as implemented in the code ASE [165].

CRediT authorship contribution statement

Alisson Ceccatto: Conceptualization, Validation, Formal analysis, Investigation, Visualization, Writing - Original Draft, Writing - Review & Editing. **Eva Marie Freiberger:** Investigation, Writing - Review & Editing. **Natalie J. Waleska-Wellnhofer:** Investigation, Writing - Review & Editing. **Simon Jaekel:** Investigation. **Duncan John Mowbray:** Formal analysis, Writing - Review & Editing. **Christian Papp:** Supervision, Writing - Review & Editing. **Hans-Peter Steinrück:** Conceptualization, Supervision, Project administration, Writing - Review & Editing, Funding acquisition. **Abner de Siervo:** Conceptualization, Supervision, Project administration, Resources, Writing - Review & Editing, Funding acquisition.

Declaration of competing interest

The authors declare that they have no known competing financial interests or personal relationships that could have appeared to influence the work reported in this paper.

Acknowledgements

The Brazilian authors acknowledge funding by Coordination for the Improvement of Higher Education Personnel (CAPES) through project PROBRAL 627947/2021; The São Paulo Research Foundation (FAPESP) through Projects 2021/08409-1, 2021/04411-1, 2007/54829-5 and The National Council for Scientific and Technological Development (CNPq) through projects 302400/2022-2. For calculations, DJM have employed the Imbabura cluster of Yachay Tech University, purchased under Contract 2017-024 (SIE-UITEY-007-2017). The German authors gratefully acknowledge funding by the German Research Foundation (DFG) through RTG 2681 (project number 491865171) at the Friedrich-Alexander-Universität Erlangen - Nürnberg and the TU Dresden, and SFB 953 (project number 182849149) at the Friedrich-Alexander-Universität Erlangen-Nürnberg, and by the German Academic Exchange Service (DAAD) through Project PPP 57598052.

Appendix: Supplementary results

This Supplementary results show additional STM and DFT data of TPyPB and TPyPPB on Cu(111) for different coverages and temperatures. It also shows tables containing information about the molecular size and honeycomb nanostructure details for the three similar precursors (TPyB, TPyPB, and TPyPPB), the evaporation parameters for TPyPPB deposition, and structural parameters for the honeycomb and flower-like nanostructures.

All depositions of TPyPPB molecule were carried out by a Kundsen cell with the Cu(111) substrate held at RT. The evaporation temperature (573 K) was monitored by a ther-

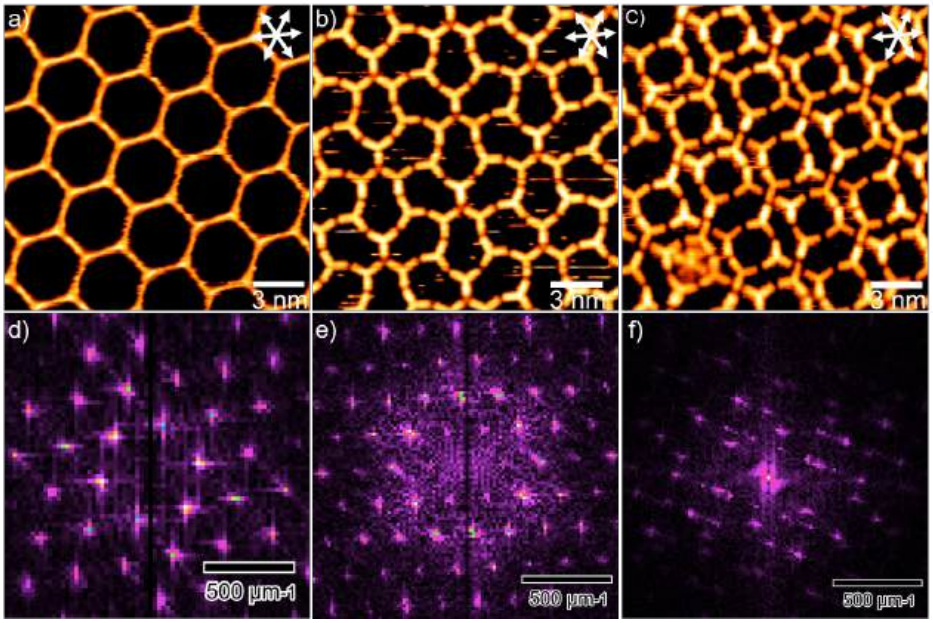

Figure 4.9: STM images of TPyPB forming a) honeycomb ($I_t = -650$ pA; $V_t = -1.4$ V), b) semi-regular ($I_t = -610$ pA; $V_t = -1.4$ V), and c) square motif ($I_t = -700$ pA; $V_t = -1.4$ V) on Cu(111). The white arrows indicate the main crystallographic directions of the Cu(111) surface. d-f) Corresponding FFT images for the three structures showing their symmetries.

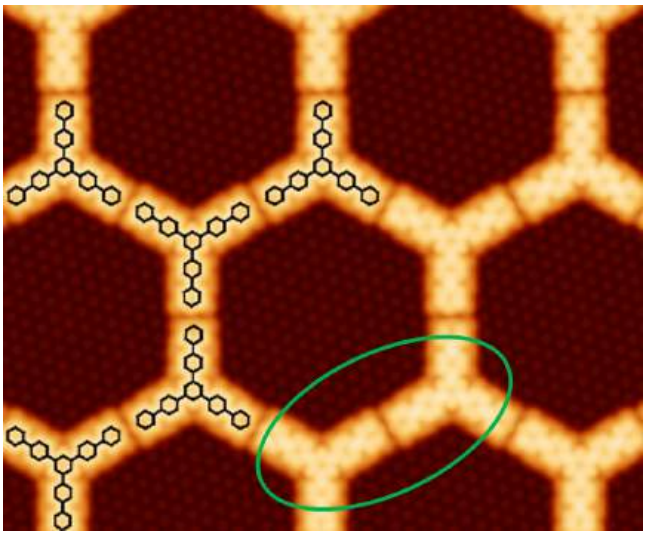

Figure 4.10: DFT simulation for the honeycomb nanostructure of TPyPB molecules coordinated by Cu atoms displaced from the upper surface layer, corresponding to a non-stable condition (for details see the manuscript). The molecular arms are not coordinated via head-on interactions as highlighted by the green oval.

mocouple located inside the crucible containing the molecular precursor. The deposition temperature ramp was kept constant (10 min) in all sublimations. Table 4.1 display the parameters of all the experiments present in this work. The molecular coverage and density were determined by statistical analysis of several STM images.

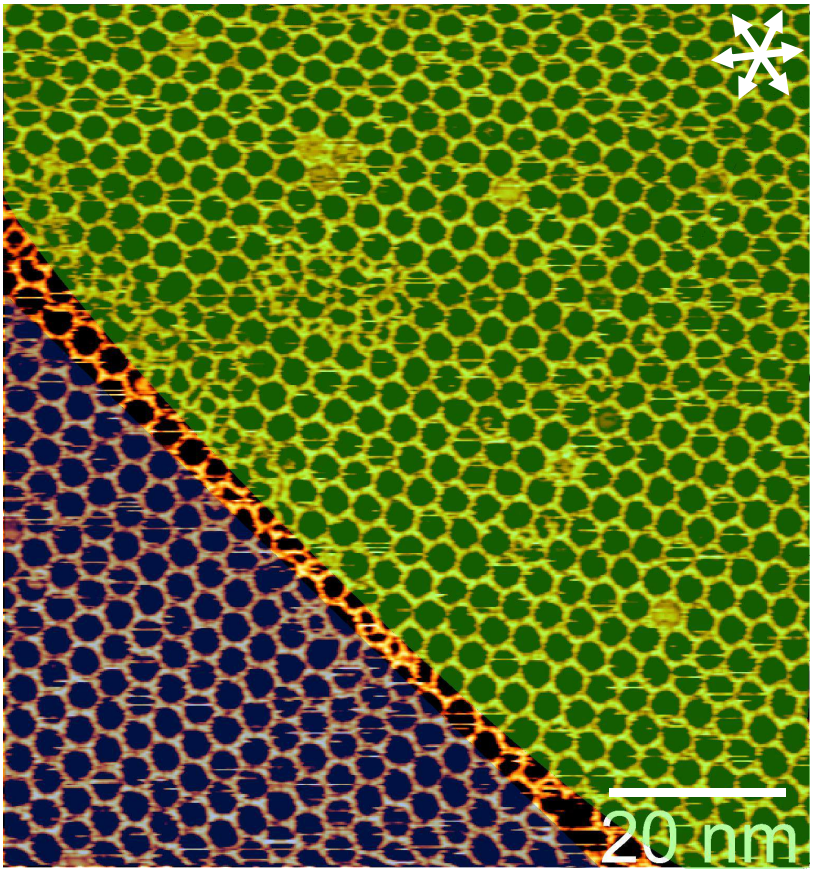

Figure 4.11: STM image showing two rotated domains (highlighted in green and blue) for the honeycomb networks of TPyPB precursor (I_t = -1.3 nA; V_t = -1.4 V).

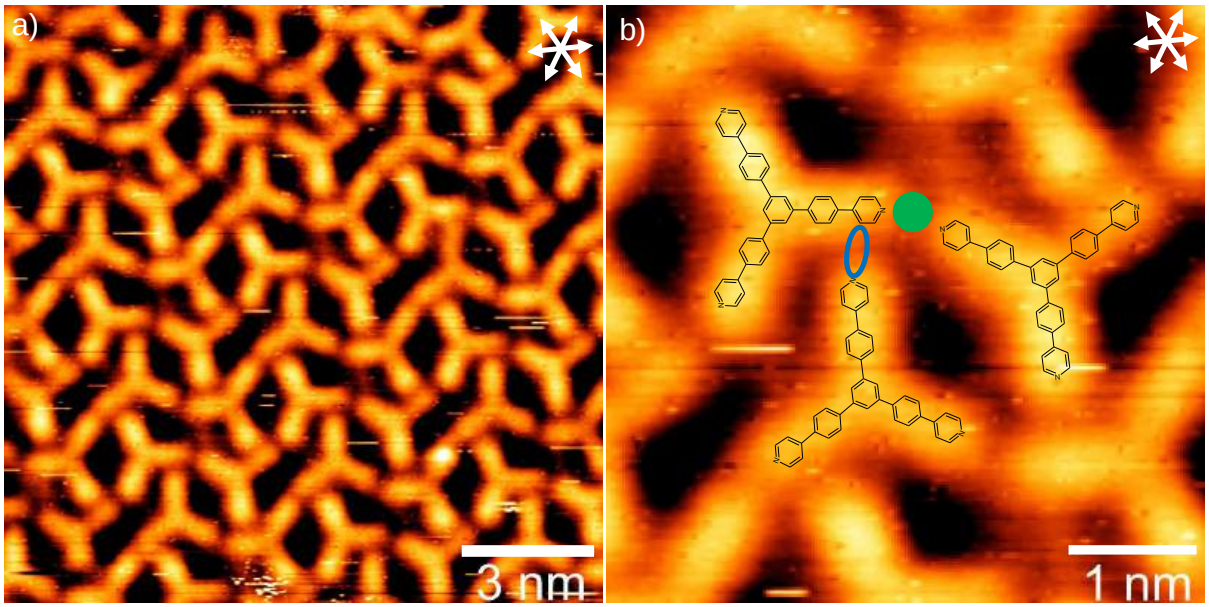

Figure 4.12: a) Close-packed self-assembly of molecule TPyPB on Cu(111) with a molecular density of ≈ 0.30 mol/nm^2, and b) zoom image highlighting the bonding motifs with the Cu-coordination center (green circle) and the hydrogen bond, N···H, between the neighboring molecules (blue oval) (I_t = -470 pA; V_t = -1.4 V).

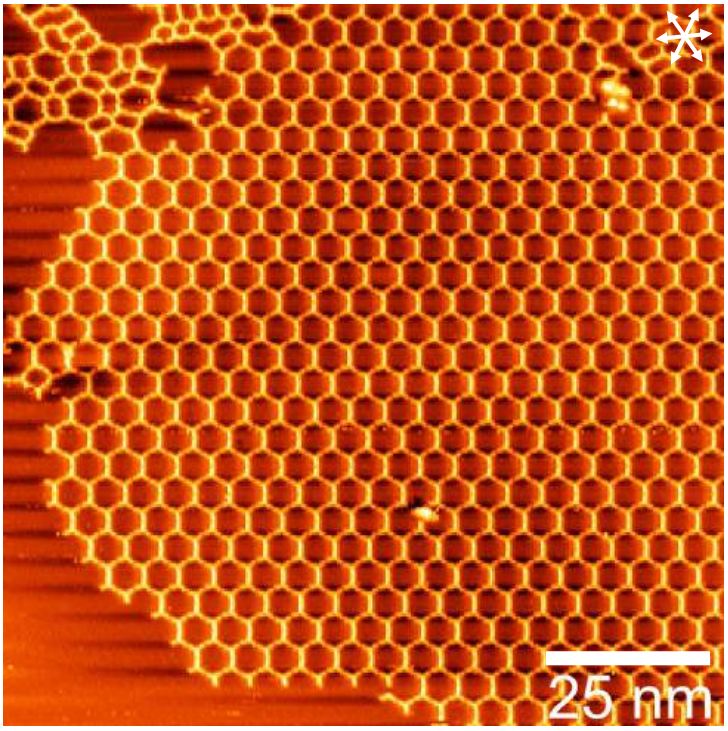

Figure 4.13: STM overview for the TPyPPB sample corresponding to 70% of coverage after annealing at 400 K for 5 minutes showing highly ordered honeycomb nanostructure with uncovered areas suggesting the self-limitation growth (I_t = -1.2 nA; V_t = -1.4 V).

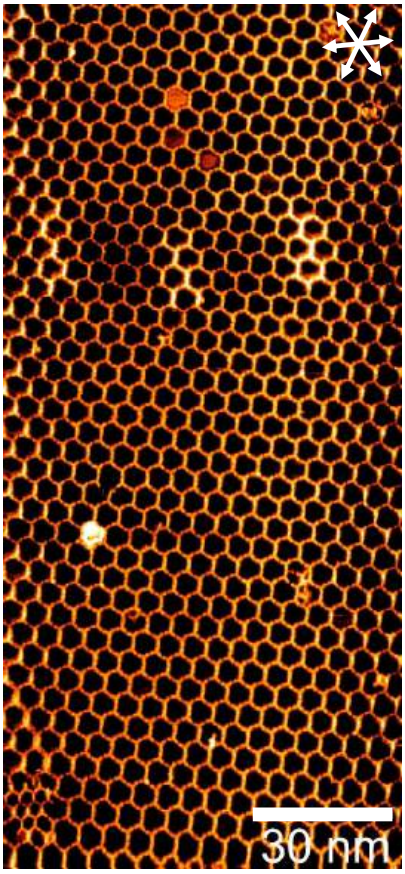

Figure 4.14: STM image for the honeycomb nanostructure with long-range domain after deposition of TPyPPB molecule with 90% coverage and subsequent annealing at 400 K for 3 hours (I_t = -1.8 nA; V_t = -0.05 V).

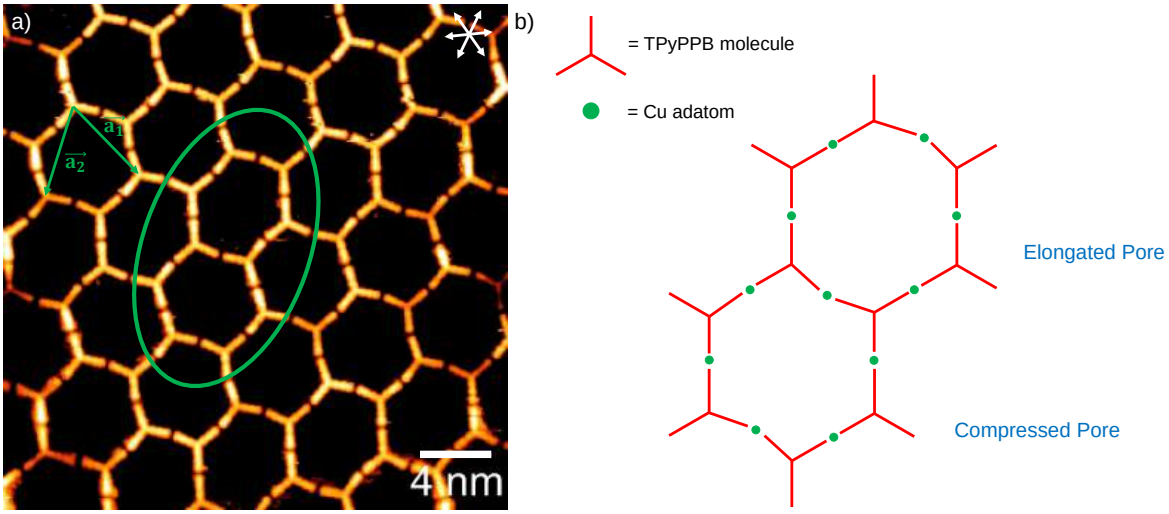

Figure 4.15: a) Honeycomb domain for the TPyPPB molecule, with the green oval highlighting the pore distortions of the nanostructure (I_t = -360 pA; V_t = -0.6 V). b) Illustration of the elongation and compression behavior of the pores.

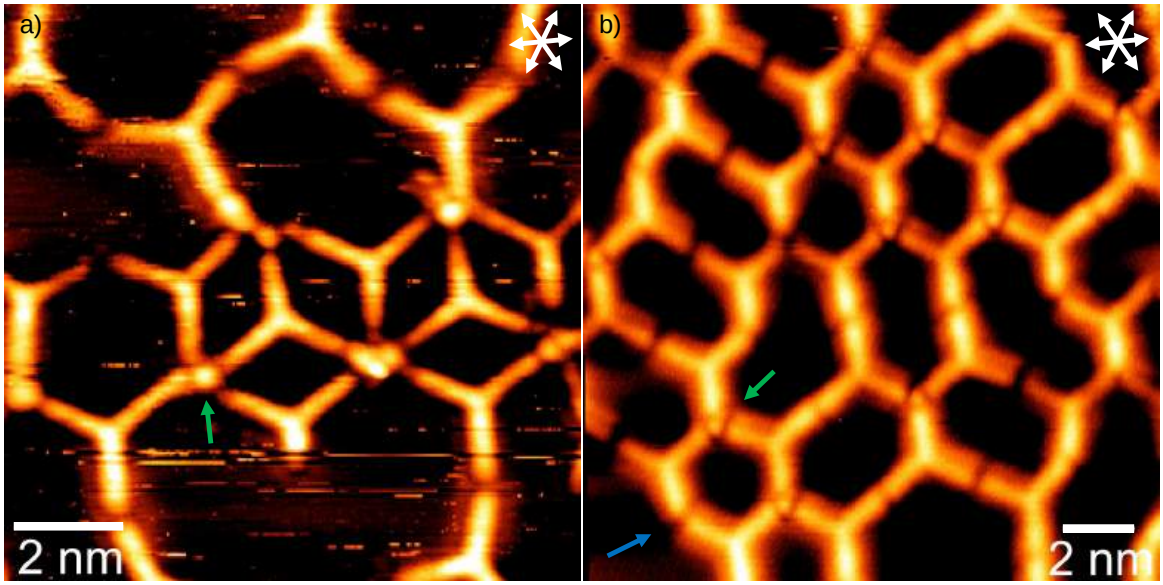

Figure 4.16: a),b) STM images showing distinct protrusions at the molecular junctions suggesting the presence of Cu adatoms for three- and four-fold coordination centers highlighted by the green arrows. For the two-fold coordinated molecules, this appearance is not observed as highlighted by the blue arrow. a) (I_t = -360 pA; V_t = -0.6 V). b) (I_t = -360 pA; V_t = -0.6 V).

Table 4.1: Star-shaped molecules TPyB, TPyPB, and TPyPPB arm lengths and Cu-coordinated honeycomb nanostructures lattice parameter and area

Molecule	Arm length	Lattice parameter	Hexagon side length	Pore area
TPyB	4.4 Å	(2.73 ± 0.05) nm [29]	(1.58 ± 0.03) nm	≈7 nm^2
TPyPB	8.8 Å	(3.9 ± 0.1) nm	(2.25 ± 0.06) nm	≈13 nm^2
TPyPPB	13.2 Å	(5.2 ± 0.1) nm	(3.00 ± 0.06) nm	≈24 nm^2

Table 4.2: TPyPPB deposition parameters

Exposure Time	Coverage Density	MOF Coverage
15 min	0.11 molec./nm^2	50%
20 min	0.15 molec./nm^2	70%
25 min	0.28 molec./nm^2	90%
30 min	0.37 molec./nm^2	Fully covered

Table 4.3: Structural parameters for TPyPPB ordered phases

Phase	Lattice parameter	Lattice angle	Phase density
Honeycomb	(5.2 ± 0.1) nm	60° ± 1°	0.08 TPyPPB/nm^2
Flower-like	(8.4 ± 0.1) nm	60° ± 2°	0.10 TPyPPB/nm^2

Chapter 5

Engineering Two-Dimensional Supramolecular Networks: The Role of Cl Atoms

---

Publication: **Alisson Ceccatto**, Gustavo Ramon Campi, Vanessa Carrenõ Diaz, Eidsa Brenda da Costa Ferreira, Natalie J. Waleska-Wellnhofer, Eva Marie Freiberger, Simon Jaekel, Christian Papp, Hans-Peter Steinrück, Duncan John Mowbray, Abner de Siervo. **"Engineering Two-Dimensional Supramolecular Networks: The Role of Cl Atoms"**.

This is the Manuscript version of an article under review process in **FlatChem**: Manuscript number: FLATC-D-24-00446.

All DFT calculations presented in this chapter were performed using the Imbabura cluster at Yachay Tech University by Prof. Duncan John Mowbray and Gustavo Ramon Campi.

On-surface synthesis is a powerful tool for engineering two-dimensional (2D) organic nanostructures by controlling intermolecular interactions between the building blocks. Herein, we explore the role of Cl adatoms in the synthesis and characterization of self-assembled 1,3,5-tris[4-(pyridin)-[1,1'-biphenyl]benzene (TPyPPB) networks on Ag(111), by combining scanning tunneling microscopy (STM), X-ray photoelectron spectroscopy (XPS), and density functional theory (DFT). In the absence of Cl, upon deposition at room temperature (RT), TPyPPB molecules form a highly ordered porous self-assembled monolayer (p-SAM) with triangular packing, stabilized by hydrogen bonds (N···H). In the presence of Cl adatoms, sublimated onto the surface using dichloro-(1,10-phenanthrolin)-platin(II) (Cl_2PhPt) a second molecular precursor, we observe a so-called mixed phase or inverted packing, depending on the applied growth procedure. The mixed phase is characterized by a non-periodic structure stabilized by intermolecular interactions between TPyPPB, Cl_2PhPt, and Cl. In contrast, when only Cl adatoms and TPyPPB are present on the Ag(111) surface, a non-porous SAM is obtained, stabilized by C–H···Cl hydrogen bonds.

Introduction

Over the past decades, on-surface reactions have been widely applied to design one- and two-dimensional supramolecular architectures [41, 166–168]. On-surface synthesis allows for control over the supramolecular nanostructure at the atomic and molecular levels, enabling the design of unique quantum materials [96]. Such tailoring of 2D nanostructures plays a key role in their applications in nanotechnology [169]. Particularly, self-assembled monolayers (SAMs) are suitable for organic nanoelectronics applications [170] due to their spontaneous and reversible non-covalent interactions, which allow for the fabrication of almost defect-free domains.

Several strategies have been explored to control the SAM properties, including the use of isotropic [25] and anisotropic substrates [171], functionalization of the organic building blocks [172], and codeposition of adatoms [31]. The latter process opens many possibilities to control the molecular architecture by inserting metallic and/or nonmetallic atoms. To date, adatom-mediated SAMs are most often prepared using single 3d metal atoms such as Cu [29, 173], Co [132], and Fe [174], or alkali metals such as Na [175]. Metal coordination has been found to be an efficient strategy for constructing SAMs, especially as it enables the tailoring of magnetic properties [33]. However, metal adatoms also have a strong influence on the electronic states near the Fermi level, which may alter the semiconductor behavior of the SAM [47, 176].

Nonmetallic adatoms, on the other hand, have less influence on the electronic properties of the SAM due to their weaker interactions with the molecular precursors. Indeed, the use of nonmetallic elements in the on-surface synthesis of organic molecules has attracted great attention in the past years. For example, Si atoms can be incorporated into

porphyrin macrocycles [46], O atoms can induce the self-assembly of quaterphenyl molecules [33], and Br atoms can be used to stabilize 2D supramolecular networks on metal surfaces [50]. Halogens are particularly important in on-surface synthesis as they can remain on the substrate as reaction byproducts after the dehalogenation of organic precursors, for example in the Ullmann coupling reaction [102]. The use of halogen bonding for the formation of 2D self-assembled networks has been widely explored for polycyclic aromatic hydrocarbons stabilized by intermolecular X···X (X = F, Cl, Br, I) and –C–H···X–C– bonds [48, 49, 177]. However, to date, the fabrication of highly ordered large-scale domains of supramolecular self-assembly with intermolecular interactions mediated by hydrogen bonds between the molecules and the halogen adatoms, –C–H···X···H–C–, is rarely reported [50, 178]. The Br-mediated self-assembly of 2,6-diphenylanthracene (DPA) molecules on Ag(111) and Cu(111) surfaces was demonstrated by Lu et al [50]. They showed that by controlling the concentration of Br adatoms on the surface the DPA molecules can be arranged in four distinct structures. While Br adatoms are electron-rich, H atoms are electron-deficient, thus stabilizing the supramolecular arrangement by attractive electrostatic interactions. Besides Br, also I adatoms have also been shown in on-surface synthesis to induce morphological transformations in 2D supramolecular SAMs [179]. However, less attention has been paid to the on-surface synthesis using Cl adatoms to modulate the self-assembled structures.

In this work, we explore the role of Cl atoms in the 2D supramolecular ordering of 1,3,5-tris[4-(pyridin-4-yl)-[1,1'-biphenyl])benzene (TPyPPB) [168] shown in the Figure 5.1a, on Ag(111). Two main supramolecular structures can be found, depending on the absence or presence of Cl adatoms. In the absence of Cl, scanning tunneling microscopy (STM) at room temperature (RT) reveals the formation of a porous SAM. Cl adatoms lead to changes in the TPyPPB arrangement, depending on the surface preparation before TPyPPB deposition, with either a mixed phase or so-called inverted packing being observed. Based on our density functional theory (DFT) calculations, we demonstrate that the Cl adatoms stabilize the inverted packing, forming –C–H···Cl bonds between the TPyPPB molecules. To the best of our knowledge, the synthesis of a SAM stabilized exclusively by –C–H···Cl bonds has so far not been explored.

Results and discussion

Upon deposition of submonolayer coverages of TPyPPB molecules on the clean Ag(111) surface at RT, we observed via STM measurements the formation of a 2D supramolecular porous network as shown in Figure 5.2a. This arrangement extends over tens of nanometers with a low density of defects, as shown in Figure 5.6 in the Supplementary results appendix. This suggests there is only a weak interaction between the molecular precursors and substrate, as expected for a SAM. The zoom-in STM image in Figure 5.2b displays triangular pores, one of which is highlighted in blue. This nanostructure is thus denoted as triangular

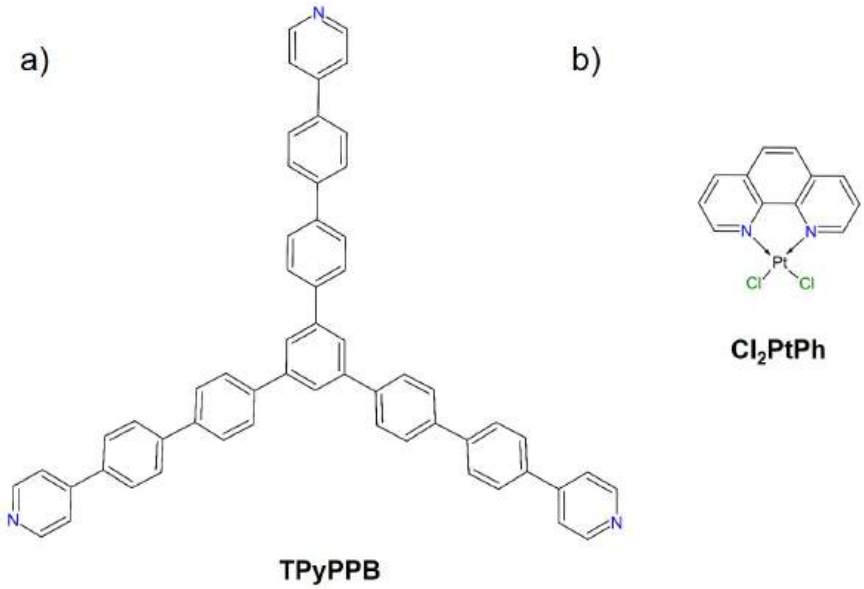

Figure 5.1: Chemical structure of a) TPyPPB and b) Cl_2PhPt precursors.

packing, as also shown in Figure 5.3a. In the high-resolution STM image in Figure 5.2c, we can identify the three-legged molecules, in excellent agreement with our DFT simulations in Figure 5.2d. The hexagonal unit cell of the triangular structure is characterized by lattice vectors $|\vec{a_1}| = |\vec{a_2}| = (1.9 \pm 0.1)$ nm, in good agreement with our calculated lattice vector of $\approx$ 2.0 nm (see Figure 5.2e). The lattice vectors are rotated by 30° ± 2° with respect to the main crystallographic directions of the substrate, which are indicated by the blue lines at the top of Figure 5.2b. For our DFT calculations, we defined the formation energy of the different structures regarding the isolated TPyPPB molecule on Ag(111) surface (see Section 5 for details). The calculated formation energy of triangular packing is E_f = -0.30 eV/molecule with a molecular adsorption height of $d \approx 3.2$ Å. This suggests that the molecules are physisorbed rather than chemisorbed, as illustrated in the side-view of Figure 5.2e. The weak molecule–substrate interaction facilitates the formation of the molecular network with extended highly ordered domains and a low defect density. From the unit cell, we determine a pore area (highlighted in blue in Figure 5.2b) of ≈1.73 nm^2 and a molecular density of (0.32 ± 0.02) molecules/nm^2 (see Table 5.1). Such a nanostructure with a regular distribution of pores in extended domains has the potential to be an efficient host-guest material for small molecules or atoms.

Table 5.1: Structural parameters of the self-assembled nanostructures formed

Packing	$\|\vec{a_1}\|$ (nm)	$\|\vec{a_2}\|$ (nm)	Density (Molec./nm^2)	Molec. per unit cell
Triangular	(1.9 ± 0.1)	(1.9 ± 0.1)	(0.32 ± 0.02)	1
Inverted	(1.9 ± 0.1)	(3.4 ± 0.2)	(0.30 ± 0.02)	2

To investigate the behavior of TPyPPB molecules in the presence of Cl adatoms, the clean Ag(111) surface was first exposed to a second molecular precursor, that is, Cl_2PhPt

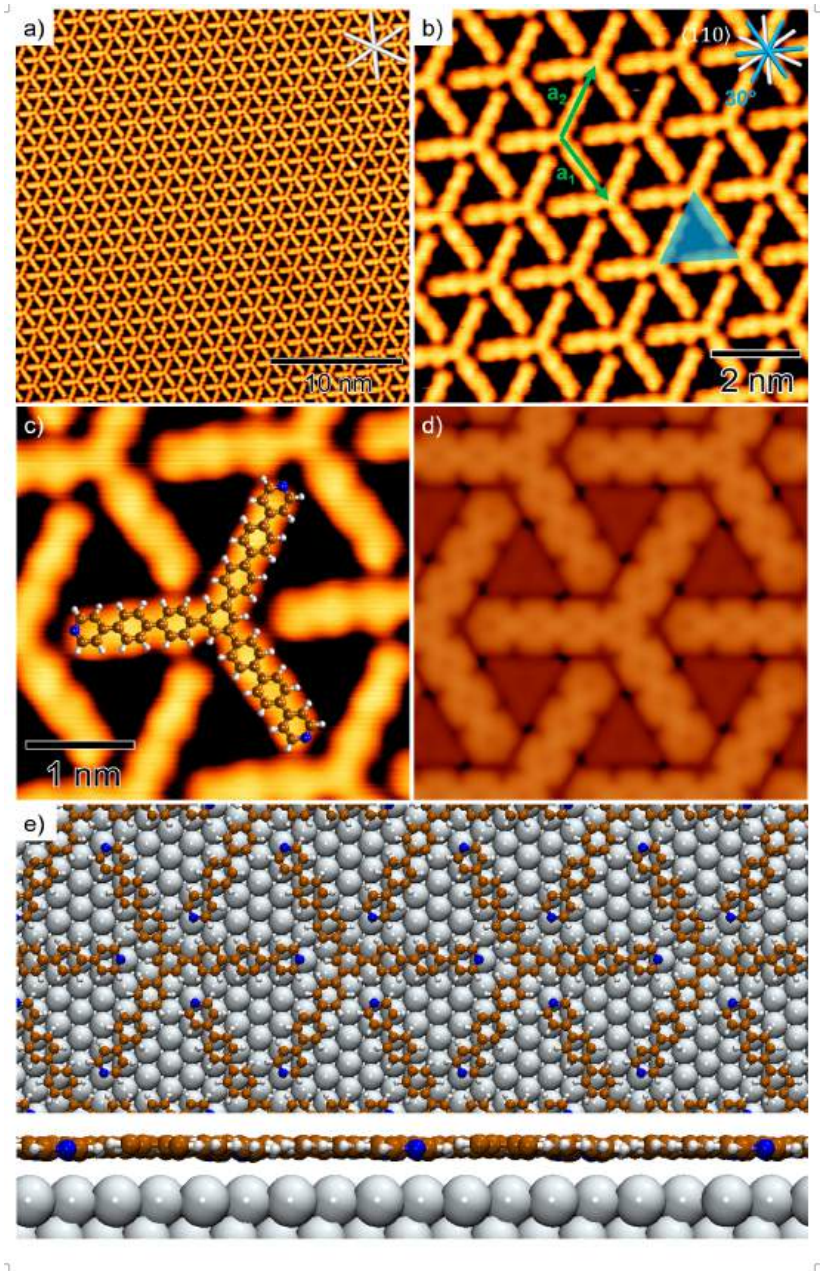

Figure 5.2: a) STM images of the triangular packing forming extended domains on Ag(111). The white lines indicate the high-symmetry directions of the surface. b) STM image with the lattice vectors $\vec{a_1}$ and $\vec{a_2}$ highlighted in green. The domains are rotated by $\approx 30°$ from the high-symmetry direction of the substrate as highlighted by the blue lines. c) High-resolution STM image with superimposed TPyPPB molecular structure showing the intermolecular interactions. d) DFT simulation of the triangular packing stabilized by hydrogen bonds. e) Top- and side-view of the DFT adsorption configuration of the triangular packing (Ag in gray, C in brown, and N in blue). a) ($I_t = 230$ pA; $V_t = -1.0$ V), b) ($I_t = 230$ pA; $V_t = -0.3$ V), c) ($I_t = 280$ pA; $V_t = -0.3$ V).

molecules. This molecule serves as a source of halogen adatoms since it can be dehalogenated by thermal annealing. Upon deposition of submonolayer coverages (≤0.5 ML) of Cl_2PhPt on the Ag(111) substrate at RT, the molecules form close-packed self-assembled domains as highlighted in green in Figure 5.7 of the Supplementary results. Subsequently, the sample was annealed at 500 K for 30 minutes. After the sample cooled down to RT, TPyPPB molecules were deposited at submonolayer coverages. The resulting molecular arrangement

in Figure 5.4a consists of a nonperiodic arrangement. In addition to the three-legged molecules, the STM images show two additional features, as highlighted by the green and blue arrows in Figures 5.4a and 5.4b, respectively.

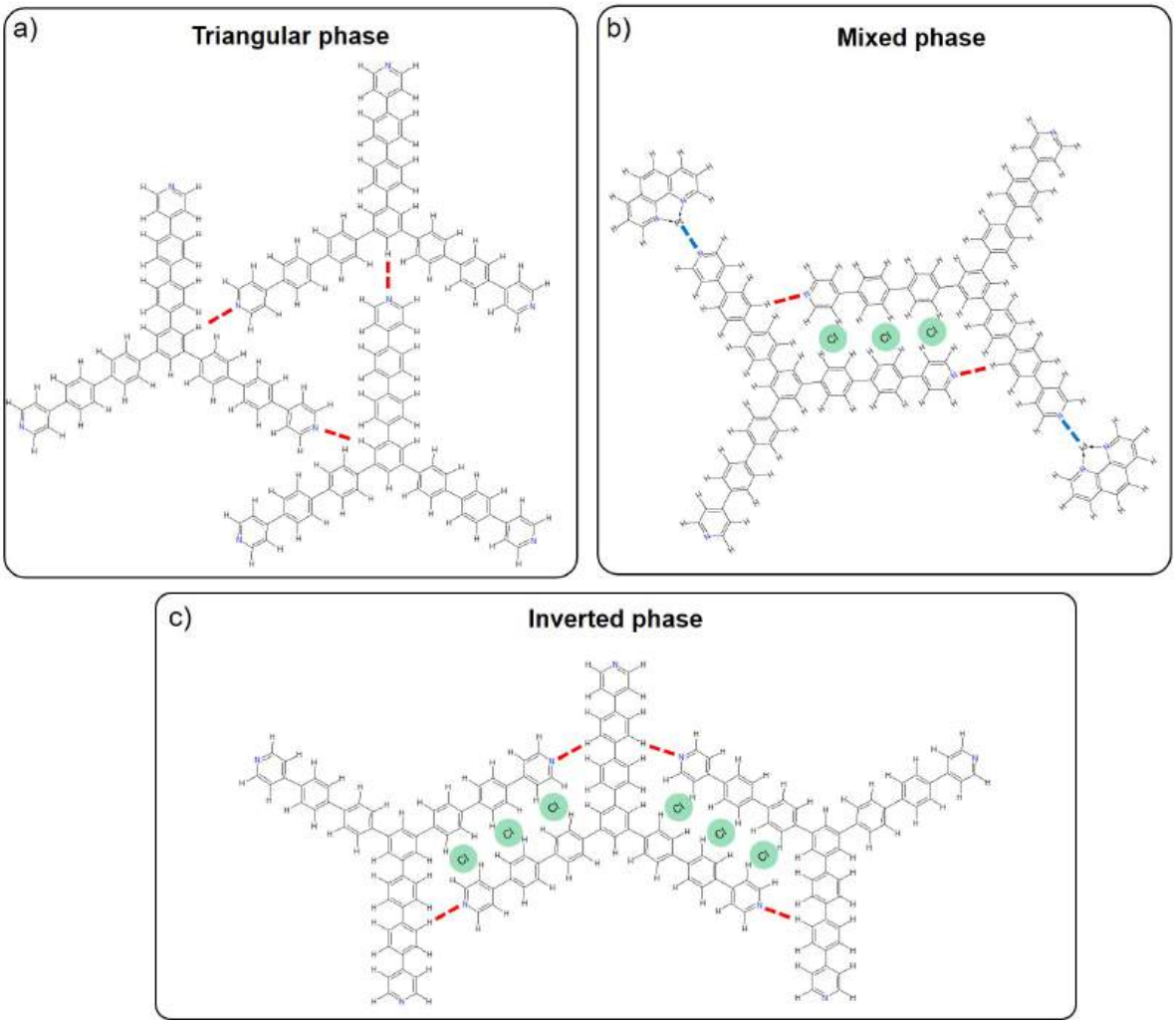

Figure 5.3: Molecular models of the a) triangular, b) mixed, and c) inverted phases observed depending on the adsorbed molecular species. The red segmented lines represent the hydrogen bonding between the molecules. The blue line depicted the Pt–N coordination. The green circles illustrate the Cl adatoms interacting with the TPyPPB arms.

To verify the dechlorination of Cl_2PhPt, we performed XPS measurements in the Cl 2p region for a sample with higher coverage (≈ 1ML), in order to obtain a better signal-to-noise ratio. Prior to XPS, the sample was annealed at 450 K for 30 minutes. Unfortunately, for such molecular coverages, it was impossible to resolve the molecules in the STM at RT. The Cl 2p spectrum in Figure 5.4c can be fitted by the doublet of a single Cl species on the surface. It is assigned to the Cl $2p_{1/2}$ and $2p_{3/2}$ peaks, with an area ratio of 1:2 and a spin-orbit coupling splitting of 1.7 eV. The Cl $2p_{3/2}$ peak binding energy of 197.7 eV is attributed to Cl adatoms chemisorbed on Ag(111), in line with previous investigations of aryl chlorides on the same surface [180]. We thus conclude that the deposition of Cl_2PhPt followed by annealing at T ≥ 450 K leads to the extraction of both Cl atoms from the complex, yielding a new

molecular complex, which we denote as PhPt. This new molecular species can potentially interact with the pyridyl end groups of the TPyPPB molecules via the Pt atoms, forming a Pt-coordinated center (Pt–N). Evidence for this behavior is indeed observed in the inset image in Figure 5.4a, where after TPyPPB deposition, C-shaped features at the end of the TPyPPB arms (green arrow) are observed, which are assigned to PhPt molecules (see the model in Figure 5.3). Moreover, additional rounded features located between the TPyPPB molecular arms highlighted by a blue arrow in Figure 5.4b, are assigned to Cl adatoms that are cleaved off the Cl_2PhPt precursor. Investigations with brominated precursors have shown similar features in the regions close to the molecules in the STM images, assigned as the Br adatoms that were cleaved from the molecules [102, 181].

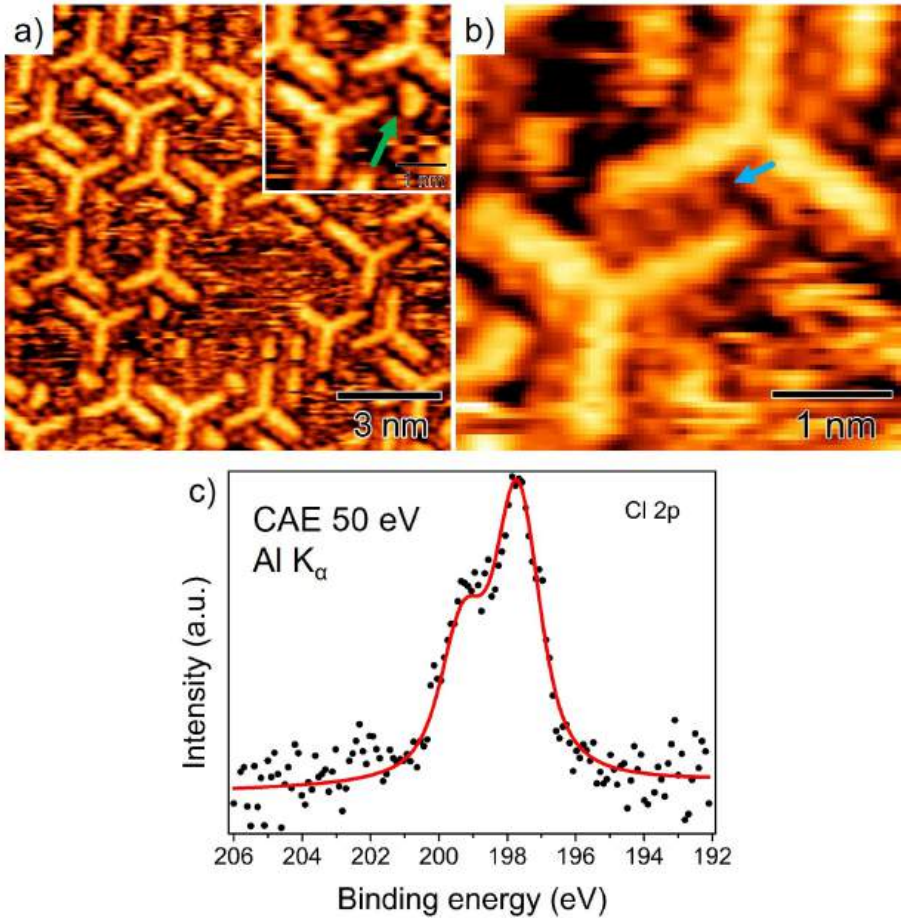

Figure 5.4: a) STM image of the Cl_2PhPt molecules (green arrow) annealed at 450 K followed by the deposition of TPyPPB (I_t = 310 pA; V_t = −0.6 V). b) High-resolution STM image of the TPyPPB molecules with three Cl adatoms between the molecular arms, highlighted by the blue arrow (I_t = 310 pA; V_t = −0.6 V); c) XPS spectrum at Cl 2p core level of the halogen adatoms dissociated on top of Ag(111) surface.

Interestingly, in the mixed phase, the TPyPPB molecules interact with their arms aligned side-by-side (see Figure 5.3b and Figure 5.4b) while in the triangular packing, the molecules interact head-on with the pyridyl groups pointing towards the benzene core of three neighboring molecules (see Figure 4.2c, 4.2e, and Figure 5.3a). Such behavior suggests that the pre-adsorption of the Cl_2PhPt followed by thermal annealing induces the mixed

phase of the TPyPPB molecules, with multiple interactions of the three-legged molecule with Cl adatoms and with PhPt molecules.

To shed light on the role of the halogens in the TPyPPB arrangement, we changed the growth protocol to avoid Pt-Py coordination. In the first step, we pre-adsorbed Cl_2PhPt on the Ag(111) surface at medium coverages (≥0.5 ML) and annealed to 450 K for 30 minutes, to abstract the Cl atoms from the molecules. Thereafter, the surface was gently sputtered with Ar^+ with energy of 600 eV for 30 minutes to remove most of the PhPt molecules, and annealed at 770 K. As a final step, the TPyPPB molecules were deposited at RT with submonolayer coverages. The resulting STM images in Figure 5.5a and b reveal the formation of a new phase with a distinct appearance, which is different from that of the triangular and mixed phases, (for comparison see Figure 5.3a and b), indicating different intermolecular interactions. This new phase is a highly ordered 2D self-assembly with a low number of defects. The STM images in Figure 5.8a and b in the Supplementary results display the formation of extended domains of the inverted packing.

In contrast to the triangular phase with triangular pores and a hexagonal unit cell containing one molecule (Figure 5.3a), the new phase has a rectangular unit cell containing two molecules, which are rotated by 180° to each other, which we denote as inverted packing (Figure 5.3c). In this packing, only one (instead of three) arm interacts head-on with the adjacent molecule along the $\vec{a_1}$ unit cell vector, forming a linear chain of identically oriented molecules. The other two arms point to the side of the neighboring, 180° rotated, molecules (which also form linear chains), yielding a side-by-side arrangement for these arms, as shown in Figure 5.5b and with higher resolution in Figure 5.5c. The unit cell with $\vec{a_1}$ = (1.9 ± 0.1) nm and $\vec{a_2}$ = (3.4 ± 0.2) nm is indicated in Figure 5.5b; it has a molecular density of (0.30 ± 0.02) mol nm^{-2}. By comparison to STM images with atomic resolution of Ag(111), we deduce that the molecular arms are aligned along the high symmetry directions of the surface, as indicated by the white lines at the top of Figure 5.5b.

In Figure 5.5b and c, the STM images show bright protrusions in the regions between the TPyPPB arms, as highlighted in blue. We assign these protrusions to Cl adatoms interacting with the TPyPPB molecules, similar to the mixed phase in Figure 5.4b. To address the Cl adatom's role in the stabilization of the inverted packing, we performed DFT calculations including the halogens in the region between the TPyPPB arms. Figure 5.5d and e show the STM simulation and the optimized adsorption geometry of the inverted packing, respectively. The simulation shows that the Cl adatoms appear as bright protrusions, as highlighted by the blue circle in Figure 5.5d, in agreement with the overall appearance in the STM measurements. Moreover, the Cl adatoms (green balls in Figure 5.5e) sit on hollow sites of the Ag(111) surface, which is the most stable adsorption site for Cl adatoms on Ag(111). [182] The lattice parameters of the supramolecular arrangement with two molecules per unit cell are $|\vec{a_1}| \approx 2.0$ nm and $|\vec{a_2}| \approx 3.5$ nm in our calculations, in good agreement with our experimental results. The DFT calculations of the inverted packing were performed for two scenarios:

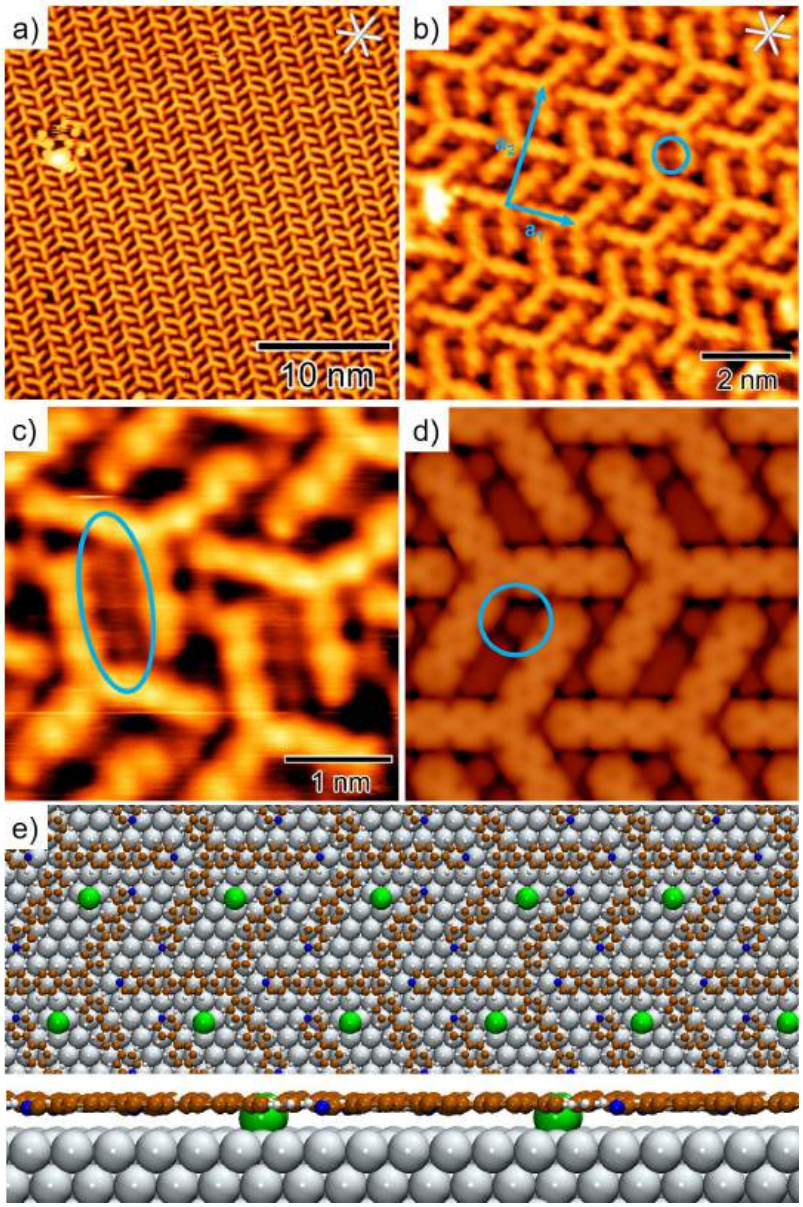

Figure 5.5: a) STM overview image of the extended domains of inverted packing with b) lattice vectors $\vec{a_1}$ and $\vec{a_2}$ with the Cl adatom highlighted by the blue circle. The molecular arms are aligned along the high-symmetry surface directions (white lines). a) (I_t = 260 pA; V_t = −1.3 V), b) (I_t = 690 pA; V_t = −1.4 V). c) High-resolution STM image with the bright protrusion assigned to Cl adatoms highlighted in blue (I_t = 690 pA; V_t = −1.4 V). d) DFT simulation of the inverted packing with one Cl adatom in the region between the TPyPPB arms, highlighted by the blue circle; e) Top- and side-view of the DFT adsorption configuration of the inverted packing with one Cl adatoms (Ag in gray, C in brown, N in blue, and Cl in green).

without and with one Cl adatom between the molecular arms. In both cases, we included van der Waals corrections (see Section 5 for more details). The DFT calculations of the inverted packing without the Cl adatoms show a formation energy of E_f = -0.23 eV/molecule. By inserting one Cl adatom per unit cell (see Figure 5.5e), the inverted packing is further stabilized with E_f = -0.34 eV/molecule, suggesting that the halogen adatoms increase the molecular overlayer stability. However, the DFT calculations of the triangular packing with one Cl adatom per unit cell show a formation energy of -0.50 eV/molecule.

To further understand the interaction between the TPyPPB and the Cl adatoms, we calculated the charge transfer between them. We expect an attractive electrostatic interaction due to the high electronegativity of the Cl atoms. Indeed, we find a significant charge transfer from Ag to Cl adatoms (≈0.55 e per atom), resulting in negatively charged Cl adatoms, while the TPyPPB molecules have a weaker negative charge of 0.2 e per molecule. Considering that the Cl adatoms interact with the six closest H atoms in the TPyPPB arms, we obtain a charge transfer of ≈0.06 e per atom from the H to the Cl adatoms. The presence of the Cl adatoms leads to distinct hydrogen bonds, C–H···Cl, stabilizing the 2D self-assembly. This unconventional hydrogen bond was recently reported for 2,6-diphenylanthracene (DPA) molecules with Br adatoms on Au(111). [50] Similarly as reported for Br, Cl adatoms can interact at maximum with six H, considering the halogens in the adsorption hollow-sites. For this reason, we suggest this additional interaction with Cl adatoms leads to the observed change in the phase formed since the molecules can interact side-by-side in the inverted packing compared to the triangular phase. Furthermore, for samples with low dosages of Cl, we observe an intermediate behavior, with TPyPPB molecules forming the triangular packing, and rows with inverted packing in between, as highlighted in green in Figure 5.9 in the Supplementary results.

Conclusions

We investigated the formation of highly ordered 2D porous supramolecular networks of TPyPPB on Ag(111) and its modification by deposited chlorine. The porous nanostructure is characterized by regular triangular pores and is stabilized by N···H hydrogen bonds between the TPyPPB molecules. Such a regular pore network with a pore area of 1.73 nm^2 is a suitable matrix for atom/molecular confinement with possible applications in the areas of gas sensors and single-atom catalysts. The structure of the network can be modified by depositing the Cl containing precursor Cl_2PhPt, followed by a dechlorination reaction, where TPyPPB forms two different new phases, that is, a mixed and an inverted phase. If after dechlorination the resulting dechlorinated PhPt complex remains on the surface, the TPyPPB molecules interact with both Cl adatoms and the remaining dechlorinated complex via its Pt atom, forming the mixed phase. However, when removing the dechlorinated complex by sputtering, the TPyPPB molecules interact only with the Cl adatoms. This interaction leads to a non-porous highly ordered phase stabilized by unconventional C–H···Cl hydrogen bonds. Our work sheds light on the formation of a halogen-mediated highly ordered 2D-SAM, opening a plethora of possibilities for coordinated nanostructures using nonmetal adatoms.

Methods

Experimental details

Sample preparation, STM, and XPS measurements were performed at UNICAMP in Campinas (Brazil) using a UHV apparatus. The experimental setup consists of two interconnected XPS and STM chambers. The XPS chamber is equipped with e-beam and Knudsen cell evaporators, LEED optics, cleaning facilities, and XPS, operating at a base pressure in the low 10^{-10} mbar range. The base pressure in the STM chamber was in the low 10^{-11} mbar range. XPS measurements were performed with a SPECS Phoibos 150 hemispherical electron analyzer using an Al Kα anode. The XPS spectra were calibrated using the Ag 3d core-level peaks as a reference with 50 eV pass energy resulting in an overall energy resolution of $\approx$ 0.5 eV. The STM measurements were carried out using an SPECS Aarhus 150 microscope operated with a *SPECS SPC* 260 controller. The measurements were performed using a W tip cleaned in situ by Ar^+ sputtering in constant current mode with a bias voltage applied to the sample. The Ag(111) surface was prepared by cycles of Ar^+ sputtering (600 V@7 μA cm^{-2}) followed by annealing at 770 K for 30 min with slow cooling ramp ($\approx$ 0.3 K/s) to ensure well-ordered and large terraces. TPyPPB molecules were purchased from ET Chem Extension and deposited using a homemade 3-fold Knudsen cell evaporator at 653 K from a quartz crucible. The Cl_2PhPt molecules were purchased from Sigma-Aldrich and evaporated in the same 3-fold Knudsen cell evaporator at 623 K. All deposition steps were performed with the Ag(111) substrate held at RT. All STM images were analyzed using Gwyddion [116] software.

Computational details

All DFT calculations were performed using the Imbabura cluster at Yachay Tech University by Prof. Duncan John Mowbray and Gustavo Ramon Campi. The PBE exchange-correlation functional [158] with van der Waals (vdW) corrections included via the Grimme's D3 semiempirical method [159] was employed in all DFT calculations. Our calculations used the projector-augmented wave method (PAW) [160] as implemented in the GPAW code [161, 162]. To represent the Kohn-Sham wavefunctions, a linear combination of atomic orbital (LCAO) [163] was implemented, with double-ζ-polarized (dzp) basis sets employed for the molecular overlayer and Cl adatoms, and a single-ζ-polarized (szp) basis set employed for the atoms of the Ag(111) substrate. The adatoms and atoms of the overlayer were relaxed until a maximum force of less than 0.03 eV/Å was obtained, keeping the three layers of the Ag(111) substrate frozen at its experimental coordinates ($a \approx 4.09$ Å), with more than 17 Å of vacuum separating periodic images of the surface slab. The large dimensions of the supercells employed throughout ($L > 40$ Å) meant Γ-point calculations were sufficient to describe the wavefunctions.

Specifically, calculations of the triangular TPyPPB overlayer employed a $\vec{a}_1$ =

$12a\sqrt{3/2}\hat{x}$, $\vec{a}_2 = 12a(1/\sqrt{2}\hat{x} + 1/\sqrt{6}\hat{y})$, $\vec{a}_3 = 25.6\hat{z}$, and calculations of the inverted TPyPPB overlayer employed a $\vec{a}_1 = 14a/\sqrt{2}\hat{x}$, $\vec{a}_2 = 14a(1/2\hat{x}+\sqrt{3}/2\hat{y})$, $\vec{a}_3 = 25.6\hat{z}$. The Tersoff-Hamann [164] approximation was employed for all STM simulations in constant-current mode as implemented in the code ASE [165].

Acknowledgements

The Brazilian authors gratefully acknowledge funding by Coordination for the Improvement of Higher Education Personnel (CAPES) through project PROBRAL 627947/2021; The São Paulo Research Foundation (FAPESP) through Projects 2022/12929-3, 2021/08409-1, 2021/04411-1, 2007/54829-5; and The National Council for Scientific and Technological Development (CNPq) through projects 302400/2022-2. The German authors gratefully acknowledge funding by the German Research Foundation (DFG) through RTG 2681 (project number 491865171) at the Friedrich-Alexander-Universität Erlangen-Nürnberg and the TU Dresden. This work used the Imbabura cluster of Yachay Tech University, which was purchased under contract No. 2017-024 (SIE-UITEY-007-2017).

Appendix: Supplementary results

This Supplementary results appendix shows additional STM measurements of the TPyPPB and Cl_2PhPt molecules on Ag(111).

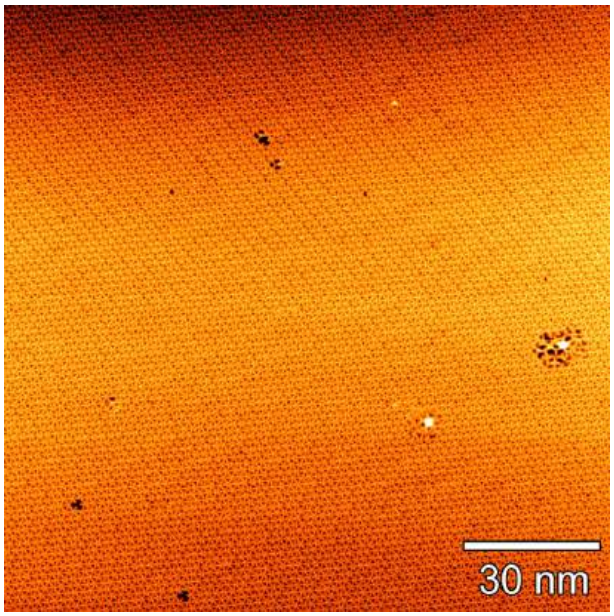

Figure 5.6: Triangular packing forming extended domains (>100 nm) (I_t = 230 pA; V_t = −1.0 V).

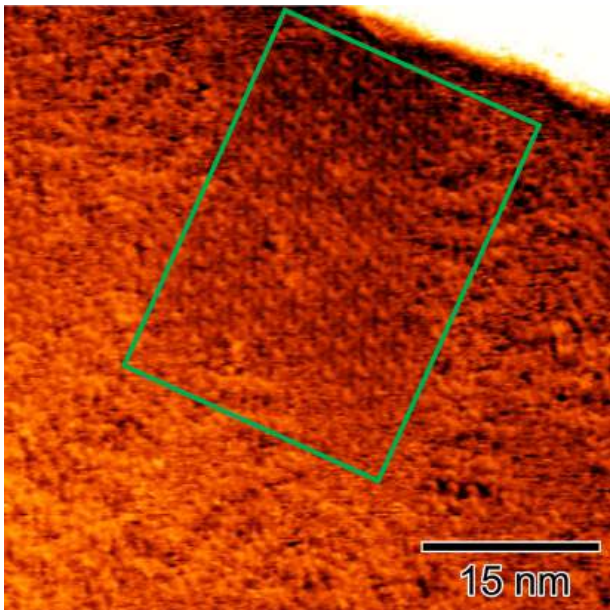

Figure 5.7: Self-assembly of Cl_2PhPt molecules on Ag(111) at RT (I_t = 270 pA; V_t = −1.4 V).

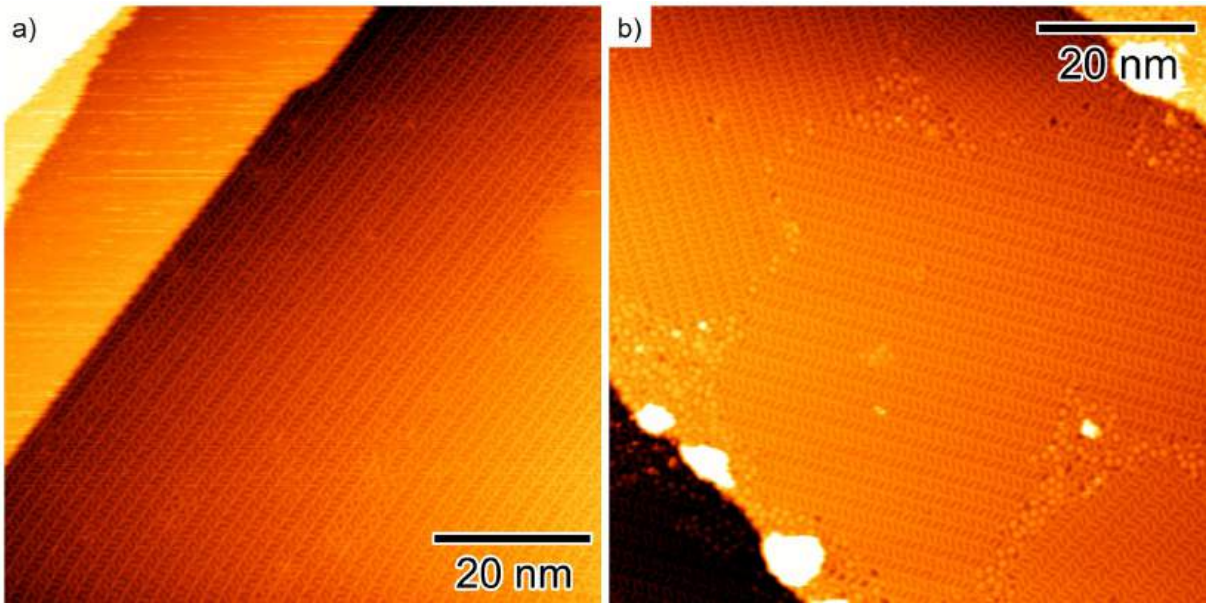

Figure 5.8: a,b) Highly-ordered inverted packing forming extended domains (>100 nm). a) (I_t = 390 pA; V_t = −0.9 V); b) (I_t = 350 pA; V_t = −1.3 V).

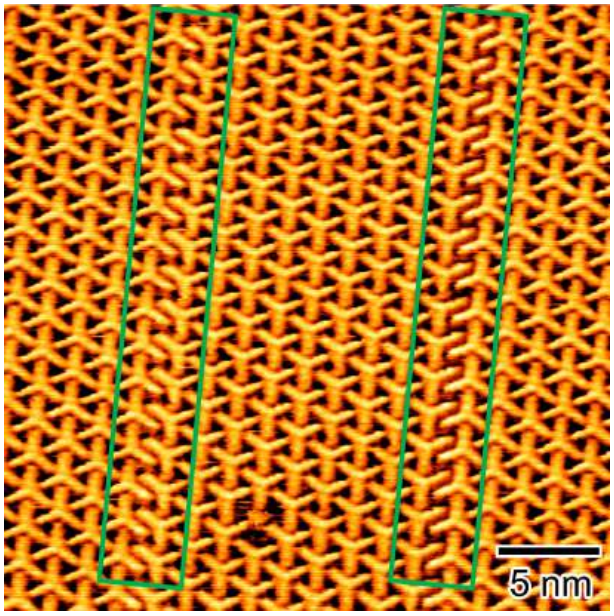

Figure 5.9: STM image of the triangular packing in the condition of low-dosing of Cl adatoms, showing TPyPPB molecules bonded side-by-side highlighted in green ($I_t = 200$ pA; $V_t = -0.7$ V).

Chapter 6

Design of Complex Cobalt-Mediated Supramolecular Porous Nanostructures

In Chapter 5, we showed the role of nonmetal adatoms (Cl) in the formation of highly ordered nanostructures on Ag(111). The TPyPPB molecules interact via unconventional hydrogen bonds between the Cl adatoms and the hydrogens in the molecule. Herein, we explore the formation of 2D-MOFs still using the same precursor on Ag(111) by providing Co adatoms. For the Cu-coordinated 2D-MOFs shown in Chapter 4, the metal-coordination centers are intrinsically on the surface. In this chapter, by combining scanning tunneling microscopy and X-ray photoelectron spectroscopy results, we demonstrated the control over the metal-coordination centers by choosing a suitable surface template and metal adatoms. Different from Cu, Co is a magnetic metal, opening the possibility to also explore the magnetic properties of 2D-MOFs.

On Ag(111) we have demonstrated that the TPyPPB molecules do not interact with the Ag adatoms and form the triangular packing, stabilized by hydrogen bonds. The presence of extrinsic adatom on the surface can induce a phase transition of the nanoarchitecture formed, as shown for the Cl adatoms in Chapter 5. To investigate the role of metal adatoms, especially magnetic atoms, we investigated the behavior of the TPyPPB molecules on Ag(111) in the presence of Co adatoms. Before the deposition of TPyPPB molecules, we estimated the Co coverage based on XPS and STM results. The XPS spectra were calibrated using the Ag 3d core-level peaks as a reference and using the Al K_α X-ray source. The measurements were performed with 50 eV pass energy resulting in an overall energy resolution of ≈ 0.5 eV. To obtain high coverages of Co, we performed the deposition on Ag(111) for 4 minutes using an emission current of 10 mA with a flux of ions (I_ϕ) of ≈ 20 nA (≈ 0.1 ML/minute). The blue spectrum displayed in Figure 6.1a shows the XPS measurement at Co $2p_{3/2}$ core-level for this deposition. To have a precise control of the evaporation, we decreased the emission current of the evaporator down to 6 mA resulting in a flux of ions of ≈ 2 nA (≈ 0.01 ML/minute). By comparing the two samples, the XPS for the former evaporation reveals a drastic decrease in the Co coverage, as shown in the red spectrum in Figure 6.1a. In Figure 6.1b, we display a zoom-in of the red spectrum of Figure 6.1a, where it is clear that the main Co species is located at 778.1 eV, where we identify as a metallic Co, similar to the blue spectrum.

Figure 6.1c and d, show the STM measurement for the sample with high (I_ϕ = 20 nA) and low (I_ϕ = 2 nA) coverages, respectively. Both STM images reveal the presence of large bright regions and decorated step edges. Such regions are assigned as Co islands. We estimated based on the XPS measurements that the Co coverage in the sample of Figure 6.1c is 5 to 6 times higher than the one in Figure 6.1d. From the STM measurements, this can not be clear due to the growth mechanism of the Co on Ag(111), which can grow as 3D islands [183]. We are interested in the coordination between TPyPPB molecules using Co adatoms to form 2D-MOFs. In this context, it is mandatory to keep two main aspects in mind: (1) the TPyPPB molecules must diffuse on the surface to react and (2) they need to find the Co adatoms before the Co islands formation. Regarding molecular deposition, we always ensure that the TPyPPB molecules are deposited in submonolayer coverages, typically < 0.3 ML. As discussed before, the Co islands are already formed in the deposition for 5 minutes using a low ion flux (2 nA). To obtain an extremely low coverage of Co, we performed the deposition keeping the same 2 nA flux but depositing the Co for 30 seconds only. We called this coverage an adatom regime, where no Co islands can be found on the Ag(111) surface. Unfortunately, at such low coverages, is impossible to detect the Co species by XPS measurements using conventional X-ray sources. To detect such low coverage it is mandatory to perform the measurements using synchrotron radiation [33].

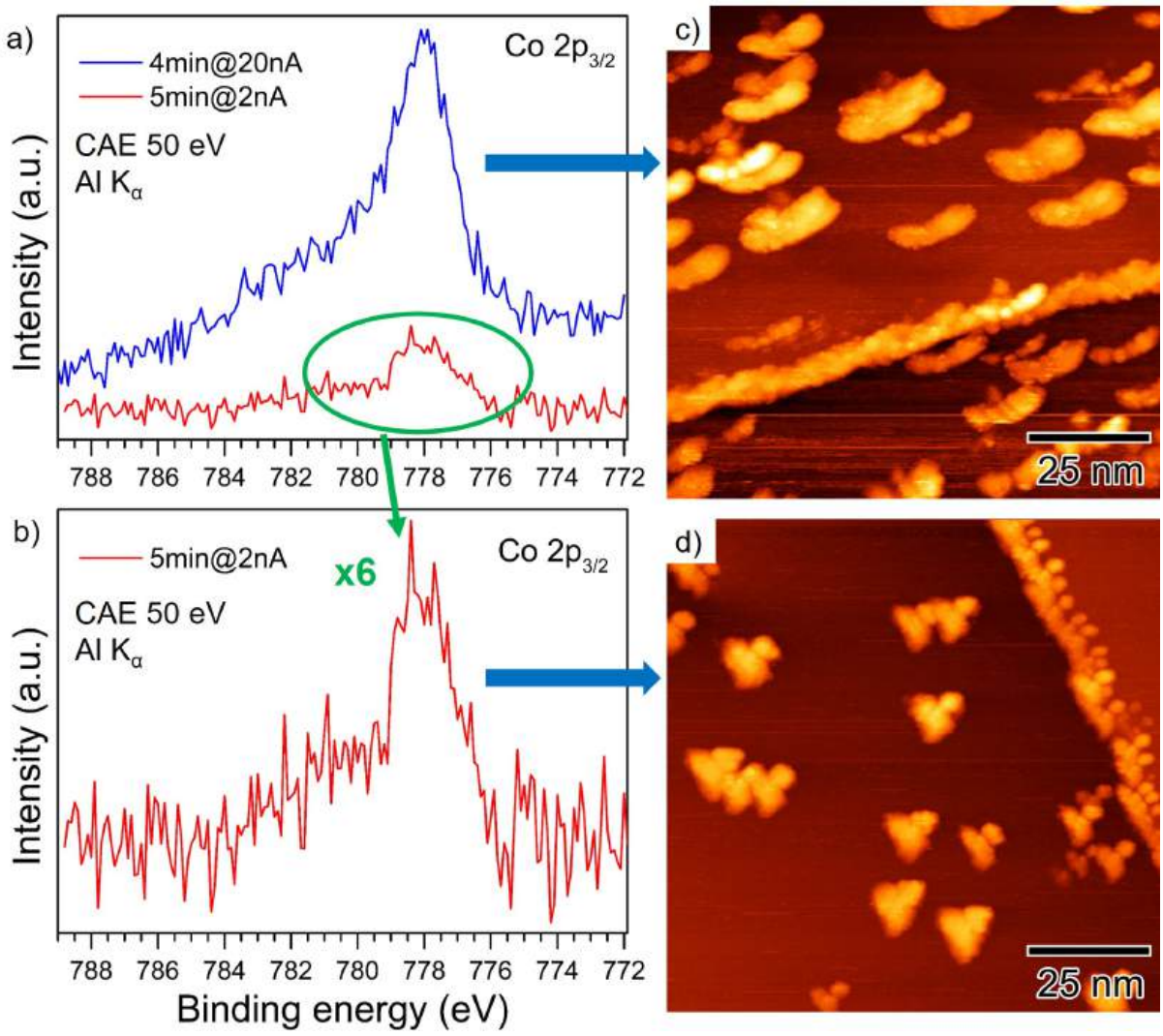

Figure 6.1: XPS spectrum at Co $2p_{3/2}$ core-level for a) high coverage (blue curve) and low Co dosage (red curve); b) Zoom-in of the XPS spectra for low Co coverage; STM image for the condition of c) high and d) low Co coverage on Ag(111). c) ($I_t = 200$ pA; $V_t = -0.7$ V); d) ($I_t = 200$ pA; $V_t = -0.7$ V).

The deposition of TPyPPB on the bare Ag(111) surface leads to the triangular packing formation, as shown in Chapter 5. In this condition, the molecules are interacting via N···H hydrogen bonds. In contrast as for Cu(111), the TPyPPB molecules do not coordinate with Ag adatoms. Recently, DFT calculations showed that the large energy separation between the 5s and the 4d atomic orbitals of Ag forbids the hybridization of the metal orbitals with the molecular orbitals of molecules containing N end groups [184]. Therefore, the Ag(111) substrate is a suitable platform for the construction of 2D-MOFs using extrinsic metal atoms. This allows us to explore a plethora of elements to tune the electronic and magnetic properties of the material.

After deposition at RT in submonolayer coverage, the TPyPPB molecules form the triangular packing (see Figure 5.2a in Chapter 5). The post-deposition of Co for 30 s leads to a phase transition, forming a complex tesselation structure, as shown in Figure 6.2a. In the adatom regime, there is no evidence of Co island formation. This more complex phase displays a rectangular symmetry, as evidenced in the fast Fourier transform (FFT) in the inset

of Figure 6.2a. The nanostructure formed extends over dozens of nanometers with the same symmetry.

Figure 6.2b, shows a high-resolution STM image where we can identify the periodicity of the nanostructure. This phase is described by a rectangular lattice with constants $a = (3.6 \pm 0.3)$ nm and $b = (4.8 \pm 0.3)$ nm. Moreover, the blue and purple ellipses in Figure 6.2b highlight the presence of protrusions in the regions between the TPyPPB molecules. In blue, the two protrusions are far apart from each other compared to the purple ones. We assigned these additional structures to Co species. Unfortunately, from STM images we can not conclude if these protrusions are single Co adatoms or a small cluster. Comparing the appearance of this appearance with the Cu-coordinated centers shown in Chapter 4, the Co adatoms appear brighter than the Cu. In fact, the Cu coordination centers are not visible in the STM images. The distinct appearance of Co compared to Cu can be assigned to their different electronic structure and/or oxidation state. The latter is defined by the coordination with the TPyPPB molecules, which for Cu is two- or three-fold while for Co is more complex since the molecules are not interacting head-on with each other. Despite the complex arrangement, the Co adatoms can form a spin lattice. The magnetic moments of the Co adatoms can interact with the substrate conduction electrons, forming a 2D Kondo lattice. The interaction between the metal centers can further lead to a Ruderman–Kittel–Kasuya–Yosida (RKKY) interaction [185, 186]. Another effect that changes the magnetic behavior of metals is the oxidation state [187]. To address such behaviors further measurements using low-temperature STM (LT-STM) and X-ray magnetic circular dichroism (XMCD) are necessary and it is not in the scope of this thesis.

Moreover, we can identify that the structure is composed of diamond-shaped pores. Inside the pores, we observed a distinct apparent height in the STM images, as highlighted by the green and blue arrows in Figure 6.2b. This blurred appearance is typically related to mobile species on the surface, especially for STM measurements at RT. We can identify two main different blurred regions in Figure 6.2b: (1) a donut-shaped (blue arrow) and (2) a uniformly bright region (green arrow). These different appearances could resemble the electronic surface states (SS) confinement in nanoporous networks at low temperatures [144]. Since our measurements are performed at RT, we do not expect to observe such behavior due to the thermal influence at such high temperatures. On the other hand, the surface has adsorbed species, more specifically adatoms (Ag and Co). Hence, the apparent height observed here is most likely related to the movement of confined adatoms. The different appearances can be assigned to a different occupation number of the pores. To demonstrate the last statement, further investigations using low-temperature STM and I(z) spectroscopy are needed.

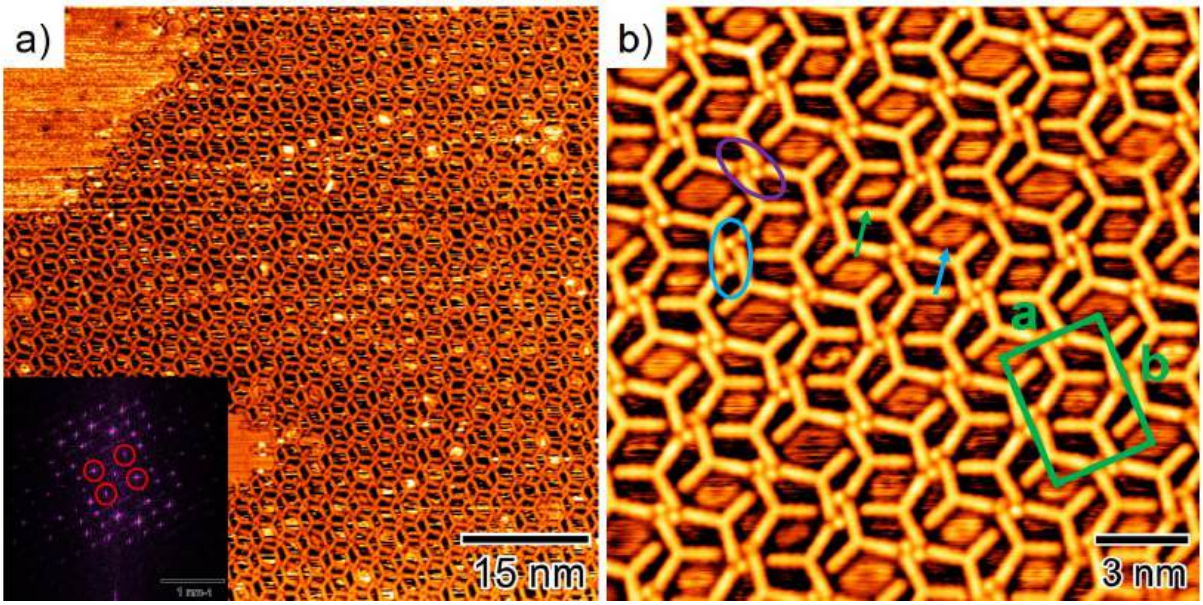

Figure 6.2: a) STM image of the porous network composed of TPyPPB molecules after Co deposition in adatom regime coverage. The inset image shows the respective FFT image with the high-symmetry points highlighted in red. ($I_t = 200$ pA; $V_t = -0.7$ V); b) STM high-resolution image of Co-coordinated nanostructure showing the lattice unit cell (green rectangle) and the Co adatoms (clusters) that stabilizes the structure (blue and purple ellipses). The green and blu arrow highlights the different apparent heights in the pores, assigned to mobile species. ($I_t = 200$ pA; $V_t = -0.7$ V).

The STM images in Figure 6.3a-c were acquired in sequence and with the same tunneling parameters to investigate the stability of the nanostructure formed. The green arrow highlights a common feature that appears in all images at the same location. In this case, it consists of four dark spots in a *L* shape, which is related to surface impurities (e.g. CO molecules). This guarantees that we are scanning the same area in all three images. From Figure 6.3a to b, the nanostructure moves from right to left and then back to right in Figure 6.3c. This suggests that for small islands, the nanostructure is not stable at RT. This can be related to a deficiency of Co adatoms on the surface, which is the key player in stabilizing the nanostructure.

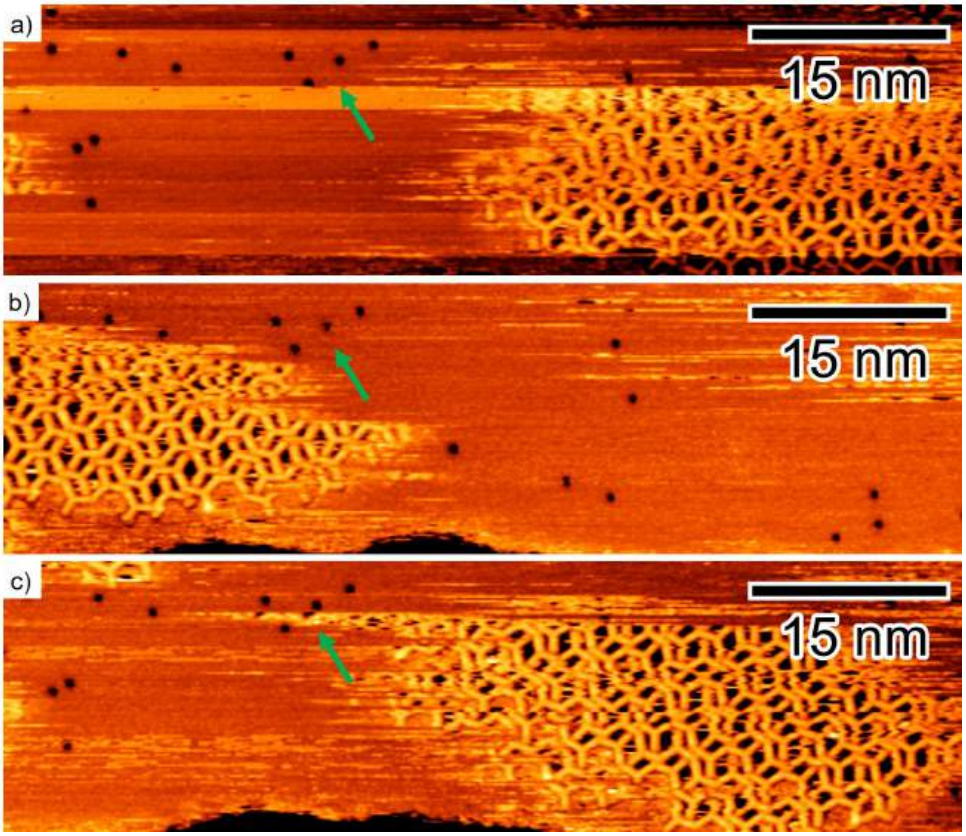

Figure 6.3: a-c) Sequential STM images showing the mobility of the Co-coordinated networks on the surface at RT. The time interval is Δt = 1m50s for each image. The green arrow highlights a distinct feature of the scanned region common to all images. (I_t = 200 pA; V_t = −0.7 V).

Conclusions

We successfully synthesized and characterized Co-coordinated supramolecular network using TPyPPB molecules on Ag(111). The nanostructure formed is highly dependent on the Co coverage, being formed only in the adatom regime. Moreover, the nanostructure is composed of a complex tesselation with the Co adatoms (or small clusters) in well-defined positions. This opens the possibilities to further explore the magnetic behavior of this 2D-MOF. The nanostructure grows in long-range domains, with a stable structure at RT. However, when in small domains (≥ 50 nm) we observed that the network is not stable at RT during the time-scale of the STM scan. Moreover, in the nanostructure pores, we identify bright regions that are assigned to confined species (small molecules, adatoms).

Chapter 7

On-Surface Synthesis of Nitrogen-Doped Porous Graphene Nanoribbons

In this chapter, we show the on-surface synthesis of nitrogen-doped porous armchair GNRs (N-GNRs) on Ag(110) using the Ullmann coupling reaction. This N-GNR was first synthesized recently on Ag(111) [96] using the 2,7,11,16-tetrabromotetrabenzo[a,c,h,j] phenazine (TBTBP) molecules. Motivated by this new find, our group started to explore the TBTBP molecular precursor on Cu(111) and Ag(100) [188]. In this case, the N-GNRs were successfully synthesized on both substrates. The results showed in this thesis consist of a follow-up investigation of the TBTBP molecules on a more open and anisotropic surface, Ag(110). The on-surface synthesis is highly dependent on the substrate orientation and reactivity, as shown in Chapter 2. Therefore, by combining the previous results on Cu(111) and Ag(100) with the results of this thesis on Ag(110), we show that the TBTBP precursor is a unique molecule, forming N-GNRs on all surfaces with the same features. The synthesis of the N-GNRs on Ag(110) was investigated using scanning tunneling microscopy combined with X-ray photoelectron spectroscopy. The TBTBP precursor is not commercially available and was synthesized in the group of Prof. Ronaldo Pilli at the Chemistry Institute (IQ) at the University of Campinas (UNICAMP).

In the previous works of our group on Cu(111) and Ag(100) [188], we observed that the TBTBP molecules deposited on both substrates at RT did not form any ordered nanostructure. On both surfaces the molecules are debrominated already at RT, forming stable C–M–C bonds (M = Cu, Ag). Moreover, on Cu(111) we also observed that adsorbing Br-functionalized porphyrins with the surface at RT or T > RT dramatically changes the molecular arrangement [102]. Motivated by our previous experience with brominated organic precursors, we did not investigate the adsorption of TBTBP molecules on Ag(110) held at RT during deposition. In our experiments, we systematically investigate the influence of the substrate temperature in the N-GNRs synthesis during the deposition as well as after annealings at 400, 450, 500, and 550 K. All samples were explored at submonolayer coverages to allow molecular diffusion. It is important to ensure that the molecules have enough space to interact with each other.

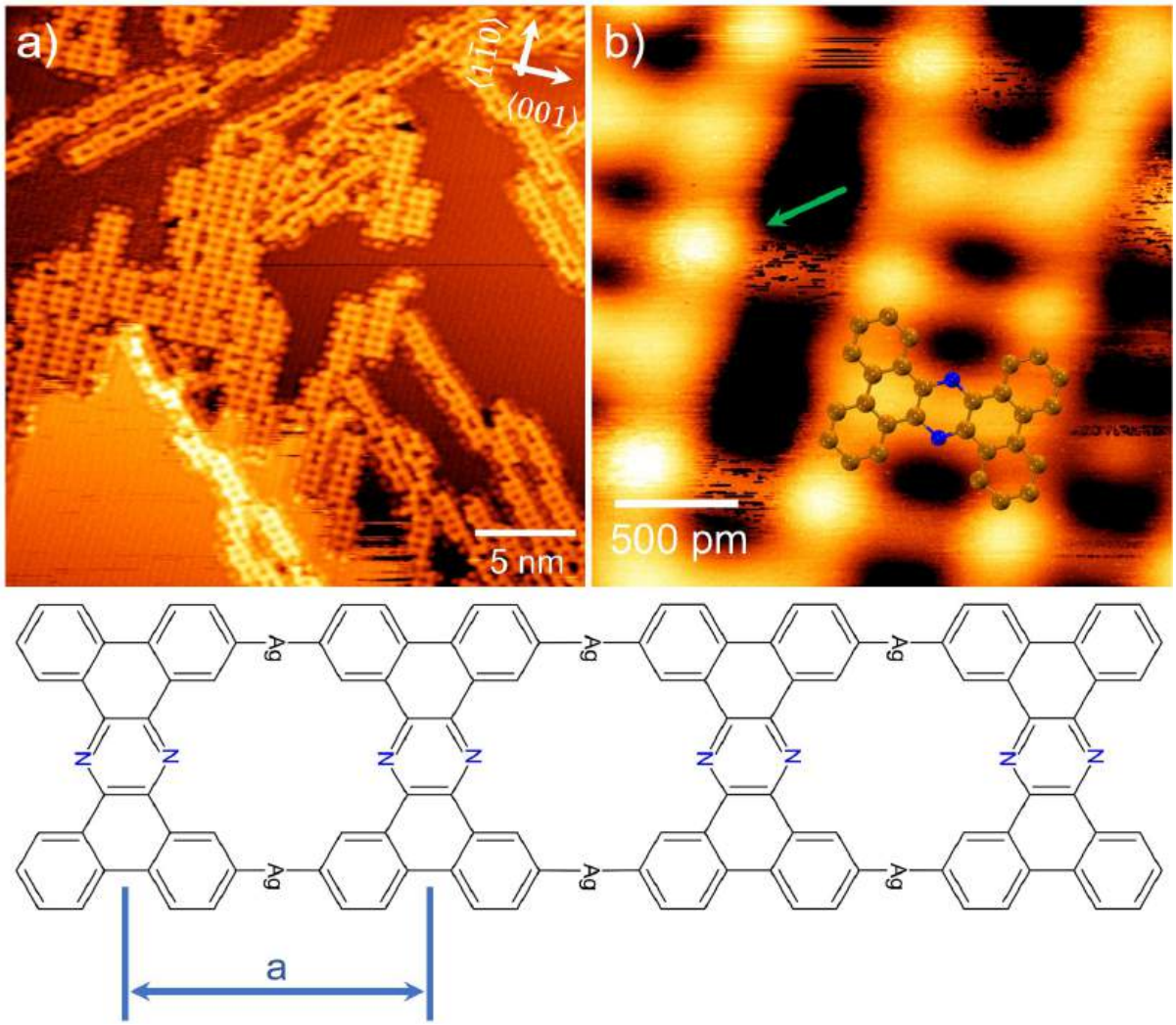

Figure 7.1: a) STM image of TBTBP molecules deposited on Ag(110) held at 400 K. The molecules form C–Ag–C chains. The black arrows at the top highlight the high-symmetry surface directions (I_t = 200 pA; V_t = −0.7 V); b) High-resolution STM image with superimposed TBTBP molecular model showing the Ag adatoms connecting the molecules (green arrow) (I_t = 200 pA; V_t = −0.7 V). At the bottom, the molecular model of the C–Ag–C chains with the intermolecular distance defined by a.

Deposition at 400 K leads to the debromination of the molecules followed by the

radical addition of the molecules forming 1D nanostructures, as shown in Figure 7.1. The dissociation of C–Br bonds on Ag(110) is reported at RT [189] so we expect that at 400 K full debromination take place. The TBTBP molecules form 1D organometallic chains coordinated by Ag adatoms, which are intrinsically on the surface. The high-resolution STM image in Figure 7.1b highlights the Ag adatoms (green arrow) coordinating the TBTBP molecules (superimposed model). The intermolecular distance in the chain is $a = (10.4 \pm 0.3)$ Å. From atomic resolution STM images of Ag(110), we can define the high-symmetry directions of the surface, represented by the black arrows at the top-right in Figure 7.1a. To investigate the orientation of the chains, we performed a statistical analysis of several STM images. After analyzing 247 chains we found that they are oriented along two main directions: along the $\langle\bar{1}10\rangle$ and rotated by $44 \pm 3°$ from it, as shown in Figure 7.2.

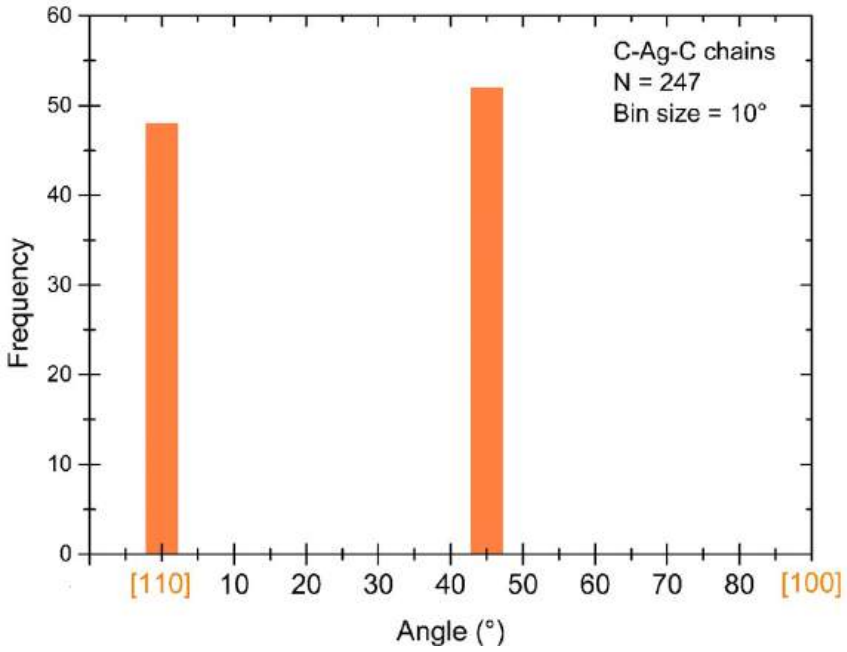

Figure 7.2: Histogram of the organometallic chain orientation

As discussed in Chapter 2, the organometallic species is an intermediate state of the Ullmann reaction. The reaction to form the N-GNRs is endothermic. Thus, we performed further annealings at 450 and 500 K for 10 minutes in the sample formed by the C–Ag–C chains (see Figure 7.1). For annealings at 450 K, we observed a change in the chain backbones, as highlighted by the blue arrows in Figure 7.3a and b. In Figure 7.3b we can distinguish two regions, a C–Ag–C chain (green arrow) and a bright region (blue arrow). The chain is evident due to the presence of the Ag adatoms (round protrusions) coordinating the molecules. On the other hand, in the region highlighted by the blue arrow, we can not identify any evidence of Ag-coordination. We assign this bright region to the molecules that are already forming N-GNR units, i.e., the final products of the Ullmann reaction. The change in their appearance in STM images is related to the planarization of the molecules after polymerization, in line with previous investigations [96, 188]. Thus, at 450 K the molecules are slowly forming the C–C bonding motifs. The chain orientation remains the same

as the sample prepared at 400 K, which is evident from Figure 7.3a, where we have both atomic and molecular resolution in the same image. Moreover, in the region between the molecular chains, the STM images revealed the presence of protrusions in a zigzag shape, as highlighted by the blue ellipse in Figure 7.3b. In the context of the Ullmann reaction, the halogen atoms typically remain on the surface after dissociation, and in the case of Br, the adatoms usually sit near the organic molecules [102, 190]. Therefore, we assigned the zigzag protrusions in Figure 7.3b to Br adatoms. The zigzag behavior was predicted from DFT calculations [188] but was first observed experimentally in this thesis. The distance between the Br adatoms along the chain (N-GNR) direction is (4.7 ± 0.4) Å. For Br adatoms, their energetically stable adsorption site is the bridge site as revealed by DFT calculations [188]. This explains the zigzag behavior observed in our STM images since the adatoms slightly change their positions to remain on the bridge site along the chain (N-GNR). The Br adatoms can potentially influence the formation of the N-GNRs. As observed, they remain in the regions along the molecular nanostructures. This can interfere in the formation of long-range domains, due to the interaction of the Br adatoms with the molecular vicinity. The influence of the halogen adatoms in the Ullmann reaction is one of the main challenges in on-surface synthesis nowadays. Typically, the nanostructures formed via the Ullmann reaction consist of small-range domains. Recently, an attempt to remove the residual Br adatoms of the on-surface synthesis was reported [191]. On this occasion, the authors used atomic hydrogen to remove Br adatoms from the surface. After the formation of the polymer, they heated the surface at a low temperature (373 K) in a flux of hydrogen, This procedure removes the residual Br adatoms from the surface keeping the nanostructure unaffected.

Further annealing at 500 K leads to the full conversion of the organometallic species into N-GNRs, as shown in Figure 7.3c. To gain further insight into the conversion reaction, we performed a systematic study as a function of annealing duration. We annealed the sample at 450 and 500 K in time steps ranging from 10 to 240 minutes, and counted the number of molecules in C–Ag–C and C–C motifs. Our starting pointing (t = 0 minute) was the sample prepared with the substrate held at 400 K, which consists of a sample containing only C–Ag–C species. Both samples were prepared using the almost same submonolayer coverage. For each sample (450 K and 500 K) 4500 - 5000 molecules were counted. The conversion rates of C–Ag–C into C–C for both temperatures are depicted in Figure 7.3d. In both cases, we can observe an expected exponential decay but with an interesting behavior. For 450 K (green triangles), the reaction stabilizes around 50 % after 60 minutes, while for 500 K (blue circles) at the same time, all molecules are forming C–C bond motifs. This suggests that the organometallic species are gradually converting into covalent ones [93]. This indicates that 450 K is the initial temperature for the conversion into covalent linkages.

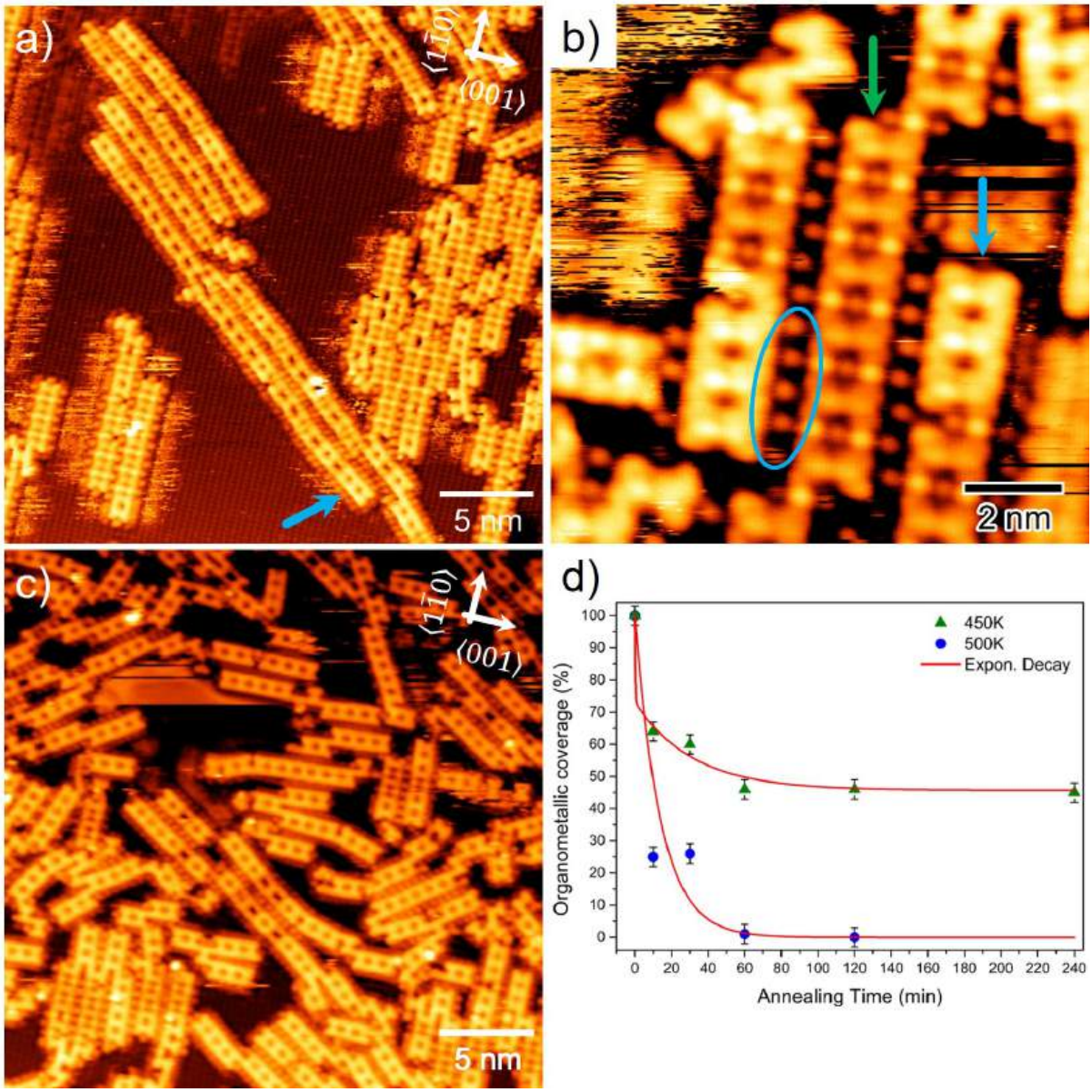

Figure 7.3: a) STM image of TBTBP molecules after annealing at 450 K for 10 minutes displaying the formation of N-GNR units (blue arrow) ($I_t = 200$ pA; $V_t = -0.7$ V); b) High-resolution STM image of C–Ag–C chains (green arrow) and N-GNR (blue arrow), showing their distinct apparent height. The blue ellipse highlights the Br adatoms ($I_t = 200$ pA; $V_t = -0.7$ V); c) STM image of TBTBP molecules annealed at 500 K for 10 minutes showing the formation of N-GNRs ($I_t = 200$ pA; $V_t = -0.7$ V); d) Statistical analysis of the conversion of C–Ag–C chains into N-GNRs as a function of annealing time at 450 K (green triangles) and 500 K (blue circles).

In order to obtain highly ordered N-GNRs, we further anneal the sample containing only C–Ag–C chains (see Figure 7.1) to 550 and 600 K for 20 minutes. For 550 K, the molecules polymerized forming short N-GNRs, mainly aligned along the ⟨100⟩ direction, as displayed in Figure 7.4a. As expected, no evidence of C–Ag–C chains was observed at this temperature. The N-GNRs display a unique morphology, with the molecules being connected by σ bonds with an inner pore containing a heteroatom doping with nitrogen, as shown in the molecular model in Figure 7.4. This gives this nanoribbon great potential in applications in nanoelectronics and gas sensing.

On the other hand, the annealing at 600 K dramatically changes the N-GNR length.

At this temperature, we observed an increase in the nanoribbon length. In addition, their orientation also changed, with the N-GNRs rotated by 55 ± 2° from the ⟨$\bar{1}$10⟩ direction, as shown in Figure 7.4b.

The intermolecular distance of the N-GNR is (8.5 ± 0.3) Å, in agreement with the N-GNRs obtained on Ag(111), Ag(100), and Cu(111) (see Table 7.1). The remarkable similarity of intermolecular distances shows the potential of TBTBP to be explored on a variety of substrates, independently of the surface orientation. The N-GNRs formed have a uniform shape with the N doping atoms at well-defined positions for all substrates in Table 7.1. They also display well-defined width (N = 7) with armchair edge terminations. In addition, Figure 7.4c, displays a high-resolution STM image with superimposed TBTBP molecular structure where we can distinguish the LDOS of the N atoms in the N-GNR. The difference in the contrast is due to the large electronegativity of N compared to C atoms.

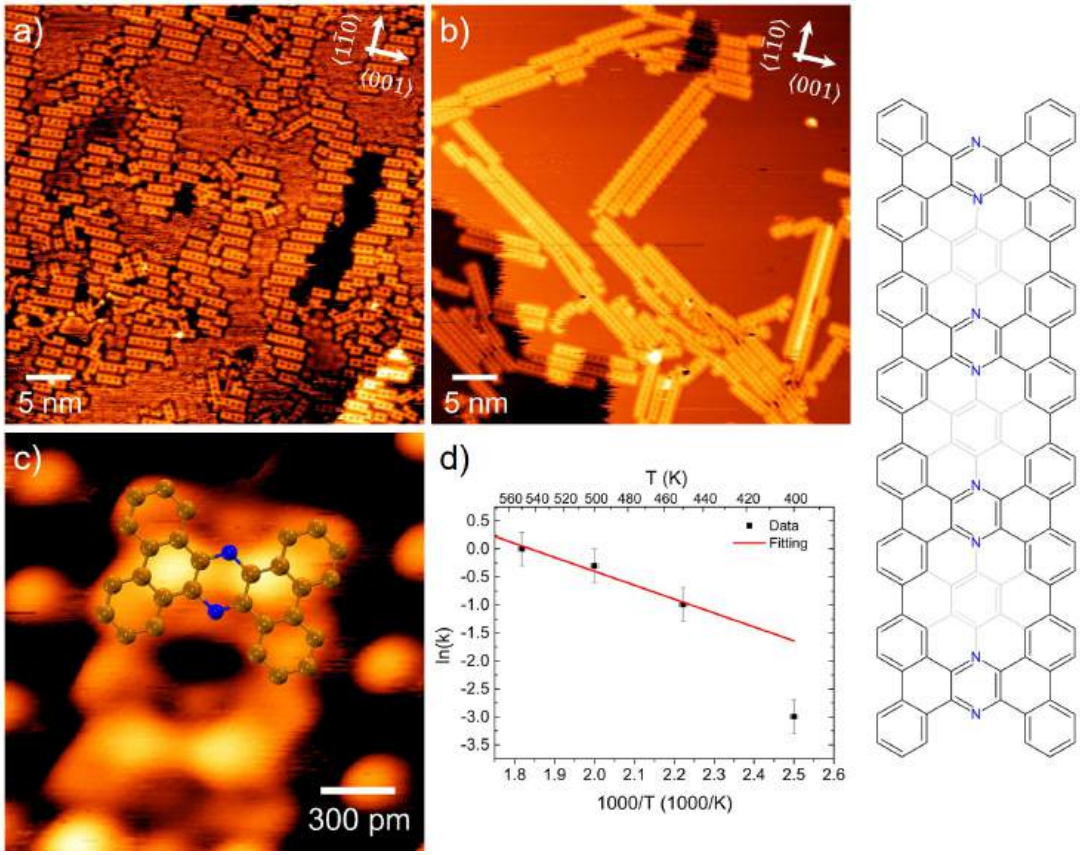

Figure 7.4: STM images of the TBTBP molecules annealed at a) 550 and b) 600 K for 20 minutes showing the formation of N-GNRs; c) High-resolution STM images with superimposed TBTBP molecular mode revealing the distinct LDOS at N positions; d) Arrhenius plot for the conversion reaction of organometallic into covalent species. On the right side, is the N-GNR molecule model. a) (I_t = 200 pA; V_t = −0.7 V); b) (I_t = 200 pA; V_t = −0.7 V); c) (I_t = 200 pA; V_t = −0.7 V).

An important aspect of reactions is their energy barriers. The STM allows us to experimentally estimate such energies, especially by employing the so-called Arrhenius plot [192–195]. In our case, we are interested in estimating the energy barrier for the reaction: C–Ag–C ⟶ C–C. Since the reaction is activated with the temperature we can employ

Table 7.1: Intermolecular distance of the N-GNR on the four different substrates

Substrate	Lattice parameter (a)
Ag(111)	(8.4) Å [96]
Ag(110)	(8.5 ± 0.3) Å
Ag(100)	(8.7 ± 0.2) Å [188]
Cu(111)	(8.5 ± 0.3) Å [188]

the Arrhenius equation $k = v\exp(-\frac{E_A}{k_B T})$, where v is a pre-factor, E_A is the activation energy for the reaction, k_B is the Boltzmann constant, and T the temperature. By analyzing several STM images in different regions we can count the number of C–Ag–C and C–C species for the samples at 400, 450, 500, and 550 K. Since the molecules rapidly convert in N-GNRs at 550 K, we did not consider the sample at 600 K, since all molecules are already converted. For each temperature, ≈1500 molecules were considered and then normalized by the total number of molecular units. At 400 K the reaction is slow, and we could not detect it from STM measurements. A similar behavior was reported for the Pd-catalyzed Ullmann reaction on Au(111) [196]. This slow conversion is due to the reversible character of the C–Ag–C bonds. Therefore, we ignored the samples at 400 K in the Arrhenius plot fitting. At T ≥ 450 K, the reaction is limited by the C–C bond formation as shown in Figure 7.3d. This limited rate combined with a rapid conversion, allows us to estimate the activation energy for the conversion of C–Ag–C into C–C bonds from the reaction kinetics. We estimated an activation energy for the reaction C–Ag–C ⟶ C–C of (0.21 ± 0.02) eV with a pre-factor of $(10^{5\pm1})$ s^{-1}.

We also investigate the adsorption of the TBTBP molecules on the Ag(110) substrate kept at 500 and 550 K during the molecular deposition. Figure 7.5a display the STM image after deposition at 500 K. At this temperature, we can identify both organometallic and covalent species on the sample. This suggests that the molecules form the N-GNRs already after deposition with more disordered motifs, highlighted in blue in Figure 7.5a. For deposition with the substrate held at 550 K, a different behavior was observed, as shown in Figure 7.5b. There is no evidence of C–Ag–C chains and only N-GNRs were observed. However, the deposition parameters of this sample were the same as the one prepared at 500 K (see Figure 7.5a). Interestingly, the molecular coverage in the STM images is strikingly different. The sample prepared at 550 K displays a very low coverage compared to the one prepared at 500 K. This suggests that 550 K is too high for the deposition and the TBTBP molecules do not stick on the surface at such high temperatures.

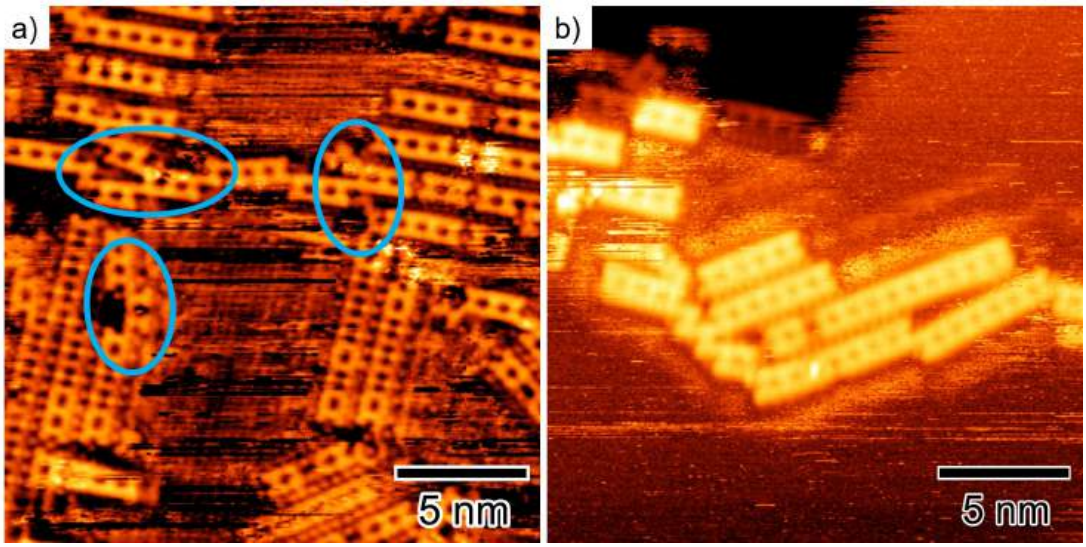

Figure 7.5: STM images of the TBTBP molecules deposited on Ag(110) held at a) 500 and b) 550 K during the molecular deposition. The blue ellipses highlight the formation of disordered structures. a) (I_t = 200 pA; V_t = −0.7 V); b) (I_t = 200 pA; V_t = −0.7 V).

Despite the differences in length and orientation shown here, the main characteristic of a GNR that dictates its electronic properties is its morphology. As discussed in Chapter 2, the width and the edge termination of the GNR determine the electronic structure as well as their doping. The influence of doping is not only related to which dopant is used but also its position in the GNR structure. Thus, for device applications based on GNRs, it is mandatory to synthesize a uniform material, especially regarding their width, edge termination, and the dopant atom and position.

Conclusions

Therefore, we addressed the behavior of TBTBP on a more open and anisotropic surface, Ag(110), compared to the previous results from the literature and our group. By systematic investigations as a function of annealing temperature, we could observe two phases of the N-GNRs: (1) short ribbons aligned along the high-symmetry surface directions and (2) longer nanoribbons rotated from the substrate directions. Moreover, from a statistical analysis, we estimated the reaction barrier for the formation of the N-GNRs, by using the Arrhenius equation approximations. Finally, the results on Ag(111) from the literature and on Ag(100) and Cu(111) from our group, demonstrated that the TBTBP molecules have great potential, since the N-GNRs formed have the same morphology independently of the Ag surface orientation.

Conclusions and outlook

In this thesis, we successfully demonstrated the on-surface synthesis of porous nanostructures stabilized with distinct intermolecular interactions on three different surfaces: Cu(111), Ag(111), and Ag(110). We focused on the design of nanoporous networks at atomic and molecular level control using nitrogen-functionalized (TPyPB and TPyPPB) and halogenated (TBTBP and Cl_2PhPt) molecular precursors. For the molecules containing N end groups, we investigated their interaction with metal (Cu, Co) and nonmetal (Cl) atoms. Depending on the interaction, several nanoporous architectures were obtained with unique morphologies. We also addressed the intermolecular interactions and their influence on stabilizing the nanostructures. By exploring the brominated precursor TBTBP, we synthesized a doped and porous graphene nanoribbon employing the C–C coupling through the surface-assisted Ullmann reaction. Our findings combined with previous results from our group, demonstrated the versatility of this precursor, forming the same structure in distinct metallic surfaces. The binary, XPS-STM, proved to be a powerful tool for synthesizing and characterizing low-dimensional quantum materials.

For TPyPB and TPyPPB molecules on Cu(111), we observed the formation of several nanoporous networks stabilized by Cu-coordination. We verified the coexistence of honeycomb, semi-regular, and square Cu-coordinated networks formed with TPyPB molecules at RT. Our DFT calculations demonstrated that the metal coordination occurs with a Cu adatom of the surface. Deposition of a similar molecule but with a slightly different size, TPyPPB, dramatically changes the nanostructures formed. At RT, the molecules form a vitreous-like phase, with no evidence of the structures formed with the smaller precursor. Upon heating, the TPyPPB molecules form different porous nanostructures depending on the temperature. At 400 K, extended domains of highly-ordered honeycomb nanostructure were formed while at 420 K we observed the coexistence of these honeycomb nanostructures with a more complex flower-like network. Finally, at 450 K, a denser Cu-coordinated structure is formed namely diamond-shaped, where the molecules display a non-periodic network.

In parallel, we explored the same TPyPPB molecules on Ag(111). We observed that in this case, the molecules do not coordinate with the Ag adatoms. Instead, a porous self-assembled monolayer, namely triangular packing, stabilized by hydrogen bonds is formed. To gain further insight into the adatom-mediated synthesis, we performed the deposition of extrinsic atoms. First, we delivered Cl adatoms on Ag(111) using a second molecular precursor: Cl_2PhPt. Upon heating the precursors dehalogenates leaving Cl adatoms on the surface. Post-deposition of TPyPPB molecules revealed a dramatic phase transition

of the triangular packing to a so-called inverted packing. This new phase extends over hundreds of nanometers with low-defect density. Our STM measurements supported by DFT calculations revealed that the stabilization of this structure is due to the Cl adatoms interacting with the hydrogen atoms of TPyPPB molecules. The deposition of TPyPPB and Co atoms on Ag(111) leads to a complex nanoporous network formation. From our STM measurements, we suggest that the stabilization of the structure is due to a Co-coordination with the N end groups of TPyPPB molecules.

Finally, we explored the TBTBP precursor on Ag(110) to synthesize a 7-AGNR with a particular morphology. The ribbon presents nitrogen heteroatom doping in the inner part of the structure. In addition, the GNR also presents pores, due to the design of the molecular precursor used. The synthesis consists of the surface-assisted Ullmann coupling reaction, where different structures were observed depending on the substrate temperature. Upon deposition at 400 K, the TBTBP molecules form organometallic chains coordinated by Ag adatoms. By performing further annealing at 450, 500, 550, and 600 K we followed the C–Ag–C $\longrightarrow$ C–C reaction. From an Arrhenius plot, we estimated the experimental energy barrier for the reaction. Moreover, our findings combined with previous results from our group revealed that this unique GNR can be obtained independently of the surface used.

Thus, the results presented in this thesis show the adatom-mediated synthesis of highly-ordered two-dimensional porous networks stabilized by distinct mechanisms. Depending on the adatom and the precursor size, we can control the nanostructure formed. Furthermore, the type of atom used also defines the network morphology. The Cl adatom deposition using an intermediate molecular precursor can pave the investigations on the role of Cl adatoms in different low-dimensional networks, so far not well explored in literature. A route for future works is to explore the influence of other nonmetal atoms (Br, I, Si, Ge) in the stabilization of supramolecular nanostructures. The on-surface synthesis using the Ullmann coupling reaction allowed the construction of doped and porous graphene nanoribbons so far inaccessible by other methods. More interesting, the N-GNR obtained, shows the potential to be synthesized on several substrates with the same morphology, a prerequisite for future applications in nanodevices.

Finally, the findings of this thesis contribute to understand the physical-chemical fundamental aspects of surface-assisted supramolecular synthesis of porous networks. Particularly, the fabrication of such nanostructures opens the possibilities of using such nanomaterials as ideal models for further fundamental explorations related to confinement and catalytic processes. The adatom-mediated route is one of the most exciting synthetic pathways. The coordination of single adatoms can be used to create single-atom catalysts (SACs) to explore chemical reaction in its more fundamental picture. We proposed that by exposing such metal-coordinated nanostructures to gas-phase molecules (CO, CO_2, C_4H_6) combined with temperature-programmed desorption (TPD) techniques, we can track the catalytic behavior of these nanoporous networks. Further exploration relies on the understanding of

the metal atom's electronic configuration influence in the formation of the 2D-MOFs with a systematic study using distinct *d* metals (Fe, Ru, Ni, Pd, Pt, Mn). Such investigation can shed light on the hybridization mechanism between the molecular orbitals with the atomic orbitals of the metals. For this, less reactive surface platforms are mandatory, such as h-BN and Gr, since there are no adatoms on the surface to interact with the molecular precursors. The TBTBP precursor proved to be a versatile building block, being explored on several metallic substrates to form porous and doped graphene nanoribbons. A natural follow-up investigation is to explore this synthesis on polycrystalline metal substrates and even on insulators, opening the possibility of fabricating electronic device prototypes.

Bibliography

[1] Panitz, J. A. Field-ion microscopy-a review of basic principles and selected applications. *Journal of Physics E: Scientific Instruments* **15**, 1281 (1982). URL https://dx.doi.org/10.1088/0022-3735/15/12/004.

[2] Binnig, G., Quate, C. F. & Gerber, C. Atomic Force Microscope. *Phys. Rev. Lett.* **56**, 930–933 (1986). URL https://link.aps.org/doi/10.1103/PhysRevLett.56.930.

[3] Herpich, M., Friedl, J. & Stimming, U. *Scanning Electrochemical Potential Microscopy (SECPM) and Electrochemical STM (EC-STM)*, 1–67 (Springer Berlin Heidelberg, Berlin, Heidelberg, 2015). URL https://doi.org/10.1007/978-3-662-44551-8_1.

[4] Furukawa, H., Cordova, K. E., O'Keeffe, M. & Yaghi, O. M. The Chemistry and Applications of Metal-Organic Frameworks. *Science* **341**, 1230444 (2013). URL https://www.science.org/doi/abs/10.1126/science.1230444.

[5] Crommie, M. F., Lutz, C. P. & Eigler, D. M. Confinement of Electrons to Quantum Corrals on a Metal Surface. *Science* **262**, 218–220 (1993). URL https://www.science.org/doi/abs/10.1126/science.262.5131.218.

[6] Petit, C. & Bandosz, T. J. Exploring the coordination chemistry of MOF–graphite oxide composites and their applications as adsorbents. *Dalton Trans.* **41**, 4027–4035 (2012). URL http://dx.doi.org/10.1039/C2DT12017H.

[7] Chakraborty, G., Park, I.-H., Medishetty, R. & Vittal, J. J. Two-Dimensional Metal-Organic Framework Materials: Synthesis, Structures, Properties and Applications. *Chemical Reviews* **121**, 3751–3891 (2021). URL https://doi.org/10.1021/acs.chemrev.0c01049.

[8] Houtsma, R. S. K., de la Rie, J. & Stöhr, M. Atomically precise graphene nanoribbons: interplay of structural and electronic properties. *Chem. Soc. Rev.* **50**, 6541–6568 (2021). URL http://dx.doi.org/10.1039/D0CS01541E.

[9] Zint, S. *et al.* Imaging Successive Intermediate States of the On-Surface Ullmann Reaction on Cu(111): Role of the Metal Coordination. *ACS Nano* **11**, 4183–4190 (2017). URL https://doi.org/10.1021/acsnano.7b01109.

[10] Dong, L., Gao, Z. A. & Lin, N. Self-assembly of metal–organic coordination structures on surfaces. *Progress in Surface Science* **91**, 101–135 (2016). URL http://dx.doi.org/10.1016/j.progsurf.2016.08.001.

[11] Sumida, K. *et al.* Carbon Dioxide Capture in Metal–Organic Frameworks. *Chemical Reviews* **112**, 724–781 (2012). URL https://doi.org/10.1021/cr2003272.

[12] Lee, J., Li, J. & Jagiello, J. Gas sorption properties of microporous metal organic frameworks. *Journal of Solid State Chemistry* **178**, 2527–2532 (2005). URL https://www.sciencedirect.com/science/article/pii/S0022459605003051.

[13] Uzun, A. & Keskin, S. Site characteristics in metal organic frameworks for gas adsorption. *Progress in Surface Science* **89**, 56–79 (2014). URL https://www.sciencedirect.com/science/article/pii/S0079681613000464.

[14] Tsai, H. *et al.* Bright and stable light-emitting diodes made with perovskite nanocrystals stabilized in metal–organic frameworks. *Nature Photonics* **15**, 843–849 (2021). URL https://doi.org/10.1038/s41566-021-00857-0.

[15] Gutiérrez, M. *et al.* New OLEDs Based on Zirconium Metal-Organic Framework. *Advanced Optical Materials* **6**, 1701060 (2018). URL https://onlinelibrary.wiley.com/doi/abs/10.1002/adom.201701060.

[16] Zhao, Y., Zeng, H., Zhu, X.-W., Lu, W. & Li, D. Metal–organic frameworks as photoluminescent biosensing platforms: mechanisms and applications. *Chem. Soc. Rev.* **50**, 4484–4513 (2021). URL http://dx.doi.org/10.1039/D0CS00955E.

[17] Dong, J., Zhao, D., Lu, Y. & Sun, W.-Y. Photoluminescent metal–organic frameworks and their application for sensing biomolecules. *J. Mater. Chem. A* **7**, 22744–22767 (2019). URL http://dx.doi.org/10.1039/C9TA07022B.

[18] Thorarinsdottir, A. E. & Harris, T. D. Metal–Organic Framework Magnets. *Chemical Reviews* **120**, 8716–8789 (2020). URL https://doi.org/10.1021/acs.chemrev.9b00666.

[19] Mínguez Espallargas, G. & Coronado, E. Magnetic functionalities in MOFs: from the framework to the pore. *Chem. Soc. Rev.* **47**, 533–557 (2018). URL http://dx.doi.org/10.1039/C7CS00653E.

[20] Pascanu, V., González Miera, G., Inge, A. K. & Martín-Matute, B. Metal–Organic Frameworks as Catalysts for Organic Synthesis: A Critical Perspective. *Journal of the American Chemical Society* **141**, 7223–7234 (2019). URL https://doi.org/10.1021/jacs.9b00733.

[21] Bavykina, A. *et al.* Metal–Organic Frameworks in Heterogeneous Catalysis: Recent Progress, New Trends, and Future Perspectives. *Chemical Reviews* **120**, 8468–8535 (2020). URL https://doi.org/10.1021/acs.chemrev.9b00685.

[22] Yang, J. *et al.* Recent advances in nanosized metal organic frameworks for drug delivery and tumor therapy. *RSC Adv.* **11**, 3241–3263 (2021). URL http://dx.doi.org/10.1039/D0RA09878G.

[23] Lawson, H. D., Walton, S. P. & Chan, C. Metal–Organic Frameworks for Drug Delivery: A Design Perspective. *ACS Applied Materials & Interfaces* **13**, 7004–7020 (2021). URL https://doi.org/10.1021/acsami.1c01089.

[24] Wang, H.-S., Wang, Y.-H. & Ding, Y. Development of biological metal–organic frameworks designed for biomedical applications: from bio-sensing/bio-imaging to disease treatment. *Nanoscale Adv.* **2**, 3788–3797 (2020). URL http://dx.doi.org/10.1039/D0NA00557F.

[25] de Campos Ferreira, R. C. *et al.* Supramolecular Ordering and Reactions of a Chlorophenyl Porphyrin on Ag(111). *J. Phys. Chem. C* **124**, 14220–14228 (2020). URL https://doi.org/10.1021/acs.jpcc.0c02953.

[26] Böhringer, M. *et al.* Two-Dimensional Self-Assembly of Supramolecular Clusters and Chains. *Phys. Rev. Lett.* **83**, 324–327 (1999). URL https://link.aps.org/doi/10.1103/PhysRevLett.83.324.

[27] Yokoyama, T., Yokoyama, S., Kamikado, T., Okuno, Y. & Mashiko, S. Selective assembly on a surface of supramolecular aggregates with controlled size and shape. *Nature* **413**, 619–621 (2001). URL https://doi.org/10.1038/35098059.

[28] Steiner, C. *et al.* Hierarchical on-surface synthesis and electronic structure of carbonyl-functionalized one- and two-dimensional covalent nanoarchitectures. *Nature Communications* **8**, 14765 (2017). URL https://doi.org/10.1038/ncomms14765.

[29] Shi, Z. *et al.* Thermodynamics and Selectivity of Two-Dimensional Metallo-supramolecular Self-Assembly Resolved at Molecular Scale. *J. Am. Chem. Soc.* **133**, 6150–6153 (2011). URL https://doi.org/10.1021/ja2010434.

[30] Song, Y. *et al.* Self-Assembly and Local Manipulation of Au-Pyridyl Coordination Networks on Metal Surfaces. *ChemPhysChem* **18**, 2088–2093 (2017). URL https://chemistry-europe.onlinelibrary.wiley.com/doi/abs/10.1002/cphc.201700439.

[31] Ceccatto dos Santos, A. *et al.* Cyano-Functionalized Porphyrins on Cu(111) from One-Dimensional Wires to Two-Dimensional Molecular Frameworks: On the Role of Co-Deposited Metal Atoms. *Chem. Mater.* **32**, 2114–2122 (2020). URL https://doi.org/10.1021/acs.chemmater.9b05256.

[32] Matena, M. *et al.* On-surface synthesis of a two-dimensional porous coordination network: Unraveling adsorbate interactions. *Phys. Rev. B* **90**, 125408 (2014). URL https://link.aps.org/doi/10.1103/PhysRevB.90.125408.

[33] Sun, Q., Zhang, C., Cai, L., Tan, Q. & Xu, W. Oxygen-induced self-assembly of quaterphenyl molecules on metal surfaces. *Chem. Commun.* **50**, 12112–12115 (2014). URL http://dx.doi.org/10.1039/C4CC05235H.

[34] Ding, Z., Wang, S., Yan, S., Zeng, Y.-J. & Wang, D.-H. Nano-SH-MOF@Self-Assembling Hollow Spherical g-C3N4 Heterojunction for Visible-Light Photocatalytic Nitrogen Fixation. *ChemCatChem* **15**, e202201605 (2023). URL https://chemistry-europe.onlinelibrary.wiley.com/doi/abs/10.1002/cctc.202201605.

[35] Piquero-Zulaica, I. *et al.* Surface state tunable energy and mass renormalization from homothetic quantum dot arrays. *Nanoscale* **11**, 23132–23138 (2019). URL http://dx.doi.org/10.1039/C9NR07365E.

[36] Baker Cortés, B. D., Schmidt, N., Enache, M. & Stöhr, M. Comparing Cyanophenyl and Pyridyl Ligands in the Formation of Porphyrin-Based Metal–Organic Coordination Networks. *The Journal of Physical Chemistry C* **125**, 24557–24567 (2021). URL https://doi.org/10.1021/acs.jpcc.1c05360.

[37] Li, Y. *et al.* Coordination and Metalation Bifunctionality of Cu with 5,10,15,20-Tetra(4-pyridyl)porphyrin: Toward a Mixed-Valence Two-Dimensional Coordination Network. *Journal of the American Chemical Society* **134**, 6401–6408 (2012). URL https://doi.org/10.1021/ja300593w.

[38] Klappenberger, F. *et al.* Dichotomous Array of Chiral Quantum Corrals by a Self-Assembled Nanoporous Kagomé Network. *Nano Letters* **9**, 3509–3514 (2009). URL https://doi.org/10.1021/nl901700b.

[39] Telychko, M. *et al.* Ultrahigh-yield on-surface synthesis and assembly of circumcoronene into a chiral electronic Kagome-honeycomb lattice. *Science Advances* **7**, eabf0269 (2021). URL https://www.science.org/doi/abs/10.1126/sciadv.abf0269.

[40] Crasto de Lima, F., Ferreira, G. J. & Miwa, R. H. Topological flat band, Dirac fermions and quantum spin Hall phase in 2D Archimedean lattices. *Phys. Chem. Chem. Phys.* **21**, 22344–22350 (2019). URL http://dx.doi.org/10.1039/C9CP04760C.

[41] Piquero-Zulaica, I. *et al.* Engineering quantum states and electronic landscapes through surface molecular nanoarchitectures. *Rev. Mod. Phys.* **94**, 045008 (2022). URL https://link.aps.org/doi/10.1103/RevModPhys.94.045008.

[42] Dubois, M.-A. *et al.* Influence of Cu adatoms on the molecular assembly of 4,4-bipyridine on Cu(111). *Phys. Chem. Chem. Phys.* **20**, 15350–15357 (2018). URL http://dx.doi.org/10.1039/C8CP01184B.

[43] Kühne, D. *et al.* High-Quality 2D MetalOrganic Coordination Network Providing Giant Cavities within Mesoscale Domains. *Journal of the American Chemical Society* **131**, 3881–3883 (2009). URL https://doi.org/10.1021/ja809946z.

[44] Fan, Q. *et al.* Confined Synthesis of Organometallic Chains and Macrocycles by Cu–O Surface Templating. *ACS Nano* **10**, 3747–3754 (2016). URL https://doi.org/10.1021/acsnano.6b00366.

[45] Bischoff, F. *et al.* Tailoring Large Pores of Porphyrin Networks on Ag(111) by Metal–Organic Coordination. *Chemistry – A European Journal* **22**, 15298–15306 (2016). URL https://doi.org/10.1002/chem.201602154.

[46] Baklanov, A. *et al.* On-Surface Synthesis of Nonmetal Porphyrins. *J. Am. Chem. Soc.* **142**, 1871–1881 (2020). URL https://doi.org/10.1021/jacs.9b10711.

[47] Faraggi, M. N. *et al.* Bonding and Charge Transfer in Metal–Organic Coordination Networks on Au(111) with Strong Acceptor Molecules. *J. Phys. Chem. C* **116**, 24558–24565 (2012). URL https://doi.org/10.1021/jp306780n.

[48] Niu, T. *et al.* Halogen-Adatom Mediated Phase Transition of Two-Dimensional Molecular Self-Assembly on a Metal Surface. *Langmuir* **34**, 553–560 (2018). URL https://doi.org/10.1021/acs.langmuir.7b03796.

[49] Liu, J. *et al.* Bromine adatom promoted C–H bond activation in terminal alkynes at room temperature on Ag(111). *Phys. Chem. Chem. Phys.* **20**, 11081–11088 (2018). URL http://dx.doi.org/10.1039/C7CP07972A.

[50] Lu, J. *et al.* Construction of Two-Dimensional Chiral Networks through Atomic Bromine on Surfaces. *J. Phys. Chem. Lett.* **8**, 326–331 (2017). URL https://doi.org/10.1021/acs.jpclett.6b02680.

[51] Novoselov, K. S. *et al.* Electric Field Effect in Atomically Thin Carbon Films. *Science* **306**, 666–669 (2004). URL https://www.science.org/doi/abs/10.1126/science.1102896.

[52] Bena, C. & Montambaux, G. Remarks on the tight-binding model of graphene. *New Journal of Physics* **11**, 095003 (2009). URL https://dx.doi.org/10.1088/1367-2630/11/9/095003.

[53] Castro Neto, A. H., Guinea, F., Peres, N. M. R., Novoselov, K. S. & Geim, A. K. The electronic properties of graphene. *Rev. Mod. Phys.* **81**, 109–162 (2009). URL https://link.aps.org/doi/10.1103/RevModPhys.81.109.

[54] Herrera-Reinoza, N., dos Santos, A. C., de Lima, L. H., Landers, R. & de Siervo, A. Atomically Precise Bottom-Up Synthesis of h-BNC: Graphene Doped with h-BN Nanoclusters. *Chemistry of Materials* **33**, 2871–2882 (2021). URL https://doi.org/10.1021/acs.chemmater.1c00081.

[55] Villarreal, R. *et al.* Achieving High Substitutional Incorporation in Mn-Doped Graphene. *ACS Nano* **18**, 17815–17825 (2024). URL https://doi.org/10.1021/acsnano.4c03475.

[56] Mathkar, A. *et al.* Controlled, Stepwise Reduction and Band Gap Manipulation of Graphene Oxide. *The Journal of Physical Chemistry Letters* **3**, 986–991 (2012). URL https://doi.org/10.1021/jz300096t.

[57] Shen, Y. *et al.* Evolution of the band-gap and optical properties of graphene oxide with controllable reduction level. *Carbon* **62**, 157–164 (2013). URL https://www.sciencedirect.com/science/article/pii/S0008622313005009.

[58] Xu, X. *et al.* Interfacial engineering in graphene bandgap. *Chem. Soc. Rev.* **47**, 3059–3099 (2018). URL http://dx.doi.org/10.1039/C7CS00836H.

[59] Warmuth, J. *et al.* Band-gap engineering by Bi intercalation of graphene on Ir(111). *Phys. Rev. B* **93**, 165437 (2016). URL https://link.aps.org/doi/10.1103/PhysRevB.93.165437.

[60] Jørgensen, J. H. *et al.* Symmetry-Driven Band Gap Engineering in Hydrogen Functionalized Graphene. *ACS Nano* **10**, 10798–10807 (2016). URL https://doi.org/10.1021/acsnano.6b04671.

[61] Zhang, H. *et al.* Aryl Functionalization as a Route to Band Gap Engineering in Single Layer Graphene Devices. *Nano Letters* **11**, 4047–4051 (2011). URL https://doi.org/10.1021/nl200803q.

[62] Cai, J. *et al.* Atomically precise bottom-up fabrication of graphene nanoribbons. *Nature* **466**, 470–473 (2010). URL https://doi.org/10.1038/nature09211.

[63] Zheng, H., Wang, Z. F., Luo, T., Shi, Q. W. & Chen, J. Analytical study of electronic structure in armchair graphene nanoribbons. *Phys. Rev. B* **75**, 165414 (2007). URL https://link.aps.org/doi/10.1103/PhysRevB.75.165414.

[64] Ruffieux, S., Pascaland Wang *et al.* On-surface synthesis of graphene nanoribbons with zigzag edge topology. *Nature* **531**, 489–492 (2016). URL https://doi.org/10.1038/nature17151.

[65] Teeter, J. D. *et al.* On-Surface Synthesis and Spectroscopic Characterization of Laterally Extended Chevron Graphene Nanoribbons. *ChemPhysChem* **20**, 2281–2285 (2019). URL https://chemistry-europe.onlinelibrary.wiley.com/doi/abs/10.1002/cphc.201900445.

[66] Han, P. *et al.* Bottom-Up Graphene-Nanoribbon Fabrication Reveals Chiral Edges and Enantioselectivity. *ACS Nano* **8**, 9181–9187 (2014). URL https://doi.org/10.1021/nn5028642.

[67] Son, Y.-W., Cohen, M. L. & Louie, S. G. Energy Gaps in Graphene Nanoribbons. *Phys. Rev. Lett.* **97**, 216803 (2006). URL https://link.aps.org/doi/10.1103/PhysRevLett.97.216803.

[68] Nakada, K., Fujita, M., Dresselhaus, G. & Dresselhaus, M. S. Edge state in graphene ribbons: Nanometer size effect and edge shape dependence. *Phys. Rev. B* **54**, 17954–17961 (1996). URL https://link.aps.org/doi/10.1103/PhysRevB.54.17954.

[69] Fujita, M., Wakabayashi, K., Nakada, K. & Kusakabe, K. Peculiar Localized State at Zigzag Graphite Edge. *Journal of the Physical Society of Japan* **65**, 1920–1923 (1996). URL https://doi.org/10.1143/JPSJ.65.1920.

[70] Li, J. *et al.* Topological phase transition in chiral graphene nanoribbons: from edge bands to end states. *Nature Communications* **12**, 5538 (2021). URL https://doi.org/10.1038/s41467-021-25688-z.

[71] Lee, Y.-L., Zhao, F., Cao, T., Ihm, J. & Louie, S. G. Topological Phases in Cove-Edged and Chevron Graphene Nanoribbons: Geometric Structures, Z2 Invariants, and Junction States. *Nano Letters* **18**, 7247–7253 (2018). URL https://doi.org/10.1021/acs.nanolett.8b03416.

[72] Aprojanz, J. *et al.* Ballistic tracks in graphene nanoribbons. *Nature Communications* **9**, 4426 (2018). URL https://doi.org/10.1038/s41467-018-06940-5.

[73] Baringhaus, J. *et al.* Exceptional ballistic transport in epitaxial graphene nanoribbons. *Nature* **506**, 349–354 (2014). URL https://doi.org/10.1038/nature12952.

[74] Zhou, X. & Yu, G. Modified Engineering of Graphene Nanoribbons Prepared via On-Surface Synthesis. *Advanced Materials* **32**, 1905957 (2020). URL https://onlinelibrary.wiley.com/doi/abs/10.1002/adma.201905957.

[75] Wen, E. C. H. *et al.* Fermi-Level Engineering of Nitrogen Core-Doped Armchair Graphene Nanoribbons. *Journal of the American Chemical Society* **145**, 19338–19346 (2023). URL https://doi.org/10.1021/jacs.3c05755.

[76] Fu, Y. *et al.* On-Surface Synthesis of NBN-Doped Zigzag-Edged Graphene Nanoribbons. *Angewandte Chemie International Edition* **59**, 8873–8879 (2020). URL https://onlinelibrary.wiley.com/doi/abs/10.1002/anie.202000488.

[77] Cloke, R. R. *et al.* Site-Specific Substitutional Boron Doping of Semiconducting Armchair Graphene Nanoribbons. *Journal of the American Chemical Society* **137**, 8872–8875 (2015). URL https://doi.org/10.1021/jacs.5b02523.

[78] Campbell, P. G., Marwitz, A. J. V. & Liu, S.-Y. Recent Advances in Azaborine Chemistry. *Angewandte Chemie International Edition* **51**, 6074–6092 (2012). URL https://onlinelibrary.wiley.com/doi/abs/10.1002/anie.201200063.

[79] Kawai, S. *et al.* Atomically controlled substitutional boron-doping of graphene nanoribbons. *Nature Communications* **6**, 8098 (2015). URL https://doi.org/10.1038/ncomms9098.

[80] Pedramrazi, Z. *et al.* Concentration Dependence of Dopant Electronic Structure in Bottom-up Graphene Nanoribbons. *Nano Letters* **18**, 3550–3556 (2018). URL https://doi.org/10.1021/acs.nanolett.8b00651.

[81] Tao, C. *et al.* Spatially resolving edge states of chiral graphene nanoribbons. *Nature Physics* **7**, 616–620 (2011). URL https://doi.org/10.1038/nphys1991.

[82] Xu, W. *et al.* Rapid Fabrication of Designable Large-Scale Aligned Graphene Nanoribbons by Electro-hydrodynamic Nanowire Lithography. *Advanced Materials* **26**, 3459–3464 (2014). URL https://onlinelibrary.wiley.com/doi/abs/10.1002/adma.201306081.

[83] Han, M. Y., özyilmaz, b., Zhang, Y. & Kim, P. Energy Band-Gap Engineering of Graphene Nanoribbons. *Phys. Rev. Lett.* **98**, 206805 (2007). URL https://link.aps.org/doi/10.1103/PhysRevLett.98.206805.

[84] Liu, L. *et al.* Nanosphere Lithography for the Fabrication of Ultranarrow Graphene Nanoribbons and On-Chip Bandgap Tuning of Graphene. *Advanced Materials* **23**, 1246–1251 (2011). URL https://onlinelibrary.wiley.com/doi/abs/10.1002/adma.201003847.

[85] Clair, S. & de Oteyza, D. G. Controlling a Chemical Coupling Reaction on a Surface: Tools and Strategies for On-Surface Synthesis. *Chemical Reviews* **119**, 4717–4776 (2019). URL https://doi.org/10.1021/acs.chemrev.8b00601.

[86] Song, S. *et al.* On-surface synthesis of graphene nanostructures with -magnetism. *Chem. Soc. Rev.* **50**, 3238–3262 (2021). URL http://dx.doi.org/10.1039/D0CS01060J.

[87] Pawlak, R. *et al.* On-Surface Synthesis of Nitrogen-Doped Kagome Graphene. *Angewandte Chemie International Edition* **60**, 8370–8375 (2021). URL https://onlinelibrary.wiley.com/doi/abs/10.1002/anie.202016469.

[88] Mateo, L. M. *et al.* On-Surface Synthesis and Characterization of Triply Fused Porphyrin–Graphene Nanoribbon Hybrids. *Angewandte Chemie International Edition* **59**, 1334–1339 (2020). URL https://onlinelibrary.wiley.com/doi/abs/10.1002/anie.201913024.

[89] Lackinger, M. Surface-assisted Ullmann coupling. *Chem. Commun.* **53**, 7872–7885 (2017). URL http://dx.doi.org/10.1039/C7CC03402D.

[90] Dong, L., Liu, P. N. & Lin, N. Surface-Activated Coupling Reactions Confined on a Surface. *Accounts of Chemical Research* **48**, 2765–2774 (2015). URL https://doi.org/10.1021/acs.accounts.5b00160.

[91] Björk, J., Hanke, F. & Stafström, S. Mechanisms of Halogen-Based Covalent Self-Assembly on Metal Surfaces. *J. Am. Chem. Soc.* **135**, 5768–5775 (2013). URL https://doi.org/10.1021/ja400304b.

[92] Shi, K. J. *et al.* Ullmann Reaction of Aryl Chlorides on Various Surfaces and the Application in Stepwise Growth of 2D Covalent Organic Frameworks. *Organic Letters* **18**, 1282–1285 (2016). URL https://doi.org/10.1021/acs.orglett.6b00172.

[93] Fritton, M. *et al.* The Role of Kinetics versus Thermodynamics in Surface-Assisted Ullmann Coupling on Gold and Silver Surfaces. *Journal of the American Chemical Society* **141**, 4824–4832 (2019). URL https://doi.org/10.1021/jacs.8b11473.

[94] Sun, K. *et al.* Low-Temperature Removal of Dissociated Bromine by Silicon Atoms for an On-Surface Ullmann Reaction. *The Journal of Physical Chemistry C* **124**, 19675–19680 (2020). URL https://doi.org/10.1021/acs.jpcc.0c06188.

[95] Chen, M. *et al.* Combined Photoemission and Scanning Tunneling Microscopy Study of the Surface-Assisted Ullmann Coupling Reaction. *The Journal of Physical Chemistry C* **118**, 6820–6830 (2014). URL https://doi.org/10.1021/jp4121468.

[96] Pawlak, R. *et al.* Bottom-up Synthesis of Nitrogen-Doped Porous Graphene Nanoribbons. *J. Am. Chem. Soc.* **142**, 12568–12573 (2020). URL https://doi.org/10.1021/jacs.0c03946.

[97] Simonov, K. A. *et al.* From Graphene Nanoribbons on Cu(111) to Nanographene on Cu(110): Critical Role of Substrate Structure in the Bottom-Up Fabrication Strategy. *ACS Nano* **9**, 8997–9011 (2015). URL https://doi.org/10.1021/acsnano.5b03280.

[98] Kimouche, A. *et al.* Ultra-narrow metallic armchair graphene nanoribbons. *Nature Communications* **6**, 10177 (2015). URL https://doi.org/10.1038/ncomms10177.

[99] Binnig, G., Rohrer, H., Gerber, C. & Weibel, E. Surface Studies by Scanning Tunneling Microscopy. *Phys. Rev. Lett.* **49**, 57–61 (1982). URL https://link.aps.org/doi/10.1103/PhysRevLett.49.57.

[100] Giessibl, F. J. The qPlus sensor, a powerful core for the atomic force microscope. *Review of Scientific Instruments* **90**, 011101 (2019). URL https://doi.org/10.1063/1.5052264.

[101] Herbschleb, C. T. *et al.* The Reactor STM: Atomically resolved scanning tunneling microscopy under high-pressure, high-temperature catalytic reaction conditions. *Review of Scientific Instruments* **85**, 083703 (2014). URL https://doi.org/10.1063/1.4891811.

[102] Ceccatto dos Santos, A., Herrera-Reinoza, N., Pérez Paz, A., Mowbray, D. J. & de Siervo, A. Reassessing the Adsorption Behavior and on-Surface Reactivity of a Brominated Porphyrin on Cu(111). *The Journal of Physical Chemistry C* **125**, 17164–17173 (2021). URL https://doi.org/10.1021/acs.jpcc.1c03346.

[103] Meusel, M. *et al.* Growth of Multilayers of Ionic Liquids on Au(111) Investigated by Atomic Force Microscopy in Ultrahigh Vacuum. *Langmuir* **36**, 13670–13681 (2020). URL https://doi.org/10.1021/acs.langmuir.0c02596.

[104] Nony, L. *et al.* Cu-TBPP and PTCDA molecules on insulating surfaces studied by ultra-high-vacuum non-contact AFM. *Nanotechnology* **15**, S91 (2004). URL https://dx.doi.org/10.1088/0957-4484/15/2/019.

[105] Vázquez de Parga, A. L. & Miranda, R. *Scanning Tunneling Spectroscopy*, 2313–2321 (Springer Netherlands, Dordrecht, 2012). URL https://doi.org/10.1007/978-90-481-9751-4_111.

[106] Krejčí, O., Hapala, P., Ondráček, M. & Jelínek, P. Principles and simulations of high-resolution STM imaging with a flexible tip apex. *Phys. Rev. B* **95**, 045407 (2017). URL https://link.aps.org/doi/10.1103/PhysRevB.95.045407.

[107] Gottlieb, A. D. & Wesoloski, L. Bardeen's tunnelling theory as applied to scanning tunnelling microscopy: a technical guide to the traditional interpretation. *Nanotechnology* **17**, R57 (2006). URL https://dx.doi.org/10.1088/0957-4484/17/8/R01.

[108] Tersoff, J. & Hamann, D. R. Theory and Application for the Scanning Tunneling Microscope. *Phys. Rev. Lett.* **50**, 1998–2001 (1983). URL https://link.aps.org/doi/10.1103/PhysRevLett.50.1998.

[109] Drakova, D. Theoretical modelling of scanning tunnelling microscopy, scanning tunnelling spectroscopy and atomic force microscopy. *Reports on Progress in Physics* **64**, 205 (2001). URL https://dx.doi.org/10.1088/0034-4885/64/2/202.

[110] Hüfner, S. *Core Levels and Final States*, 61–107 (Springer Berlin Heidelberg, Berlin, Heidelberg, 2003). URL https://doi.org/10.1007/978-3-662-09280-4_2.

[111] Osterwalder, J. *Electron Based Methods: 3.2.2 Photoelectron Spectroscopy and Diffraction*, chap. 3.2, 151–214 (John Wiley Sons, Ltd, 2013). URL https://onlinelibrary.wiley.com/doi/abs/10.1002/9783527680535.ch5.

[112] Hofmann, P. *Surface Physics: An Introduction* (self-published, 2016).

[113] Hercules, D. M. & Hercules, S. H. Analytical chemistry of surfaces. Part II. Electron spectroscopy. *Journal of Chemical Education* **61**, 483 (1984). URL https://doi.org/10.1021/ed061p483.

[114] Rosenthal, S. J., McBride, J., Pennycook, S. J. & Feldman, L. C. Synthesis, surface studies, composition and structural characterization of CdSe, core/shell and biologically active nanocrystals. *Surface Science Reports* **62**, 111–157 (2007). URL https://www.sciencedirect.com/science/article/pii/S0167572907000180.

[115] Somorjai, G. *Chemistry in Two Dimensions: Surfaces*. Cornell Paperbacks (Cornell University Press, 1981). URL https://books.google.com.br/books?id=VQ_wAAAAMAAJ.

[116] Nečas, D. & Klapetek, P. Gwyddion: an open-source software for SPM data analysis. *Cent. Eur. J. Phys.* **10**, 181–188 (2012). URL https://doi.org/10.2478/s11534-011-0096-2.

[117] Liu, W. *et al.* Two-Dimensional Polymer Synthesized via Solid-State Polymerization for High-Performance Supercapacitors. *ACS Nano* **12**, 852–860 (2018). URL https://doi.org/10.1021/acsnano.7b08354.

[118] Li, Z. *et al.* Intercalation Strategy in 2D Materials for Electronics and Optoelectronics. *Small Methods* **5**, 2100567 (2021). URL https://onlinelibrary.wiley.com/doi/abs/10.1002/smtd.202100567.

[119] Kim, T., Park, J. Y., Hwang, J., Seo, G. & Kim, Y. Supramolecular Two-Dimensional Systems and Their Biological Applications. *Adv. Mater.* **32**, 2002405 (2020). URL https://onlinelibrary.wiley.com/doi/abs/10.1002/adma.202002405.

[120] Grill, L. & Hecht, S. Covalent on-surface polymerization. *Nat. Chem.* **12**, 115–130 (2020). URL https://doi.org/10.1038/s41557-019-0392-9.

[121] Bouju, X., Mattioli, C., Franc, G., Pujol, A. & Gourdon, A. Bicomponent Supramolecular Architectures at the Vacuum–Solid Interface. *Chemical Reviews* **117**, 1407–1444 (2017). URL https://doi.org/10.1021/acs.chemrev.6b00389.

[122] Kocić, N. *et al.* Periodic Charging of Individual Molecules Coupled to the Motion of an Atomic Force Microscopy Tip. *Nano Lett.* **15**, 4406–4411 (2015). URL https://doi.org/10.1021/acs.nanolett.5b00711.

[123] Lehn, J.-M. Perspectives in Chemistry—Steps towards Complex Matter. *Angew. Chem. Int. Ed.* **52**, 2836–2850 (2013). URL https://onlinelibrary.wiley.com/doi/abs/10.1002/anie.201208397.

[124] Barth, J. V., Costantini, G. & Kern, K. Engineering atomic and molecular nanostructures at surfaces. *Nature* **437**, 671–679 (2005). URL https://doi.org/10.1038/nature04166.

[125] Destoop, I. *et al.* Solvent-Induced Homochirality in Surface-Confined Low-Density Nanoporous Molecular Networks. *J. Am. Chem. Soc.* **134**, 19568–19571 (2012). URL https://doi.org/10.1021/ja309673t.

[126] Viciano-Chumillas, M. *et al.* Metal–Organic Frameworks as Chemical Nanoreactors: Synthesis and Stabilization of Catalytically Active Metal Species in Confined Spaces. *Accounts of Chemical Research* **53**, 520–531 (2020). URL https://doi.org/10.1021/acs.accounts.9b00609.

[127] Wan, Y., Yang, H. & Zhao, D. "HostGuest" Chemistry in the Synthesis of Ordered Nonsiliceous Mesoporous Materials. *Accounts of Chemical Research* **39**, 423–432 (2006). URL https://doi.org/10.1021/ar050091a.

[128] Umbach, T. R. *et al.* Ferromagnetic Coupling of Mononuclear Fe Centers in a Self-Assembled Metal-Organic Network on Au(111). *Phys. Rev. Lett.* **109**, 267207 (2012). URL https://link.aps.org/doi/10.1103/PhysRevLett.109.267207.

[129] Wang, T. *et al.* Kinetic Strategies for the Formation of Graphyne Nanowires via Sonogashira Coupling on Ag(111). *J. Am. Chem. Soc.* **140**, 13421–13428 (2018). URL https://doi.org/10.1021/jacs.8b08477.

[130] Zhang, R., Lyu, G., Li, D. Y., Liu, P. N. & Lin, N. Template-controlled Sonogashira cross-coupling reactions on a Au(111) surface. *Chem. Commun.* **53**, 1731–1734 (2017). URL http://dx.doi.org/10.1039/C6CC10091K.

[131] Ciesielski, A. *et al.* Concentration-Dependent Supramolecular Engineering of Hydrogen-Bonded Nanostructures at Surfaces: Predicting Self-Assembly in 2D. *J. Am. Chem. Soc.* **135**, 6942–6950 (2013). URL https://doi.org/10.1021/ja4002025.

[132] Stepanow, S. *et al.* Surface-Assisted Assembly of 2D Metal–Organic Networks That Exhibit Unusual Threefold Coordination Symmetry. *Angew. Chem. Int. Ed.* **46**, 710–713 (2007). URL https://onlinelibrary.wiley.com/doi/abs/10.1002/anie.200603644.

[133] Lepper, M. *et al.* Controlling the Self-Metalation Rate of Tetraphenylporphyrins on Cu(111) via Cyano Functionalization. *Angew. Chem. Int. Ed.* **57**, 10074–10079 (2018). URL https://onlinelibrary.wiley.com/doi/abs/10.1002/anie.201803601.

[134] Gao, Z. *et al.* Design and Synthesis of a Single-Layer Ferromagnetic Metal-Organic Framework with Topological Nontrivial Gaps. *J. Phys. Chem. C* **124**, 38 (2020). URL https://pubs.acs.org/doi/full/10.1021/acs.jpcc.0c08140.

[135] Li, J. *et al.* Low-Dimensional Metal–Organic Coordination Structures on Graphene. *J. Phys. Chem. C* **123**, 12730–12735 (2019). URL https://doi.org/10.1021/acs.jpcc.9b00326.

[136] Nowakowska, S. *et al.* Configuring Electronic States in an Atomically Precise Array of Quantum Boxes. *Small* **12**, 3757–3763 (2016). URL https://onlinelibrary.wiley.com/doi/abs/10.1002/smll.201600915.

[137] Zhang, R. *et al.* Two-Dimensional Superlattices of Bi Nanoclusters Formed on a Au(111) Surface Using Porous Supramolecular Templates. *ACS Nano* **9**, 8547–8553 (2015). URL https://doi.org/10.1021/acsnano.5b03676.

[138] Pivetta, M., Pacchioni, G. E., Schlickum, U., Barth, J. V. & Brune, H. Formation of Fe Cluster Superlattice in a Metal-Organic Quantum-Box Network. *Phys. Rev. Lett.* **110**, 086102 (2013). URL https://link.aps.org/doi/10.1103/PhysRevLett.110.086102.

[139] Piquero-Zulaica, I. *et al.* Electron Transmission through Coordinating Atoms Embedded in Metal-Organic Nanoporous Networks. *Phys. Rev. Lett.* **123**, 266805 (2019). URL https://link.aps.org/doi/10.1103/PhysRevLett.123.266805.

[140] Huang, H., Shen, K., Chen, F. & Li, Y. Metal–Organic Frameworks as a Good Platform for the Fabrication of Single-Atom Catalysts. *ACS Catalysis* **10**, 6579–6586 (2020). URL https://doi.org/10.1021/acscatal.0c01459.

[141] Yan, L. *et al.* Self-assembly of a binodal metal–organic framework exhibiting a demi-regular lattice. *Faraday Discuss.* **204**, 111–121 (2017). URL http://dx.doi.org/10.1039/C7FD00088J.

[142] Kizilörenli, E. & Maden, F. Tessellation in Architecture from Past to Present. *IOP Conf. Ser.: Mater. Sci. Eng.* **1203**, 032062 (2021). URL https://dx.doi.org/10.1088/1757-899X/1203/3/032062.

[143] Wang, W. *et al.* Cooperative Modulation of Electronic Structures of Aromatic Molecules Coupled to Multiple Metal Contacts. *Phys. Rev. Lett.* **110**, 046802 (2013). URL https://link.aps.org/doi/10.1103/PhysRevLett.110.046802.

[144] Wang, S. *et al.* Tuning two-dimensional band structure of Cu(111) surface-state electrons that interplay with artificial supramolecular architectures. *Phys. Rev. B* **88**, 245430 (2013). URL https://link.aps.org/doi/10.1103/PhysRevB.88.245430.

[145] Liu, J. *et al.* Structural Transformation of Two-Dimensional Metal–Organic Coordination Networks Driven by Intrinsic In-Plane Compression. *J. Am. Chem. Soc.* **133**, 18760–18766 (2011). URL https://doi.org/10.1021/ja2056193.

[146] Classen, T. *et al.* Templated Growth of Metal–Organic Coordination Chains at Surfaces. *Angew. Chem. Int. Ed.* **44**, 6142–6145 (2005). URL https://onlinelibrary.wiley.com/doi/abs/10.1002/anie.200502007.

[147] Adhikari, R. *et al.* Formation of Highly Ordered Molecular Porous 2D Networks from Cyano-Functionalized Porphyrins on Cu(111). *Chem. - Eur. J.* **26**, 13408–13418 (2020). URL https://chemistry-europe.onlinelibrary.wiley.com/doi/abs/10.1002/chem.202001980.

[148] Kuliga, J. *et al.* Metalation of 2HTCNPP on Ag(111) with Zn: Evidence for the Sitting atop Complex at Room Temperature. *ChemPhysChem* **22**, 396–403 (2021). URL https://chemistry-europe.onlinelibrary.wiley.com/doi/abs/10.1002/cphc.202000883.

[149] Auwärter, W. *et al.* Self-assembly and conformation of tetrapyridyl-porphyrin molecules on Ag(111). *J. Chem. Phys.* **124**, 194708 (2006). URL https://doi.org/10.1063/1.2194541.

[150] Ren, J. *et al.* Chemistry of 4-[(4-bromophenyl)ethynyl]pyridine at metal surfaces studied by STM. *Chem. Commun.* **54**, 9305–9308 (2018). URL http://dx.doi.org/10.1039/C8CC03986K.

[151] Lichtenstein, L., Heyde, M. & Freund, H.-J. Atomic Arrangement in Two-Dimensional Silica: From Crystalline to Vitreous Structures. *J. Phys. Chem. C* **116**, 20426–20432 (2012). URL https://doi.org/10.1021/jp3062866.

[152] Farnell, D. J. J. *et al.* Interplay between lattice topology, frustration, and spin quantum number in quantum antiferromagnets on Archimedean lattices. *Phys. Rev. B* **98**, 224402 (2018). URL https://link.aps.org/doi/10.1103/PhysRevB.98.224402.

[153] Fadeeva, A. I., Gorbunov, V. A., Solovyeva, O. S., Stishenko, P. V. & Myshlyavtsev, A. V. Homologous Series of Flower Phases in Metal–Organic Networks on Au(111) Surface. *J. Phys. Chem. C* **124**, 11506–11515 (2020). URL https://doi.org/10.1021/acs.jpcc.0c02527.

[154] Liu, J. *et al.* Structural Transformation of Two-Dimensional MetalÀOrganic Coordination Networks Driven by Intrinsic In-Plane Compression. *J. Am. Chem. Soc* **133**, 34 (2011). URL https://pubs.acs.org/sharingguidelines.

[155] Schlickum, U. *et al.* Chiral Kagomé Lattice from Simple Ditopic Molecular Bricks. *J. Am. Chem. Soc.* **130**, 11778–11782 (2008). URL https://doi.org/10.1021/ja8028119.

[156] Kühne, D. *et al.* Self-Assembly of Nanoporous Chiral Networks with Varying Symmetry from Sexiphenyl-dicarbonitrile on Ag(111). *J. Phys. Chem. C* **113**, 17851–17859 (2009). URL https://doi.org/10.1021/jp9041217.

[157] Horcas, I. *et al.* WSXM: A software for scanning probe microscopy and a tool for nanotechnology. *Rev. Sci. Instrum.* **78**, 013705 (2007). URL https://doi.org/10.1063/1.2432410.

[158] Perdew, J. P., Burke, K. & Ernzerhof, M. Generalized Gradient Approximation Made Simple. *Phys. Rev. Lett.* **77**, 3865–3868 (1996). URL https://link.aps.org/doi/10.1103/PhysRevLett.77.3865.

[159] Grimme, S., Antony, J., Ehrlich, S. & Krieg, H. A consistent and accurate ab initio parametrization of density functional dispersion correction (DFT-D) for the 94 elements H-Pu. *J. Chem. Phys.* **132**, 154104 (2010). URL https://doi.org/10.1063/1.3382344.

[160] Kresse, G. & Joubert, D. From ultrasoft pseudopotentials to the projector augmented-wave method. *Phys. Rev. B* **59**, 1758–1775 (1999). URL https://link.aps.org/doi/10.1103/PhysRevB.59.1758.

[161] Mortensen, J. J., Hansen, L. B. & Jacobsen, K. W. Real-space grid implementation of the projector augmented wave method. *Phys. Rev. B* **71**, 035109 (2005). URL https://link.aps.org/doi/10.1103/PhysRevB.71.035109.

[162] Enkovaara, J. *et al.* Electronic structure calculations with GPAW: a real-space implementation of the projector augmented-wave method. *J. Phys.: Condens. Matter* **22**, 253202 (2010). URL https://doi.org/10.1088%2F0953-8984%2F22%2F25%2F253202.

[163] Larsen, A. H., Vanin, M., Mortensen, J. J., Thygesen, K. S. & Jacobsen, K. W. Localized Atomic Basis Set in the Projector Augmented Wave Method. *Phys. Rev. B: Condens. Matter Mater. Phys.* **80**, 195112 (2009). URL http://link.aps.org/doi/10.1103/PhysRevB.80.195112.

[164] Tersoff, J. & Hamann, D. R. Theory of the scanning tunneling microscope. *Phys. Rev. B* **31**, 805–813 (1985). URL https://link.aps.org/doi/10.1103/PhysRevB.31.805.

[165] Larsen, A. H. *et al.* The atomic simulation environment—a Python library for working with atoms. *J. Phys.: Condens. Matter* **29**, 273002 (2017). URL https://doi.org/10.1088%2F1361-648x%2Faa680e.

[166] Goronzy, D. P. *et al.* Supramolecular Assemblies on Surfaces: Nanopatterning, Functionality, and Reactivity. *ACS Nano* **12**, 7445–7481 (2018). URL https://doi.org/10.1021/acsnano.8b03513.

[167] Gröning, O. *et al.* Engineering of robust topological quantum phases in graphene nanoribbons. *Nature* **560**, 209–213 (2018). URL https://doi.org/10.1038/s41586-018-0375-9.

[168] Ceccatto, A. *et al.* Engineering large nanoporous networks with size and shape selected by appropriate precursors. *Carbon* **221**, 118945 (2024). URL https://www.sciencedirect.com/science/article/pii/S0008622324001647.

[169] El Abbassi, M. *et al.* Controlled Quantum Dot Formation in Atomically Engineered Graphene Nanoribbon Field-Effect Transistors. *ACS Nano* **14**, 5754–5762 (2020). URL https://doi.org/10.1021/acsnano.0c00604.

[170] Casalini, S., Bortolotti, C. A., Leonardi, F. & Biscarini, F. Self-assembled monolayers in organic electronics. *Chem. Soc. Rev.* **46**, 40–71 (2017). URL http://dx.doi.org/10.1039/C6CS00509H.

[171] Sun, Q. *et al.* On-Surface Formation of One-Dimensional Polyphenylene through Bergman Cyclization. *J. Am. Chem. Soc.* **135**, 8448–8451 (2013). URL https://doi.org/10.1021/ja404039t.

[172] Auwärter, W. *et al.* Controlled Metalation of Self-Assembled Porphyrin Nanoarrays in Two Dimensions. *ChemPhysChem* **8**, 250–254 (2007). URL

https://chemistry-europe.onlinelibrary.wiley.com/doi/abs/10.1002/cphc.200600675.

[173] Lu, J. *et al.* Order–Disorder Transition of Two-Dimensional Molecular Networks through a Stoichiometric Design. *ACS Nano* **17**, 20194–20202 (2023). URL https://doi.org/10.1021/acsnano.3c05945.

[174] Lin, N. *et al.* Surface-assisted coordination chemistry and self-assembly. *Dalton Trans.* 2794–2800 (2006). URL http://dx.doi.org/10.1039/B515728E.

[175] Liang, Z. *et al.* Tuning Chirality of Self-Assembled PTCDA Molecules on a Au(111) Surface by Na Coordination. *ACS Nano* **17**, 10938–10946 (2023). URL https://doi.org/10.1021/acsnano.3c02819.

[176] Tseng, T.-C. *et al.* Two-dimensional metal-organic coordination networks of Mn-7,7,8,8-tetracyanoquinodimethane assembled on Cu(100): Structural, electronic, and magnetic properties. *Phys. Rev. B* **80**, 155458 (2009). URL https://link.aps.org/doi/10.1103/PhysRevB.80.155458.

[177] Dong, M., Wu, J., Miao, X., Li, J. & Deng, W. Bromine Substituent Position Triggered Halogen versus Hydrogen Bond in 2D Self-Assembly of Fluorenone Derivatives. *J. Phys. Chem. C* **123**, 26191–26200 (2019). URL https://doi.org/10.1021/acs.jpcc.9b04779.

[178] Lu, J. *et al.* Controllable Density of Atomic Bromine in a Two-Dimensional Hydrogen Bond Network. *J. Phys. Chem. C* **122**, 25681–25684 (2018). URL https://doi.org/10.1021/acs.jpcc.8b08964.

[179] Xie, L., Zhang, C., Ding, Y. & Xu, W. Structural Transformation and Stabilization of Metal–Organic Motifs Induced by Halogen Doping. *Angew. Chem. Int. Ed.* **56**, 5077–5081 (2017). URL https://onlinelibrary.wiley.com/doi/abs/10.1002/anie.201702589.

[180] Dai, J. *et al.* Dechlorinated Ullmann Coupling Reaction of Aryl Chlorides on Ag(111): A Combined STM and XPS Study. *ChemPhysChem* **20**, 2367–2375 (2019). URL https://chemistry-europe.onlinelibrary.wiley.com/doi/abs/10.1002/cphc.201900264.

[181] Yang, Z. *et al.* Metalated Graphyne-Based Networks as Two-Dimensional Materials: Crystallization, Topological Defects, Delocalized Electronic States, and Site-Specific Doping. *ACS Nano* **14**, 16887–16896 (2020). URL https://doi.org/10.1021/acsnano.0c05865.

[182] Doll, K. & Harrison, N. M. Theoretical study of chlorine adsorption on the Ag(111) surface. *Phys. Rev. B* **63**, 165410 (2001). URL https://link.aps.org/doi/10.1103/PhysRevB.63.165410.

[183] Morgenstern, K., Kibsgaard, J., Lauritsen, J. V., Lægsgaard, E. & Besenbacher, F. Cobalt growth on two related close-packed noble metal surfaces. *Surface Science* **601**, 1967–1972 (2007). URL https://www.sciencedirect.com/science/article/pii/S0039602807001446.

[184] Zhang, X. *et al.* Influence of Relativistic Effects on Assembled Structures of V-Shaped Bispyridine Molecules on M(111) Surfaces Where M = Cu, Ag, Au. *ACS Nano* **11**, 8511–8518 (2017). URL https://doi.org/10.1021/acsnano.7b04559.

[185] Baljozović, M. *et al.* Self-Assembly and Magnetic Order of Bi-Molecular 2D Spin Lattices of M(II,III) Phthalocyanines on Au(111). *Magnetochemistry* **7** (2021). URL https://www.mdpi.com/2312-7481/7/8/119.

[186] Girovsky, J. *et al.* Long-range ferrimagnetic order in a two-dimensional supramolecular Kondo lattice. *Nature Communications* **8**, 15388 (2017). URL https://doi.org/10.1038/ncomms15388.

[187] Wäckerlin, C. *et al.* Two-Dimensional Supramolecular Electron Spin Arrays. *Advanced Materials* **25**, 2404–2408 (2013). URL https://onlinelibrary.wiley.com/doi/abs/10.1002/adma.201204274.

[188] Herrera-Reinoza, N. Z. *Growth of carbon nanostructures and doped graphene via bottom-up methods*. Ph.D. thesis, University of Campinas, Gleb Wataghin Physics Institute (2022). URL https://hdl.handle.net/20.500.12733/6233.

[189] Yu, X. *et al.* On-surface synthesis of graphyne nanowires through stepwise reactions. *Chem. Commun.* **56**, 1685–1688 (2020). URL http://dx.doi.org/10.1039/C9CC07421J.

[190] Ammon, M., Sander, T. & Maier, S. On-Surface Synthesis of Porous Carbon Nanoribbons from Polymer Chains. *Journal of the American Chemical Society* **139**, 12976–12984 (2017). URL https://doi.org/10.1021/jacs.7b04783.

[191] Zuzak, R., Jančařík, A., Gourdon, A., Szymonski, M. & Godlewski, S. On-Surface Synthesis with Atomic Hydrogen. *ACS Nano* **14**, 13316–13323 (2020). URL https://doi.org/10.1021/acsnano.0c05160.

[192] Marbach, H. & Steinrück, H.-P. Studying the dynamic behaviour of porphyrins as prototype functional molecules by scanning tunnelling microscopy close to room temper-

ature. *Chem. Commun.* **50**, 9034–9048 (2014). URL http://dx.doi.org/10.1039/C4CC01744G.

[193] Ditze, S. *et al.* On the Energetics of Conformational Switching of Molecules at and Close to Room Temperature. *Journal of the American Chemical Society* **136**, 1609–1616 (2014). URL https://doi.org/10.1021/ja411884p.

[194] Buchner, F. *et al.* Diffusion, Rotation, and Surface Chemical Bond of Individual 2H-Tetraphenylporphyrin Molecules on Cu(111). *The Journal of Physical Chemistry C* **115**, 24172–24177 (2011). URL https://doi.org/10.1021/jp206675u.

[195] van Vörden, D. *et al.* Communication: Substrate induced dehydrogenation: Transformation of octa-ethyl-porphyrin into tetra-benzo-porphyrin. *The Journal of Chemical Physics* **138**, 211102 (2013). URL https://doi.org/10.1063/1.4810879.

[196] Adisoejoso, J. *et al.* A Single-Molecule-Level Mechanistic Study of Pd-Catalyzed and Cu-Catalyzed Homocoupling of Aryl Bromide on an Au(111) Surface. *Chemistry – A European Journal* **20**, 4111–4116 (2014). URL https://chemistry-europe.onlinelibrary.wiley.com/doi/abs/10.1002/chem.201304443.